# New materials and designs for 2D-based infrared photodetectors

Huitian Guo[1] and Weihong Qi[1,2] (✉)

[1] *State Key Laboratory of Solidification Processing, Center of Advanced Lubrication and Seal Materials, Northwestern Polytechnical University, Xi'an 710072, China*

[2] *Shandong Laboratory of Yantai Advanced Materials and Green Manufacturing, Yantai 264006, China*

## ABSTRACT

Infrared photodetectors have attracted much attention considering their wide civil and military applications. Two-dimensional (2D) materials offer new opportunities for the development of costless, high-level integration and high-performance infrared photodetectors. With the advent of a broad investigation of infrared photodetectors based on graphene and transition metal chalcogenides (TMDs) exhibiting unique properties in recent decades, research on the better performance of 2D-based infrared photodetectors has been extended to a larger scale, including explorations of new materials and artificial structure designs. In this review, after a brief background introduction, some major working mechanisms, including the photovoltaic effect, photoconductive effect, photogating effect, photothermoelectric effect and bolometric effect, are briefly offered. Then, the discussion mainly focuses on the recent progress of three categories of 2D materials beyond graphene and TMDs. Noble transition metal dichalcogenides, black phosphorus and arsenic black phosphorous and 2D ternary compounds are great examples of explorations of mid-wavelength or even long-wavelength 2D infrared photodetectors. Then, four types of rational structure designs, including type-II band alignments, photogating-enhanced designs, surface plasmon designs and ferroelectric-enhanced designs, are discussed to further enhance the performance via diverse mechanisms, which involve the narrower-bandgap-induced interlayer exciton transition, gate modulation by trapped carriers, surface plasmon polaritons and ferroelectric polarization in sequence. Furthermore, applications including imaging, flexible devices and on-chip integration for 2D-based infrared photodetectors are introduced. Finally, a summary of the state-of-the-art research status and personal discussion on the challenges are delivered.

## KEYWORDS

two-dimensional (2D) materials, infrared photodetectors, noble transition metal dichalcogenides, black phosphorus, layered ternary compounds, structure designs

## 1   Introduction

Infrared photodetectors have played a significant role in thermal imaging, military, communication, meteorology, and other application scenarios. Infrared radiation and its heating effect were first discovered in 1800 by a German-born British astronomer, William Herschel, with thermometers and a prism [1]. Infrared detection involves wavelengths ranging from 750 nm to 1 mm, which can be further divided into near infrared (NIR, 0.75–1.5 μm), short-wavelength infrared (SWIR, 1.5–3 μm), mid-infrared (MIR, 3–8 μm), long-wavelength infrared (LWIR, 8–15 μm) and far infrared (FIR, 15–1,000 μm) regions [2]. In early development, thermal-type infrared photodetectors (such as bolometers) played a dominant role since the puzzle of infrared radiation was not ready to be solved until Max Planck's formulation of quantum theory in 1900. Infrared photodetectors based on the photoelectric effect were developed on a large scale around the 1940s and attracted much attention after World War II [3]. In 1959, Lawson et al. successfully synthesized the mixed compound CdTe-HgTe, which rapidly became the dominant material for LWIR detection [4]. In the following decades, with the aid of lithography, crystal growth, and epitaxy technology, the

development of infrared photodetectors based on semiconductors has gone through three generations [5]. To date, commercialized infrared photodetectors based on III-V type-II InAs/GaSb superlattice or mercury cadmium telluride (HgCdTe) systems can easily realize a tunable response spectrum up to 25 μm [6–8]. For HgCdTe, by modulating the proportion of cadmium in $Hg_{1-x}Cd_xTe$, their photoelectric properties can be further optimized. In consideration of their high performance and maturity, these photodetectors hold the largest portion of the photodetector market, especially for MIR and LWIR detection [9]. Nevertheless, behind their maturity, difficulties in integration with silicon-based electronics and circuits caused by lattice mismatches [10], the high price in manufacturing processes [11] and appendant equipment to satisfy the harsh operating temperature (usually a temperature of 77 K is required) [7] hinder large-scale and small-size developments. For example, the fabrication process of conventional p-n junction HgCdTe photodetectors usually involves ion implantation and complicated side passivation processes, which can induce interface defects or contamination, leading to large dark currents [12]. The advanced growth methods of ternary crystals or III-V superlattices are metal organic chemical vapour deposition and molecular beam epitaxy, which enable the

fabrication of complex planar arrays but also put forward restrictions for the categories and crystal orientations of substrates. Meanwhile, HgCdTe photodiodes seem to fit the high operating temperature (HOT) conditions better than the type-II superlattice InAs/InAsSb photodiodes, while decades of struggles on HOT HgCdTe are still limited by the fully depleted background at the present stage [13, 14].

Thus, the special values of tunable bandgap, strong light–matter interaction, and the surface without dangling bonds benefit integration, high flexibility and transparency that two-dimensional (2D) materials can put them in the spotlight of promising infrared photodetection [15–17]. In addition to their fascinating optical and electrical properties induced by their tiny size in one dimension, what makes 2D materials so attractive in this research field is their low burden of strict lattice mismatch at the interfaces of heterostructures. This means that different 2D materials can be stacked to build heterojunctions through van der Waals (vdW) forces to realize energy band engineering and modulate the carrier behaviors.

In terms of cost-competitive 2D-based infrared photodetectors, great efforts have been made on graphene and transition metal chalcogenides (TMDs). For graphene, the single layer of honeycomb-arranged carbon atoms could exhibit a high light absorption coefficient of $7 \times 10^5$ cm$^{-1}$ over a wide optical spectrum from 300 nm to 2.5 μm [18], and the reduced carrier mobility in graphene after the effect of interfacial photonic scattering with the SiO$_2$ substrate still reached $4 \times 10^4$ cm$^2 \cdot$V$^{-1} \cdot$s$^{-1}$ at room temperature [19]. However, the total optical absorption for few-layer graphene is relatively insufficient, and the gapless band structure results in a large dark current. Thus, the deficiency of effective generation and extraction of photogenerated charges limited the photoresponsivity to a weak level. Energy band engineering and defect engineering are applied to increase the carrier lifetime and photoresponsivity of graphene. For example, Ti$_2$O$_3$ nanoparticles with a small bandgap of 0.09 eV were coupled with trilayer graphene as a mixed-dimensional photodetector [20]. Under 10 μm illumination, the responsivity reached ~ 300 A·W$^{-1}$ due to the strong optical absorption of Ti$_2$O$_3$. Considering these fundamental material properties and the prevalence situation of graphene fabrication technology, it is rather debatable to predict the encouraging future of pristine graphene in infrared photodetection to fulfil current requirements [21]. As a well-studied 2D material classification, TMDs have shown excellent performance for optoelectronic applications owing to their direct bandgap structure. As one of the most typical TMDs, molybdenum disulfide (MoS$_2$) was demonstrated with a room-temperature $I_{on}/I_{off}$ ratio of $1 \times 10^8$ and ultralow standby power dissipation as transistors [22]. Nonetheless, many bare TMDs are not suitable for MIR optoelectronic applications as a consequence of the wide bandgap with a cut-off wavelength in the visible or NIR light region only. Hence, more 2D materials and decent designs have been explored to exhibit those outstanding intrinsic properties and to develop performance-competitive 2D-based infrared photodetectors. In the past decade, on one hand, various 2D materials have been investigated in infrared detection. Black phosphorus (BP) with a polarized d detection capacity [23] and group X noble transition metal dichalcogenides (NTMDs) such as PdSe$_2$ [24] with a narrow bandgap have been investigated to compensate for detection at longer wavelengths. Ternary layered compounds such as GaGeTe exhibited promising characteristics as fast photodetectors with a 3 dB cut-off frequency of 0.9 MHz [25], and Bi$_2$O$_2$Se showed an ultrahigh response speed on the nanosecond scale [26]. On the other hand, the bond-free surface of 2D materials endows great freedom in combination with different kinds of materials via the vdW force. Some artificial

designs have been proven to successfully enhance light absorption. The effects of novel heterostructures on the interface properties, band alignment and operation principles are also discussed [27]. For example, type-II band alignment designs could enable devices to realize a sensitive and ultrafast photoresponse stemming from the strong interlayer transition and the efficient separation and recombination suppression of photoexcited carriers by the built-in field [28]. In addition, plasmonic nanostructures [29] as well as ferroelectrics [30] are added to improve optical absorption.

Although infrared photodetectors based on graphene and TMDs have been discussed and summarized partly in several reviews in recent years [21, 31, 32], other 2D materials that have brought remarkable breakthroughs for infrared photodetectors in the MIR or LWIR range and these artificial structures for further enhancement toward on-chip integration lack sufficient discussion and comparisons. Allowing for the dynamic development in this field, a review focused on other typical 2D materials and structure designs for better photodetection performance is still necessary to provide a more comprehensive perspective of this research field. In this article, we will focus on the state-of-the-art development in the past five years of some 2D materials and rational structure designs aiming at 2D-based infrared photodetection enhancement. First, some basic but vital working mechanisms that 2D-based photodetectors operate under are concisely introduced. Subsequently, recent progress on some representative 2D materials beyond graphene and TMDs are summarized, mainly including NTMDs, BP and layered ternary compounds. Next, four types of artificial structures based on different mechanisms to broaden the response spectrum or improve light–matter interactions are mainly discussed, which contain type-II band alignments, photogating heterostructures, plasmonic nanostructures and ferroelectric-enhanced structures. Furthermore, recent applications such as image sensing, flexible devices, and on-chip integration for 2D-based infrared photodetectors are introduced. Finally, this review will close with a summary including the comparison of the current research status and challenges.

## 2  Working mechanisms of 2D photodetectors

The working mechanisms of 2D photodetectors can be classified into two categories, photon detectors and thermal detectors, depending on whether the heat-induced temperature change is involved in the process by which the incident light is converted into electrical signals.

The photon type in which the photon energy of incident light excites electrons up to the conduction band (CB), leaving holes behind in the valence band (VB), mainly includes the photovoltaic effect (PVE), photoconductive effect (PCE) and photogating effect (PGE). For photodetectors operated through PVE, as Fig. 1(a) illustrates, the separation of photogenerated electron–hole pairs is driven by the built-in electric field of the p-n junction or Schottky junction in general, which suppresses the dark current. Carriers with opposite polarity are collected separately in different electrodes and contribute to the directional photocurrents. Photovoltaic devices usually exhibit a rectifying current–voltage behavior as photodiodes [33]. For example, modulated with gate voltage, the photoresponsivity of a WSe$_2$/WS$_2$ photodetector exhibited the same trend as the short-circuit current when it functioned as a photovoltaic diode [34]. To obtain a low dark current and high quantum efficiency, zero or reverse external bias is usually applied [35]. When the reverse bias is large enough for the initiation of impact ionization, the multiplied number of free carriers will be ionized, which is the working mechanism of avalanche photodetectors [36, 37]. For PCE devices, an applied bias is necessary (while for PVE devices it is not a must) to
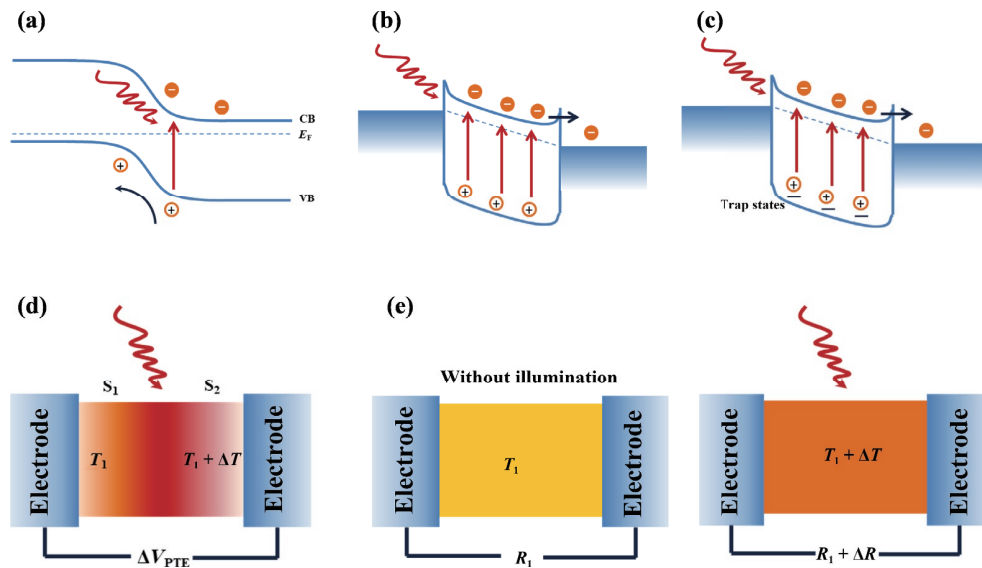
**Figure 1** Schematic of the detection mechanism: (a) PVE; (b) PCE; (c) PGE; (d) PTE; (e) BOL.

separate the photogenerated electron–hole pairs and extract the photocurrents. Without an inherent localized field, the direction of photocurrents depends on the external bias. Under illumination, as described in Fig. 1(b), the variation in free carrier density $\Delta n$ in channel materials leads to a change in conductivity $\Delta \sigma$, given as

$$\Delta \sigma = \Delta n e \mu \tag{1}$$

(where e and $\mu$ represent the unit charge and the carrier mobility of channel materials, respectively). Thus, the change in photocurrent can be offered as

$$I_{\mathrm{ph}} = A V \Delta \sigma \tag{2}$$

(where $A$ is the illuminated area and $V$ is the external bias). For photodetectors based on PGE, as shown in Fig. 1(c), the prolonged carrier lifetime and large photoconductive gain induced by the local gate greatly enhance the detection performance. Under illumination, the localized charged gates that strongly modulate the channel conductance via electrostatic interactions are performed by the charge-trapped states induced by defects and the construction of heterostructures with light sensitizer materials such as quantum dots (QDs) [10, 38]. Such separation of electrons and holes suppresses the carrier combination and then extends the carrier lifetime. Thus, considering the photoconductive gain $G$ given by

$$G = \frac{\tau_l}{\tau_t} = \tau_l V_{\mathrm{bias}} \frac{\mu}{L^2} \tag{3}$$

where $\tau_l$ and $\tau_t$ represent the carrier lifetime and the carrier transition time respectively; $L$ is the transition length; $\mu$ is the carrier mobility, and $V_{\mathrm{bias}}$ is the applied external bias between the source and the drain. PGE devices usually exhibit a high gain.

The thermal type usually contains the photothermoelectric effect (PTE) and bolometric effect (BOL), which mostly appear in graphene-based photodetectors for LWIR detection. Photodetectors based on PTE are famous for their ultrabroadband response without the limitation of the bandgap. Under illumination, the photon energy is absorbed by carriers and transferred within carriers and the crystal lattice; the electron temperature increases, and a local photovoltage is generated according to the Seebeck effect. The Seebeck coefficient $s$ is offered as

$$s = \frac{\pi^2 k_{\mathrm{B}}^2 T}{3e} \cdot \frac{\partial \ln(\sigma(\varepsilon))}{\partial \varepsilon} \Big|_{\varepsilon = E_{\mathrm{F}}} \tag{4}$$

where $k_{\mathrm{B}}$ is the Boltzmann constant; $T$ represents the temperature; e is the unit charge; $\varepsilon$ represents the energy level, and the derivative function takes the value when $\varepsilon$ is at the Fermi level. As the incident light illuminates areas with different Seebeck coefficients, the temperature difference results in a potential difference, which can be converted into photoresponsivity $R$ according to

$$R = \frac{V_{\mathrm{ph}}}{P} \tag{5}$$

where $V_{\mathrm{ph}}$ represents the photogenerated voltage and $P$ represents the incident power. Therefore, the photocurrent will increase with the increase in the photothermal-generated voltage that drives it. Thus, according to the formula

$$\Delta V_{\mathrm{PTE}} = (S_1 - S_2) \Delta T \tag{6}$$

(where $S_1$ and $S_2$ are the Seebeck coefficients of two areas with different thermoelectric responses), photodetectors with higher sensitivity require a larger asymmetry of the Seebeck coefficients or a larger temperature gradient distribution, resulting in a greater voltage, as illustrated in Fig. 1(d). Such asymmetry can be realized by localized plasmonic structures [39], localized illumination [40] and asymmetric metal contacts [41]. For example, the thermal conductivity of multilayer graphene is larger than that of gold. Playing the role of electrodes, the PdSe$_2$ nanoflakes could form asymmetric vdW contacts with them [42]. With the architecture of an asymmetric heat sink, the photodetector exhibited a global photovoltage response that was not limited in the contact region, showing the characteristic of PTE. Under global infrared illumination, the self-powered PTE photodetector realized a responsivity of over 13 V·W$^{-1}$ and response time of ~ 50 μs in the 4.6–10.5 μm range at room temperature due to hot carrier diffusion driven by the temperature gradient. Different from the self-driven characteristic of PTE, devices based on BOL require an external bias. The BOL is based on the resistance change of the temperature-sensitive channel resulting from the heating effect under illumination (Fig. 1(e)), which is quite similar to PCE. BOL photodetectors possess fast response characteristics due to the wavelength independence of the thermal effect, which can be understood as the independence of the carrier trapping and releasing process. For example, a remarkable photoresponse to incident light of 10.6 μm with photon energy below the bandgap (0.98 eV, with a corresponding absorption edge of ~ 1,265 nm) demonstrated the existence of BOL in the SnSe-based

photodetector, where thermally induced holes (also known as hot holes) were generated in the VB rather than photogenerated electron–hole pairs among the CB and the VB [43]. Thus, a much faster response was observed after the switch on/off of the laser, without moderate rising or falling processes.

In addition to the 5 basic mechanisms mentioned above, there are other summarized mechanisms. Carrier tunneling can suppress the thermal noise and dark current in a photodetector, leading to a high on/off ratio. This can be ascribed to the introduction of insulator layers, which are usually the hBN layers, forming a sharp barrier in band alignment for tunneling. The tunneling effects include Fowler–Nordheim quantum tunneling [44] and direct tunneling [45]. In a photodetector based on a $MoTe_2/hBN/MoTe_2/hBN$ heterostructure, a dark current at a magnitude of $10^{-10}$ A and a fast response speed of 37.5/50 μs were reported at room temperature [44]. The tunneling behavior is mainly dominated by holes under a reverse drain bias. Moreover, in a specific photodetector, photoresponses under different wavelengths of incident light can be ascribed to different working mechanisms via precise designs [46], and the mixture of mechanisms under a certain wavelength is also common due to the inevitable energy conversion between photons and lattice vibrations, which induces thermal effects in the generation of currents. In general terms, compared with the photon type, the thermal type has an unwilling slower response speed, despite the advantages in broadband detection. When the incident photon energy is high enough to excite carriers from the VB to the CB in 2D materials, the dominant principle usually belongs to the photon-type. However, the photoresponse under weak illumination is sometimes induced by thermal types. Jiang et al. developed a $p-VO_2/n-MoTe_2$ hybrid photodetector that successfully realized three modes under different conditions [47]. Ultrasensitive detection with a response speed of 17 μs in the range from 450 nm to 1.31 μm was realized by the p-n junction mode. When the external bias turned forward and the wavelength exceeded 1.31 μm, the bolometer mode preponderated over the PVE, exhibiting an ultrabroad response region beyond 10 μm. The third mode of the Schottky junction occurred at a higher temperature, and semiconducting $VO_2$ was transferred into the metallic material.

Some figures of merit are generally used to evaluate and compare the performance of photodetectors with different working mechanisms, which include the photoresponsivity, external quantum efficiency (EQE), noise equivalent power (NEP), response speed, and linear dynamic range (LDR). Photoresponsivity $R$ characterizes the optical-to-electrical conversion ability of photodetectors, and is defined as the photocurrent or output voltage generated by each watt per unit area. $R$ changes at different wavelengths and frequencies. EQE is also a convenient parameter to measure the optical-to-electrical conversion ability from the perspective of quantum, which is offered by

$$EQE = \frac{hc}{e\lambda}R \qquad (7)$$

where $h$ is the Planck constant; $c$ is the speed of light; $\lambda$ represents the incident wavelength. NEP is defined as the signal power that gives a signal-to-noise ratio of one in a one hertz output bandwidth

$$NEP = \frac{I_{noise}}{R} \qquad (8)$$

where $I_{noise}$ is the noise current, which represents the detective ability of a weak signal. A smaller NEP value means that the photodetector can detect a weaker signal. The specific detectivity

$D^\star$ (the reciprocal of NEP) is commonly used to characterize the sensitivity of photodetectors, and a larger $D^*$ represents better sensitivity. In addition, when calculating the value of $D^*$, the convenient formula relating to the dark current $I_d$, effective area $A$, and photoresponsivity $R$ is usually chosen

$$D^* = \sqrt{\frac{A}{2eI_d}}R \qquad (9)$$

Apparently, response speed characterizes the photodetectors' sensitivity to incident signals on a time scale, and it usually refers to the time that the photocurrent changes from 10%/90% to 90%/10% of the maximum under step signals. A faster response speed represents a faster speed to convert the incident optical signal to an electrical signal. LDR represents the normal operating range of a detector, with units of dB. In this range, the value of electric signals (currents or voltages) is proportional to the power density of incident light. Moreover, the on-off ratio and $G$ can also evaluate a photodetector.

It is worth mentioning that the performances of infrared photodetectors under blackbody radiation are more referable and relevant. Blackbody radiation is more similar to the signals emitted by real objects compared to the laser.

# 3 Materials for infrared photodetection beyond graphene and TMDs

The issues mentioned before that graphene and TMDs face require the exploration of other 2D materials with high performance or considerable photoresponse in MIR and LWIR for communication or military applications. In addition, allowing for the convenience of constructing vdW heterostructures, the investigation of more 2D materials can provide more possibilities.

## 3.1 Noble transition metal dichalcogenides

Group X noble transition metal dichalcogenides (NTMDs, with formula $MX_2$, M = Pt, Pd; X = S, Se, Te) have stimulated considerable research interest in recent years owing to tunable narrow bandgaps, high carrier mobility at room temperature and outstanding air stability for broadband infrared photodetection [48, 49]. Compared to other TMDs, a stronger hybridization between group X metal d orbitals and chalcogen p orbitals is formed in NTMDs, indicating unique properties such as extensive interlayer coupling and a layer-dependent bandgap. For example, $PtS_2$ is calculated by density functional theory (DFT) to exhibit the properties of indirect bandgap semiconductors for monolayer and bulk materials with bandgaps of 1.8 and 0.48 eV, respectively [50, 51], and the tunable bandgap of $PtS_2$ is experimentally proven [51]. Additionally, a temperature-dependent effect on the carrier mobility of the few-layer transistors from metal to insulator was examined [50]. At room temperature, 2D $PtS_2$ photodetectors with a spectral response range from visible to MIR exhibited a fast photoresponse of 175 μs at 830 nm. In addition, experiments and theoretical calculations on some NTMDs even proved a transition from semimetal to semiconductor when decreasing the layer number of materials from bulk to monolayer. Usually, the bandgaps of few-layer devices correspond with light absorption in the infrared region. Such a situation exists in $PtSe_2$ [52] and $PdSe_2$ [53, 54], and photodetectors based on them as well as their vdW heterojunctions exhibit remarkable properties. The properties of related applications are summarized in Table 1.

The monolayer and bilayer $PtSe_2$ are semiconductors with indirect bandgaps of ~ 1.2 and ~ 0.3 eV, respectively, while the thick layer becomes metallic. The photoresponsivity of the bilayer $PtSe_2$ photodetector was 5.5 and ~ 4.5 A·$W^{-1}$ at NIR and 10 μm, respectively, which is approximately three orders of magnitude

**Table 1** Performance of NTMD-based infrared photodetectors. $R$, $D^*$, $\tau_r$, and $\tau_d$ represent the photoresponsivity, specific detectivity, rising time and decading time, respectively

| Material | Detection range (μm) | $R$ (A·W$^{-1}$) | $D^*$ (Jones) | $\tau_r/\tau_d$ (μs) | EQE (%) | Ref. |
|---|---|---|---|---|---|---|
| PdSe$_2$/MoS$_2$ | 0.45–10.6 | 42.1 (10.6 μm) | $6.09 \times 10^{10}$ (4.012 μm) | $74.5 \times 10^3/93.1 \times 10^3$ | 25.4 | [61] |
| p-BP/n-PdSe$_2$ | 0.532–1.31 | $1.63 \times 10^5$ (1,310 nm) | $1.13 \times 10^{13}$ (532 nm) | $1.6 \times 10^3/4.7 \times 10^3$ | $9.4 \times 10^6$ | [62] |
| PdSe$_2$/CdTe | 0.2–10.6 | $3.247 \times 10^{-2}$ | $3.3 \times 10^{12}$ | 4.9/8.3 | — | [63] |
| PtSe$_2$/CdTe | 0.2–2 | $5.065 \times 10^{-1}$ (780 nm) | $4.2 \times 10^{11}$ (780 nm) | 8.1/43.6 | — | [64] |
| PtS$_2$/PtSe$_2$ | 0.405–2.20 | $\sim 6 \times 10^{-2}$ (1,064 nm) | — | $6.6 \times 10^4/75 \times 10^4$ | 1.2 (1,064 nm) | [65] |
| PdSe$_2$/MoTe$_2$ | 0.405–2 | $1.24 \times 10^5$ (400 nm) | $2.42 \times 10^{14}$ (400 nm) | 16.1/31.1 | 130 (2,000 nm) | [66] |
| InSe/PdSe$_2$ | 0.532–1.65 | 58.8 (1,650 nm) | $1 \times 10^{10}$ (1650 nm) | $1.6 \times 10^5/1.8 \times 10^5$ | 4,660 (1,650 nm) | [67] |
| PdSe$_2$/SiNWA | 0.2–4.6 | 0.726 (980 nm) | $3.19 \times 10^{14}$ (980 nm) | 25.1/34 | — | [68] |

higher than that of common graphene photodetectors [52]. Azar et al. [55] presented a multilayer PtSe$_2$ photodetector based on an optical cavity substrate containing a TiO$_2$ spacer and a gold mirror layer, which enhanced the light-matter interaction and extended the photoresponse to LWIR, realizing a responsivity up to 54 mA·W$^{-1}$ at 8.35 μm. By directly integrating 2D PtSe$_2$ onto the Si waveguide via area-selective low-temperature growth, a complex hybrid structure is obtained [56] (Fig. 2(a)). However, the responsivity of this photodetector at 1,550 nm is only 1.93 nA·W$^{-1}$. PdSe$_2$ is another popular star in NTMDs, showing a broadband response range [57] (from visible to THz) and outstanding air stability [58]. 2D PdSe$_2$ is usually obtained by mechanical exfoliation or chemical vapour deposition (CVD), while Zeng et al. [54] demonstrated an easy selenization approach to fabricate PdSe$_2$ films. The films are uniform, and the thickness corresponds to that of the Pd layer, offering a controllable method for practical application. Based on this as-selenized method, researchers conducted more interesting research. Luo et al. constructed an as-assembled PdSe$_2$/Ge nanocone (GeNC) heterojunction infrared photodetector by transferring the selenized palladium layer onto a solution-etched Ge wafer [59]. The PdSe$_2$/GeNC hybrid infrared photodetector exhibits high sensitivity to infrared illumination. A responsivity of 530.2 mA·W$^{-1}$ and an EQE of 42.4% were obtained, which resulted from the built-in field and the strong light trapping effect induced by the nanocone structures. Similarly, Liang et al. [60] chose the alkali etching method to obtain a pyramid microstructure morphology of silicon (illustrated in Fig. 2(b)). Then, a Pd layer was deposited and selenized on the surface of pyramidal Si. The as-fabricated photodetector exhibited excellent photoresponse performance in terms of a responsivity of 456 mA·W$^{-1}$ and a high specific detectivity of up to $9.97 \times 10^{13}$ Jones under 980 nm illumination at zero bias due to the light trapping effect of the pyramid structure and built-in field, as mentioned above. Both devices above can function as infrared light sensors.

Moreover, the puckered pentagonal structure of PdSe$_2$ makes the polarization-sensitive response to light possible [24, 69, 70]. The accurate detection of polarimetric information in incident optical signals from the environment is essential and desired. Usually, a polarizer is used to obtain tunable polarized incident light. The pronounced polarization sensitivity could be attributed to the in-plane anisotropic structure of 2D PdSe$_2$ and the built-in perpendicular electric field [68, 71, 72], and an ultrahigh polarization sensitivity of up to 112.2 was achieved by Wu et al [72].

### 3.2 Black phosphorus

Another puckered 2D material is BP, showing strengths in MIR photodetection due to the narrow direct bandgap decreasing from $\sim 2.0$ eV (monolayer) to $\sim 0.3$ eV (bulk form, corresponding to a

4.13 μm cut-off wavelength) [73] and high internal photoconductive gain [74] via various fabrication approaches [75]. Three Raman peaks corresponding to three vibration modes of BP exhibit different polarization responses as a function of sample layer number [76]. The Raman spectra of a 7.75 nm BP flake encapsulated by a polymethyl methacrylate layer under different polarization angles are illustrated in [77]. With the polarization of the incident light varying from 0 ($x$) to 90° ($y$), the intensity of the A$_{2g}$ mode decreased markedly because the main atomic vibration of the A$_{2g}$ mode was in the $x$ direction, verifying the anisotropy of the crystal orientation. Thus, BP is suitable for high-performance polarized IR detection [78, 79] and imagination [80], as well as the applications of on-chip MIR systems [81, 82] when integrated with silicon waveguides. Homojunctions aided by element doping [83, 84] and heterojunctions [85, 86] were used to improve the photodetection performance of BP, and the latter is a more common approach. Zhang et al. employed a Mo bottom electrode as a light-absorption-enhanced mirror to construct a graphene/BP heterostructure photodetector (Fig. 2(d)) exhibiting high photoresponsivity and EQE under PVE [87]. This device has an ultrabroad photoresponse spectrum from 637 nm to 4.25 μm. As Fig. 2(e) illustrates, from 0.637 to 3.662 μm, the photoresponsivity and EQE decreased as the wavelength increased, whereas in the remaining part, an increasing tendency was found, which was ascribed to the corresponding high light absorption of the BP film in this range. The low Schottky barrier between Mo and BP, the built-in field within the depletion layer and the high carrier mobility of graphene contributed to the efficient carrier separation and collection, and a high specific detectivity of $6.69 \times 10^8$ Jones at 4.25 μm was achieved.

Introducing arsenic into BP to form b-AsP can significantly extend the operational wavelength range of BP-based photodetectors [88]. Specifically, the bandgap of b-As$_x$P$_{1-x}$ could be tuned from 0.3 to 0.15 eV (with the corresponding wavelength of 8.5 μm) via the variation of $x$ [89]. A detailed comparison of the basic characteristics, such as electronic properties, between BP and b-AsP was discussed in a review [23]. Regarding the environmental stability, BP films degraded and bubbled after 3 days, while b-AsP showed negligible degradation after 7 days according to atomic force microscope measurements [90]. The field-effect modulation of b-AsP in the mid-infrared region is practical [91]. A remarkable gate-controlled ambipolar behavior is observed in the transfer characteristics of b-As$_{0.084}$P$_{0.916}$-based field-effect transistors (FETs), with drain current modulation on the order of 10$^5$ and the highest charge carrier mobility of up to 147 cm$^2$·V$^{-1}$·s$^{-1}$ [92]. These FETs were also sensitive to a broad wavelength region from visible to NIR (450–2,200 nm), achieving a photoresponsivity of 0.45 A·W$^{-1}$ and specific detectivity up to $6.45 \times 10^9$ Jones under 1,550 nm illumination.

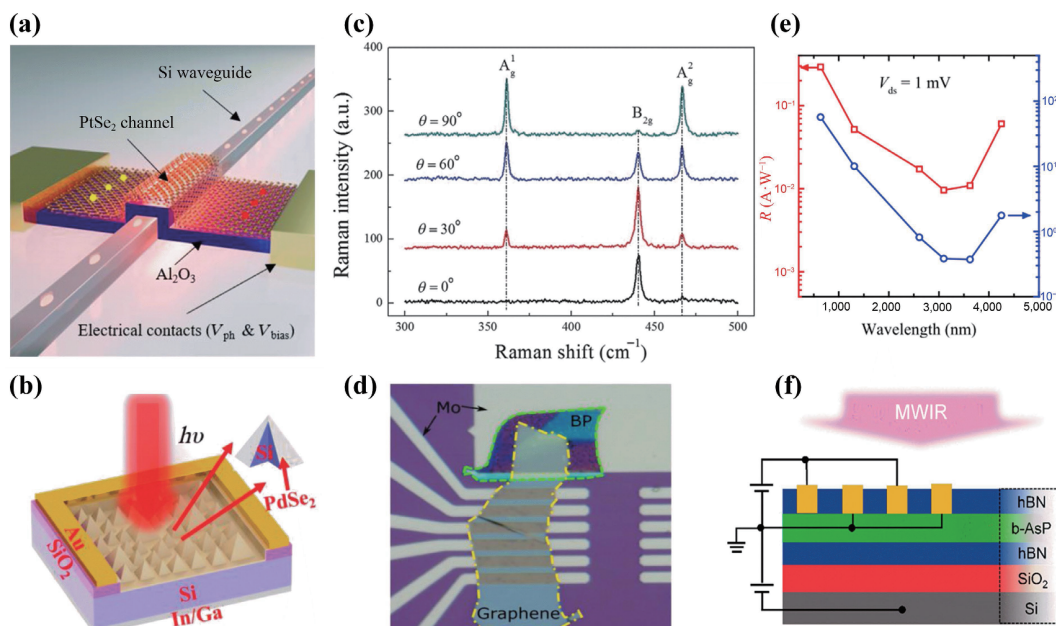However, compared with NTMDs, BP (or b-AsP) has little

**Figure 2** (a) Schematic of the integrated $PtSe_2$ infrared photodetector on a silicon waveguide. Reproduced with permission from Ref. [56], © Prechtl, M. et al. 2021. (b) Schematic illustration of the $PdSe_2$/pyramid Si array heterojunction photodetector. Reproduced with permission from Ref. [60], © WILEY-VCH Verlag GmbH & Co. KGaA, Weinheim 2019. (c) Polarized Raman spectra of the encapsulated BP with different polarization angles. Reproduced with permission from Ref. [77], © WILEY-VCH Verlag GmbH & Co. KGaA, Weinheim 2016. (d) Optical image of the Mo-BP-graphene vertical heterojunction photodetector. (e) $R$ and EQE as a function of wavelength from 0.637 to 3.662 μm. Reproduced with permission from Ref. [87], © Zhang, X. M. et al. 2021. (f) Cross-sectional schematic of the as-fabricated hBN/b-$As_{0.83}P_{0.17}$/hBN heterostructure photodetector. Reproduced with permission from Ref. [95], © American Chemical Society 2018.

advantage over air stability. Protective layers to prevent oxidation, such as boron nitride (BN), are designed at the top of the device, contributing to its eminent photoresponse, fast response time up to ~ 16 μs, a high $I_{on}/I_{off}$ of ~ $10^3$ and a reasonable photoresponsivity of ~ 1.55 A·W⁻¹ [93]. Chen et al. demonstrated an hBN/BP/hBN sandwich structured photodetector, in which the hBN dielectric guaranteed an ultraclean interface for efficient photocarrier collection [94]. The vertical electric field resulting from the Stark effect in this 5 nm-thick BP device dynamically extended the photoresponse spectrum from 3.7 to beyond 7.7 μm. The photodetector exhibited peak responsivities at 77 K of 518, 30, and 2.2 mA·W⁻¹ at 3.4, 5, and 7.7 μm, respectively. Similarly, encapsulated by hBN, the b-AsP in a hBN/b-$As_{0.83}P_{0.17}$/hBN heterostructure photodetector (Fig. 2(f)) was preserved well free from oxidation after several months via elemental analysis by electron energy loss spectroscopy [95]. Based on the intrinsic photoconduction mode, at room temperature, the device exhibited photoresponsivities of 190, 16 and 1.2 mA·W⁻¹ at 3.4, 5.0 and 7.7 μm, respectively.

### 3.3 Ternary compounds

Recently, a newly developed 2D material $Bi_2O_2Se$ belonging to layered bismuth oxychalcogenides ($Bi_2O_2X$: X = S, Se, Te) has attracted much attention in the high-performance infrared photodetection field due to its ultrahigh carrier mobility (~ 29,000 cm²·V⁻¹·s⁻¹ at 1.9 K and ~ 450 cm²·V⁻¹·s⁻¹ maintained at room temperature) and an indirect narrow bandgap of 0.8 eV (bulk form) corresponding to the infrared spectrum [96]. Compared to vdW layered materials connected by vdW interactions, the layers of $Bi_2O_2X$ are connected by electrostatic forces. These alternately stacked $[Bi_2O_2]_n^{2n+}$ cation and $[X]_n^{2n-}$ anion layers are described as a zipper model [97], in which fifty percent of the $[X]_n^{2n-}$ layer belongs to the upper $[Bi_2O_2]_n^{2n+}$ layer while the other fifty percent belongs to the lower layer (Fig. 3(a)). Thus, $Bi_2O_2X$ can exhibit some layer-dependent properties. For example, 2D $Bi_2O_2Se$ exhibits ultrahigh mobility, outstanding stability, tunable bandgaps, and excellent performance in electronics and optoelectronics [98].

A CVD-synthesized $Bi_2O_2Se$ photodetector demonstrated by Yin et al. exhibited a high sensitivity of 65 A·W⁻¹ at 1,200 nm [99]. The great performance of this device in detecting weak incident light from visible to infrared was ascribed to photoconductive gain under applied bias. Moreover, an ultrafast photoresponse attributed to the outstanding electron mobility was measured by time-resolved photocurrent spectroscopy. The response speed was ~ 1 ps at room temperature, which is comparable to the reference graphene sample of ~ 1.3 ps. In addition, the high stability of the photoresponse in ambient air for more than five weeks was proven, which could be attributed to the lack of surface dangling bonds in the selenium terminal atomic layer [96]. Li et al. synthesized $Bi_2O_2Se$ nanosheets via low-pressure CVD [100]. The NIR performances of $Bi_2O_2Se$-based photodetector were studied and interestingly, the responsivity and response speed remained in the same level under the temperature varying from 80 to 300 K. This might resulted from the inexistence of shallow defects energy levels or surface trap states.

While $Bi_2O_2Se$ has great potential, the intrinsic toxic selenium contained in this remarkable material could be a fly in ointment. Thus, $Bi_2O_2S$ with a similar crystal structure could become the next alternative. Since the atomic number of sulfide is smaller than that of selenium, the indirect bandgap of $Bi_2O_2S$ is wider than that of $Bi_2O_2S$, which can be ascribed to the decrease in the p-orbital ionization energy of the X anion in $Bi_2O_2X$ [101]. An NIR photodetector based on $Bi_2O_2S$ nanosheets synthesized with a cost-saving method at room temperature was demonstrated [102]. Chitara et al. chose a one-pot wet-chemical method and $Bi(NO_3)_3·5H_2O$ and $CH_4N_2S$ as raw materials to synthesize the nanosheets and drop-cast to fabricate the device, as shown in Fig. 3(b). Since the solution containing $Bi_2O_2S$ was dried in vacuum overnight, the agglomerated nanosheets were observed under transmission electron microscopy (TEM), which may lead to the relatively slow response time of 100 ms. PCE was considered to be the photoresponse mechanism in this NIR photodetector, so the electron–hole pairs were extracted under applied bias upon
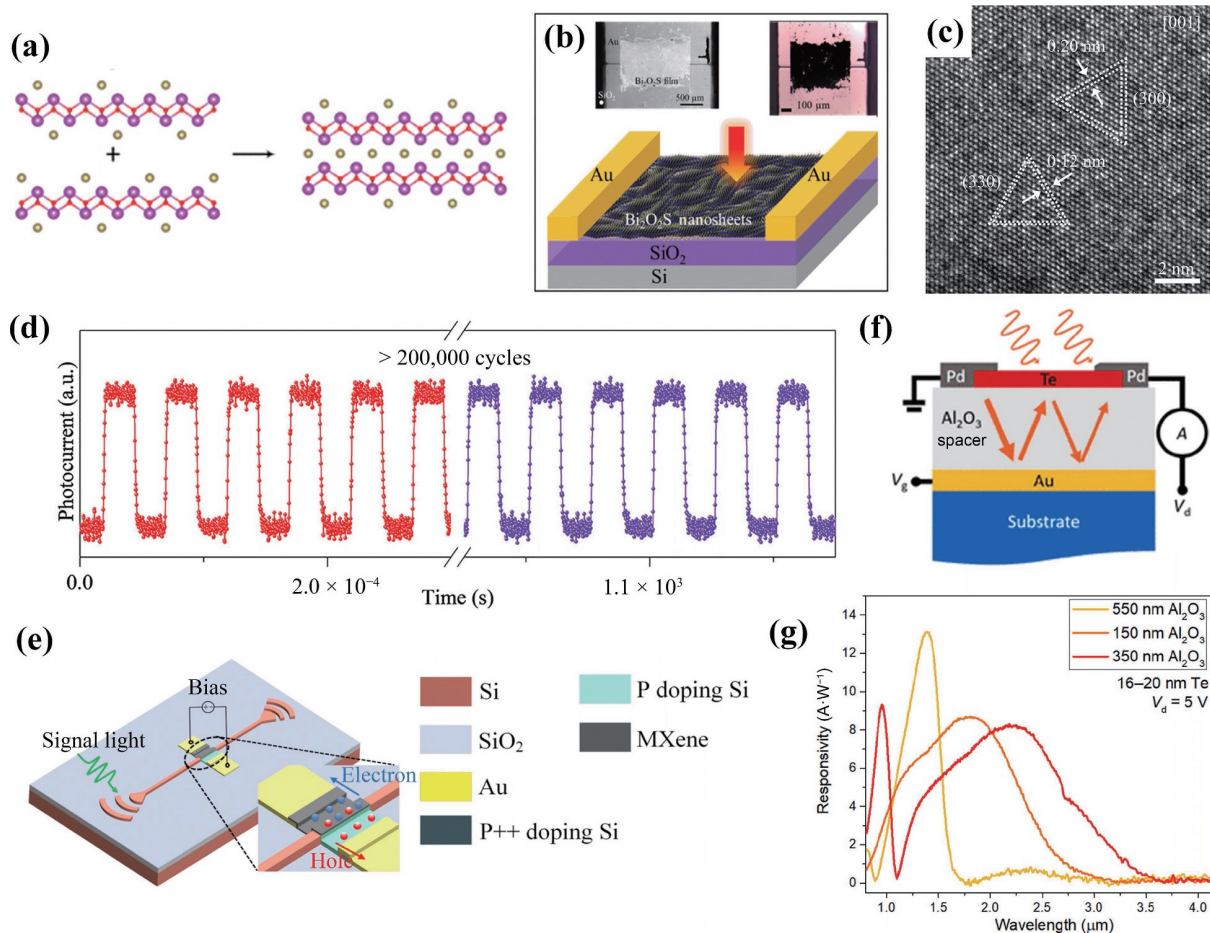
**Figure 3** (a) Scheme of the zipper model of bilayer Bi₂O₂Se. Reproduced with permission from Ref. [97], © American Chemical Society 2019. (b) Schematic of the solution-processed Bi₂O₂S photodetector. Reproduced with permission from Ref. [102], © the Royal Society of Chemistry 2020. (c) High-resolution TEM (HRTEM) image of InSiTe₃ and (d) stability tests of the InSiTe₃ photodetector, under 200,000 cycles of switch operations. Reproduced with permission from Ref. [111], © American Chemical Society 2022. (e) The structure of the Ti₃C₂Tₓ/p-Si photodetector. Reproduced with permission from Ref. [123], © Yang, C. M. et al. 2021. (f) Schematic of the SWIR photoconductor based on quasi-2D Te nanoflakes and (g) photoresponsivity of quasi-2D Te nanoflakes infrared photodetectors with different Al₂O₃ thicknesses. Reproduced with permission from Ref. [127], © American Chemical Society 2018.

illumination. A photoresponsivity of 4 A·W⁻¹ and a high EQE of 630% at 785 nm wavelength were demonstrated. A similar synthesis method was applied to fabricate a Bi₂O₂S photoelectrochemical photodetector with a broad detection range from 365 to 850 nm [103]. A lower synthesis temperature for 2D infrared photodetectors also has advantages in integration with silicon-based circuits. A low-temperature approach was reported for a 2D Bi₂O₂Te-based photodetector [104]. The transition from a sputtered Bi₂Te₃ ultrathin film grown on an n-Si substrate to 2D Bi₂O₂Te occurred after rapid annealing in the atmosphere at 400 °C, which was bearable for the complementary metal oxide semiconductor (CMOS) process, permitting direct large-scale integration. With an ultrabroadband infrared photodetection from 210 to 2.4 mm, the photodetector exhibited a remarkable responsivity of up to $3 \times 10^5$ and $2 \times 10^4$ A·W⁻¹ and a specific detectivity of $4 \times 10^{15}$ and $2 \times 10^{14}$ Jones for deep ultraviolet (UV) and SWIR under weak light illumination, respectively.

Bi₂O₂X has exhibited much potential in infrared photodetection, especially its broadband detection ability. However, compared with vdW materials, their stronger binding energy makes it quite harder for large-area exfoliation from the bulk to a single layer [97], and except for Bi₂O₂Se, the precise control in bottom-up methods such as CVD or hydrothermal synthesis to fabricate 2D bismuth oxychalcogenides with satisfactory performance is still quite challenging [98, 99, 105]. The difficulty of ternary compound crystal growth with few lattice defects or segregation might be the constraint for these 2D ternary

compound photodetectors to obtain better performance, so approaches to high-quality flakes are desired. Such a situation was also embodied in related studies about other ternary compounds. Chemical vapour transit (CVT) was applied in high-quality crystal growth before mechanical exfoliation for 2D photodetectors based on materials such as HfSSe [106], SnS₁.₂₆Se₀.₇₆ [107] and FePSe₃ [108], which contributed to decent photodetection in the infrared region. Regarding bottom-up methods, Kang et al. developed a reliable confined-space CVD to fabricate few-defect and large-area ReS₂₍₁₋ₓ₎Se₂ₓ monolayer crystals on SiO₂/Si substrates with the assistance of NaCl, which promoted the formation of an intermediate product, provided a stable environment and contributed to a response speed of approximately 35 ms at 940 nm [109]. Luo et al. fabricated a 2D Bi₂Te₂Se (BTS) photodetector via an atmospheric-pressure solid source thermal evaporation method, which exhibited a fast response speed up to 2 μs in the spectrum of 365–980 nm and a photoresponsivity of 2.74 A·W⁻¹ at 980 nm under modulation [110]. High-quality triangle BTS nanosheets with a thickness of 4 nm and a largest lateral size up to 60 nm were obtained by optimizing the evaporation conditions. For the photodetector, a few defects in BTS flakes trapped a small part of holes to enhance the concentration of electrons in the channel, implying the existence of PGE. Chen et al. synthesized an InSiTe₃ crystal by a high-temperature solid-state reaction, and the photodetector based on this layered material with trigonal symmetry (Fig. 3(c)) showed an ultrafast photoresponse 545–576 ns from UV (265 nm) to NIR (1,310 nm) dominated by PCE

[111]. In addition, the photoresponse owned outstanding stability during 200 000 cycles, as illustrated in Fig. 3(d). In addition, vdW heterostructures such as MQDs/Ta$_2$NiSe$_5$ [112], CrPS$_4$/MoS$_2$ [113], Bi$_2$O$_2$Se/MoSe$_2$ [114] and BTS/Bi$_2$O$_2$Se [115] also optimized the optoelectrical properties of photodetectors based on 2D ternary compounds under infrared illumination.

### 3.4 Other materials

In addition to what has been discussed above, there are some other 2D materials, such as semiconducting metal-organic frameworks (MOFs) [116], that exhibit potential applications for infrared detection. Overall, the reported theoretical studies [117, 118] imply that more new materials remain to be explored.

As a large family of 2D materials, a few MXenes are favored by photodetectors as new candidates due to their high conductivity and possibility in large-scale synthesis [119, 120]. In addition to the layer-dependent effect, MXenes also show tunable optical properties by the regulation of surface functional groups. On this basis, they can play a role as transparent electrodes due to their tunable work function, which matched well with that of photoabsorbers, and the good contact promoted charge transfer and light absorption [121, 122]. In addition, MXenes also functioned as photoabsorbers, and one practical future for MXenes could be combining with well-studied conventional materials, such as Si and III–V materials. Yang et al. designed a vdW Schottky junction photodetector based on Ti$_3$C$_2$T$_x$/p-Si, whose structure is schematically illustrated in Fig. 3(e) [123]. The photodetector demonstrated a widely tunable working wavelength in SWIR regions with the aid of vacuum annealing. After the simple surface treatment, the -F, and =O functional groups with high dipole moments by vacuum annealing were removed; the work function of Ti$_3$C$_2$T$_x$ was decreased from 4.66 to 4.43 eV, and the Schottky barrier height (SBH) was correspondingly increased from 0.64 to 0.72 eV, resulting in a 215 nm blueshift of the working wavelength. Under 1,550 nm illumination and an external bias of 2 V, the device exhibited a photoresponsivity of 0.55 μA·W$^{-1}$, which left a quite large space for improvement. Except for the higher Schottky barrier, the morphology defects induced by spray coating were also unfriendly to hot carriers to transition into silicon due to clastic films with different sizes contained in Ti$_3$C$_2$T$_x$ films. Other synthesis methods, such as CVD, may be promising approaches to more planar nanoflakes. Through another simple synthesis method, drop casting, Zhang et al. fabricated a self-driven photodetector based on a Ti$_3$C$_2$T$_x$/GaAs Schottky heterostructure [124], which was able to detect light with wavelengths up to 980 nm. The device exhibited a high sensitivity up to 980 nm light illumination, exceeding the absorption edge of GaAs (874 nm), which could be explained as hot electrons in Ti$_3$C$_2$T$_x$ overcoming the Schottky barrier. In this report, Ti$_3$C$_2$T$_x$ films on GaAs were also composed of disordered nanoflakes. However, these nanometric nanoflakes with a high density of edges and gaps were assumed to efficiently relax plasmonic momentum constraints and promote energized hot electron generation, which had a positive influence on the performance.

2D Te, with a unique helical chain structure, outstanding environmental stability, high carrier mobility and low-cost synthesis approaches, has exhibited great potential in high-performance polarized infrared photodetectors [125]. The chain structure induced an ultrahigh extinction ratio of ~ 2,812 at 3.4 eV photon energy, and the transition of Te 5p bonding orbitals along or perpendicular to the chain directions realized ultrastrong anisotropic photoresponsivity [126]. Amani et al. proposed SWIR photodetectors based on hydrothermally synthesized Te nanoflakes [127] (Fig. 3(f)). The Au/Al$_2$O$_3$ optical cavity substrate was employed to cover the shortage in light absorption (1.6–

3.4 μm) induced by the 0.3 eV indirect bandgap of 12 nm-thick Te. As Fig. 3(g) shows, the peak photoresponsivity wavelength of the photodetector can be tuned by the thickness of Al$_2$O$_3$ from 1.4 μm (13 A·W$^{-1}$) to 2.4 μm (8 A·W$^{-1}$) with a cut-off wavelength up to 3.4 μm, which fully covers the SWIR band. An excellent specific detectivity of $2 \times 10^9$ Jones was obtained at 1.7 μm at room temperature. In addition, due to the anisotropic crystal structure of Te nanoflakes, the devices also exhibited a polarization-sensitive SWIR photoresponse. The blackbody-sensitive infrared detection of Te devices was also demonstrated, supported by a high responsivity of 6650 A·W$^{-1}$ (at 1,550 nm) and a blackbody responsivity of 5.19 A·W$^{-1}$ [128]. Moreover, compared with BP, the excellent stability without degradation under ambient atmospheric conditions provided strong support for applications of 2D Te-based photodetectors. In addition, photodetectors based on 2D α-GeSe also possessed the property of environmental stability [129] for NIR polarization imaging with a contrast ratio up to 2.45 at 808 nm [130].

## 4 Device structure construction for infrared photodetection

Although the electronic and optical properties of 2D materials can be controlled by doping, strain, and other means, it is difficult to achieve large-scale applications with these methods. Therefore, performance enhancement and modulation actualized by structure designs becomes a pathway with more potential.

### 4.1 Type-II band alignments

According to the different structures of band alignments, the band structures of heterostructures can be classified into three categories: straddling gap (type-I), staggered gap (type-II) and broken gap (type-III). For type-I band alignments, electrons and holes transfer into the narrow-bandgap side due to its lower conduction-band minimum (CBM) and higher valence-band maximum (VBM) than those of the other material with a broader bandgap. Such a carrier transfer process will lead to a strong charge combination, which is suitable for electroluminescent devices instead of photodetectors. Type-II heterostructures are promising candidates for optoelectronic devices [131], such as photodetectors and solar cells, due to broadband light absorption induced by the formation of a subbandgap. Two perovskite QDs, CH$_3$NH$_3$PbBr$_3$ QDs (MQDs) and CsPbI$_{3-x}$Br$_x$ QDs (CQDs), were precisely synthesized to construct typical type-I and type-II 0D/2D vdW heterostructures with MoS$_2$ and to further carry out an in-depth understanding of interfacial photogenerated charge behavior [132]. The energy band structure models are illustrated in Fig. 4(a). Comparing the photoluminescence (PL) spectra of two band alignments (Figs. 4(b) and 4(c)), a pronounced quenched PL of MQDs in type-I vdW heterostructure could be ascribed to the nonradiative energy and carriers transferring from MQDs to MoS$_2$. The quenching for both CQDs and MoS$_2$ in type-II verified efficient charge diffusion to and through heterostructure interfaces, facilitating carrier separation. Furthermore, characteristics including PL lifetime, photocurrent, responsivity and detectivity demonstrated a better photoresponse performance. For the broken bandgap, the band-to-band quantum tunneling of charge transport induced by the nonoverlapping bandgap between two semiconductors making up the type-III band alignment endows some devices (mostly tunneling field-effect transistors, TFETs for short) based on this band structure with a high speed and low power [133]. Adjustments of the intensity and direction of the external bias voltage could change the size of the bandgap and even make the band alignment of the heterojunction switch between the three types mentioned above [134, 135], implying that
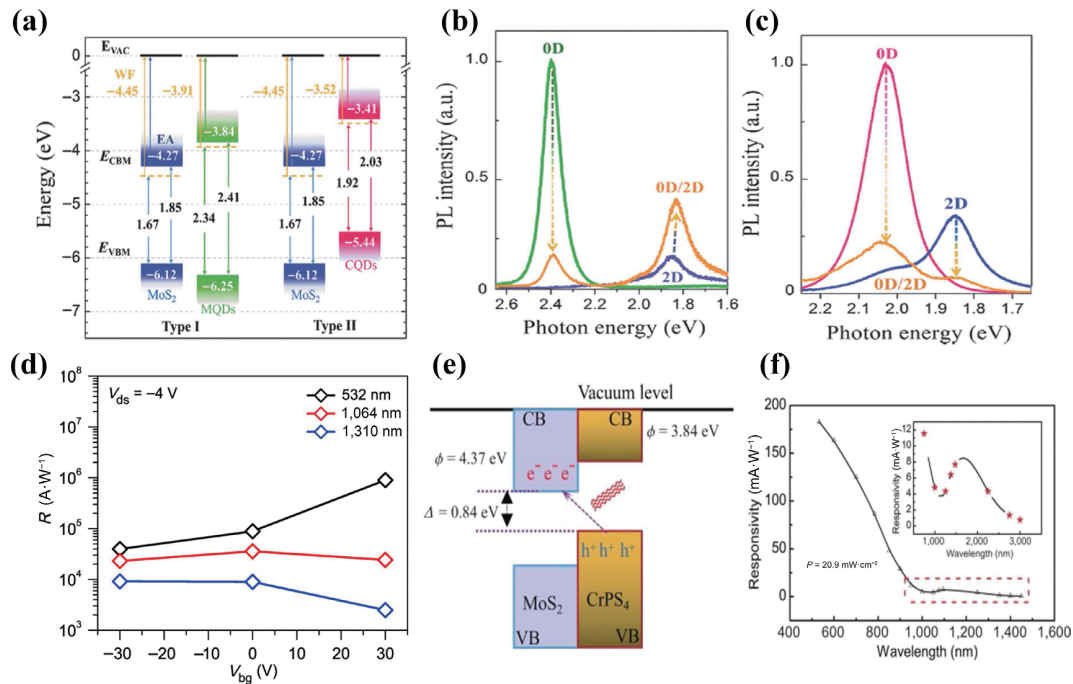
**Figure 4** (a) Band structure diagrams of the two 0D/2D vdW heterojunction (vdWH) interface types: MQDs/MoS$_2$ (left) and CQDs/MoS$_2$ (right). Steady-state PL spectra of (b) MQDs/MoS$_2$ excited by a 442 nm laser and (c) CQDs/MoS$_2$ vdWH on a SiO$_2$/Si substrate excited by a 532 nm laser. Reproduced with permission from Ref. [132], © WILEY-VCH Verlag GmbH & Co. KGaA, Weinheim 2018. (d) $R$ of the p-BP/n-PdSe$_2$ photodetector as a function of $V_{bg}$ at different wavelengths. Reproduced with permission from Ref. [62], © American Chemical Society 2020. (e) The heterostructure of CPS/MoS$_2$ under equilibrium conditions (in the dark). (f) $R$ of the CPS/MoS$_2$ photodetector as a function of wavelength. Reproduced with permission from Ref. [113], © Tsinghua University Press and Springer-Verlag GmbH Germany, part of Springer Nature 2021.

the band offset under an external electric field makes devices possible for applications in different situations.

Regarding infrared photodetectors, the construction of type-II heterostructures with strong interlayer transitions is a promising pathway to achieving high-performance infrared optoelectronic systems. The type-II band alignments expedite the charge separation process and set the stage for electrons and holes to move in the opposite direction, thus enabling spatial separation and the best utilization of photogenerated carriers [136–139]. The charge behavior at the type-II interface can be further modulated by the electric field to enhance the carrier separation [62, 66, 115]. More importantly, since the VBM and CBM of the heterostructure belong to two different materials and the interlayer bandgap is usually much smaller than that of any of the two semiconductors, under infrared illumination with a photon energy lower than the two bandgaps, photogenerated electrons can jump from the VBM of one semiconductor to the CBM of the other semiconductor, breaking the limitation of pristine bandgaps on the photoresponse spectrum range [140–142]. The prediction and proof obtained via density functional theory calculations, PL spectroscopy and Kelvin probe force microscopy verified the strong interlayer transition between the InSe/PdSe$_2$ heterostructure [67]. Photodetectors based on that with a bandgap of 0.853 eV (smaller than the bandgap of InSe and PdSe$_2$, 1.403 and 1.328 eV, respectively) exhibited outstanding photodetection in the NIR region with photoresponsivity, detectivity, and EQE at 1,650 nm up to 58.8 A·W$^{-1}$, 1 × 10$^{10}$ Jones, and 4,660%. Afzal et al. experimentally demonstrated the interlayer optical transition in photodetectors with type-II band alignments based on p-BP/n-PdSe$_2$ [62] and PdSe$_2$/MoTe$_2$ [66]. The remarkable photoresponses at NIR (1,310 nm) were induced by interlayer charge transfer, which was verified via the different trends of responsivity as a function of back-gate voltage ($V_{bg}$) compared with that of the band-to-band transition corresponding with visible photoresponse (Fig. 4(d)). For incident light at visible

wavelengths, the value of the responsivity decreased continuously with a decrease in the gate voltages ($V_{bg} < 0$). The increased effective SBH between the semiconductor and metal electrodes caused a reduction in the collection of photocarriers generated via the band-to-band transitions. However, under infrared illumination, the photoresponsivity increased as $V_{bg}$ decreased. The negative $V_{bg}$ enhanced the built-in field, accelerating the carrier separation and thus increasing the photocurrent.

In this case, some materials showing little response in the infrared region can be utilized as photodetectors via the formation of type-II heterostructures, and the detection range may be extended to SWIR and even MIR, which is critical in telecommunication and the military. A type-II heterostructure photodetector with a subbandgap smaller than 0.8 eV consisting of 2D perovskite with an intrinsic large bandgap and MoS$_2$ exhibited high performance up to the SWIR region, with a responsivity and a specific detectivity of 3.86 A·W$^{-1}$ and 1.4 × 10$^{13}$ Jones at 1,550 nm, respectively [28]. The strong interlayer transition with a reduced energy interval extended the detection range of both individual nanoflakes and endowed the composite device with a sensitive ultrafast response at the microsecond level, which was reduced by three orders of magnitude. A mixed-dimensional photodetector based on a WS$_2$/Si heterojunction was fabricated for IR detection [143] and exhibited a large specific detectivity of ∼ 10$^{13}$ Jones and a fast response speed of 4.5/21.7 μs under 980 nm light illumination. In addition, the type-II band alignment realized broadband detection capability from the deep UV (200 nm) to MIR (3 μm) region.

In some reports, the interlayer excitons in staggered band alignments were mentioned explicitly. Interlayer exciton transitions are likely to dominate the photoresponse when the photon energy is below the cut-offs of the individual materials and above the interlayer transition energy because of the narrow interlayer band, and strong Coulomb interactions between the spatially separated electrons and holes with large binding energy in

different materials still exist and thus form tightly bound interlayer excitons [144, 145]. In this case, the interface accumulates more carriers instead of becoming the depletion region. Thus, in a type-II $CrPS_4$/$MoS_2$-based photodetector, more electron injections from $CrPS_4$ to $MoS_2$ resulted in the offset of quasi-Fermi levels of $CrPS_4$ and $MoS_2$ (Fig. 4(e)) [113]. The wavelength-dependent photocurrent measurement achieved the observation of optical excitation up to 1,450 nm (corresponding to the subbandgap of 0.84 eV induced by strong interlayer coupling) at forward bias. The valley current phenomena at approximately 1,095 nm of 1.2 nA illustrated in Fig. 4(f), which was quite more remarkable than previous reports, probed the existence of interlayer excitons in $CrPS_4$/$MoS_2$.

Usually, allowing for the reduced overlap of the spatially separated electron and hole wave functions, the oscillator strength is expected to be reduced by orders of magnitude compared to that of intralayer excitons in individual monolayers, resulting in a decrease in photocurrent [146]. Nevertheless, a high oscillator strength was realized via sizeable charge delocalization and charge accumulation at the interface in the $WS_2$/$HfS_2$ photodetector, resulting in high absorption that is comparable to intralayer exciton absorption [147]. Moreover, the interlayer exciton accumulation can enhance the electron–hole overlap at the interface, which overcomes the space-indirect character of the interlayer transition. Therefore, operated at room temperature, the type-II device exhibited strong absorption peaks at 0.24 and 0.21 eV for $WS_2$/3 L $HfS_2$ and $WS_2$/bulk $HfS_2$, respectively, a response extended from the MIR to LWIR spectrum of 20 μm under a modest gate bias and a responsivity of $WS_2$/3 L $HfS_2$ photodetector of $8.2 \times 10^2$ A·W$^{-1}$ at 4.7 μm.

However, the problem of high-density thermionic carriers can hardly be overcome in some reported 2D heterostructure photodetectors based on type-II band alignment, which results in an extremely small $I_{photo}/I_{dark}$ and strong temperature dependence that imposes restrictions on the performance of photodetectors [44]. The inescapable thermal noise generated from the disorder-assisted generation–recombination effect leads to the critical weakness of the strong temperature-dependent photodetection process. Although the introduction of a strong built-in electric field is an effective way to suppress the dark current, the strong built-in electric field contributes to the suppression of dark current as well as photoresponsivity, which impedes the detection of incident light with weak power. To suppress interlayer carrier recombination, an hBN dielectric layer was inserted into the type-II InSe/GeS photodetector [148]. The device manifested a photoresponsivity and detectivity of $9 \times 10^2$ A·W$^{-1}$ and $3.4 \times 10^{14}$ Jones, respectively. Additionally, there is a calculation result that the emerging states induced by interlayer coupling could decrease the bandgap abnormally, resulting in the type-I InSe/hBN photodetector having a photoresponse from the infrared to ultraviolet region, implying more possibility in band alignments [149].

## 4.2 Photogating-enhanced designs

PGE is mostly illustrated in nanostructured materials such as QDs [132], nanotubes [150], nanoribbons [151], and 2D layer semiconductors [61], which are utilized as sensitizers onto 2D materials to overcome their intrinsic weak absorption. The mechanism of PGE has been introduced in an earlier section. It can be regarded as a special case of the PCE. The difference in PCE and PGE can be inferred from the $I_{ds}$–$V_g$ and $I_{ph}$–$V_g$ curves. When PGE is dominant, there is a horizontal shift of the $I_{ph}$–$V_g$ trace due to the existing local gate from localized states. Generally, electron–hole pairs are excited under illumination. If the photogenerated electrons or holes become trapped in the defects

or sensitizers, these charged defects could act as an external local gate [152, 153], which would change the channel conductance and modulate carriers transferred into channel materials. Instead of being centers for recombination, these defects in materials with a large surface-to-volume ratio can prolong the carrier lifetime. Thus, some PGE-based infrared photodetectors show high responsivity and large photoconductive gain but limited response speed.

A higher defect concentration of low-dimensional materials contributes to their relatively easier occurrence of PGE characteristics. The random charge distribution at the semiconductor/metal interface, vacancies or grain boundary may lead to a nonuniformity of potential, subsequently forming band tails and adjacent trap states. A $MoTe_2$-based photodetector with a considerable photoresponse in SWIR was realized via PGE [154]. Upon illumination, photon absorption generated electron–hole pairs. In the theoretical explanation, since the Fermi level was closer to the CB, enough localized states near the VB trapped holes, which functioned as a local gate and induced more electrons in the channel, resulting in the leftward shift of the transfer curves. More verifications of this electric gate effect with local trapped charge states were offered from the transfer curves under different incident powers (Fig. 5(a)). As the incident light power increased, the localized traps were gradually occupied, and the threshold voltage changed until they were fully filled. A broad spectral detection range (0.6–1.55 μm) and a $1.3 \times 10^9$ Jones at 1,060 nm under a back gate bias of 10 V were realized.

The variation of band structure with gate voltage was further demonstrated in a BP photodetector that achieved a PGE-induced maximum responsivity of 82 A·W$^{-1}$ at 3.39 μm under 500 mV bias and 1.6 nW incident power [74]. The disorder at the semiconductor/metal interface or defects of BP could cause trap states. Basically, we know that the trap states with energy below the Fermi level are occupied by electrons, and this electronegative property allows them to capture free holes, whereas those whose energy is above the Fermi level are empty to capture free electrons. As the applied gate voltage varied from −10 to 10 V, the change in band alignment is depicted in Fig. 5(b). The Fermi level moved toward the CB with increasing gate bias, and thus, the height of an additional barrier for holes approximately near the drain metal contact was reduced. Although the concentration of free holes in the VB gradually decreased along with the increasing Fermi level, trapped photogenerated electrons still rendered long-lifetime photogenerated holes to transfer between electrodes, leading to the rising photoconductive gain of the transistor and a high photocurrent. At ~ 5 V of $V_g$, the maximum photocurrent occurred (Fig. 5(c)). A further increase in the gate bias resulted in fewer free electrons and holes and an increasing number of trap states to trap photogenerated holes, as well as a decreased photocurrent. When incident light with a higher intensity was applied, the photocurrent peak shifted toward the direction of the higher gate voltage.

However, the photoresponsivity, EQE and specific detectivity of most PGE-based photodetectors all exhibit negative correlations with the optical power intensity. In other words, a higher photodetection performance usually occurs under a relatively small power intensity. The vacancy defects in SnSe films introduced by the magnetron sputtering method induced the PGE mechanism, leading to ultrahigh responsivity with the corresponding high EQE and high detectivity, whose values had a similar trend as mentioned above (Figs. 5(d)–5(f)) [155]. Thus, the 5 nm SnSe with a bandgap of ~ 1.45 eV even reached a responsivity of ~ 3 A·W$^{-1}$ in the device under 980 nm, which was beyond the absorption spectrum. Photodetectors based on Te nanoflakes [156] responded in a wide bandwidth ranging from
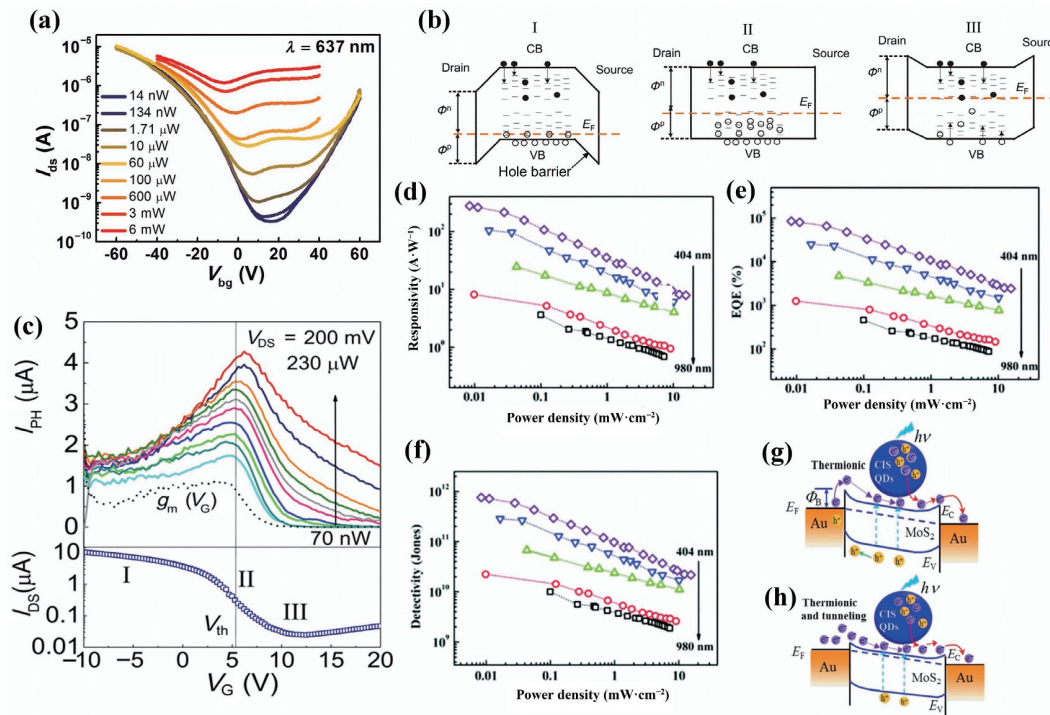
**Figure 5** (a) The transfer curves of MoTe$_2$-based photodetector under different incident light powers ($\lambda$ = 637 nm). Reproduced with permission from Ref. [154], © IOP Publishing Ltd. 2016. (b) The change in band alignment of a BP photodetector as a function of gate voltage, (I) $V_g < V_{th}$, (II) $V_g \approx V_{th}$ and (III) $V_g > V_{th}$. (c) Upper panel: gate-dependent photocurrent measured under a wide range of incident optical powers. The dashed line sketches the gate-dependent channel transconductance for reference. Lower panel: transistor transfer characteristic for $V_{ds}$ = 200 mV. Reproduced with permission from Ref. [74], © American Chemical Society 2016. (d) Responsivity, (e) EQE and (f) detectivity of the SnSe device as a function of laser power densities under different laser wavelengths, including 404, 515, 650, 808 and 980 nm. Considering the large channel region, the bias voltage is 15.0 V. Reproduced with permission from Ref. [155], © The Royal Society of Chemistry 2020. (g) Schematic of the channel current transport mechanism and energy band diagram of the MoS$_2$/CuInSe$_2$-QD hybrid device under illumination and with bias and (h) ON-state: $V_g > V_{th}$, illumination and with bias. Reproduced with permission from Ref. [158], © American Chemical Society 2020.

520 nm to 3.39 μm. At larger incident powers, the decrease in the responsivity clearly proved the PGE, and the peak responsivity of 18 mA·W$^{-1}$ was measured at 3.39 μm under an incident power of 1.6 nW. In addition, because of PGE, high gains up to $3.15 \times 10^4$ were obtained at 3.39 μm. In addition to bare 2D materials, artificial heterostructures combined with zero-dimensional (0D) nanoparticles or QDs with strong light absorption can also induce PGE. Wang et al. demonstrated a 0D-MOF/2D-Bi$_2$Se$_3$ hybrid heterojunction photodetector with an ultrahigh responsivity of 4,725 A·W$^{-1}$ and an outstanding detectivity of $3.5 \times 10^{13}$ Jones at 1,500 nm [157]. The highly porous Ni-CAT-1 (MOF) nanoparticles with a 0.48 eV narrow bandgap acted as a sensitizer to absorb light up to the SWIR region and generated electron–hole pairs, followed by electron transfer to the high-mobility Bi$_2$Se$_3$ channel to contribute to the photocurrent, while holes remained within the sensitizer as a local gate to enhance the photoconductivity gain. The clear nonlinear dependence of the photocurrent ($I_{ph}$) on the power intensity (P), which could be depicted by the power law of $I_{ph} \sim P^x$ ($\alpha$ was fitted to be 0.38), further validated the presence of PGE since $\alpha$ is much smaller than 1 and is related to the dominant photoresponse mechanism of PGE. However, if the value of $\alpha$ is close to 1, the predominance of PCE is confirmed. In other words, the smaller the value is, the larger the contribution to photoconductive gain the PGE makes. In some heterostructure-based photodetectors, the value of $\alpha$ can be tuned by gate-voltage modulation [46, 115], implying conversion between PCE and PGE. In a photodetector based on MoS$_2$/CuInSe$_2$-QDs with a staggered bandgap [158], $\alpha$ was tailored from 0.69 to 0.27 when $V_g$ increased from 0 to 60 V, implying a transformation from PCE to PGE. The effects of type-II alignment, built-in field and trap states at the interface on photogenerated carriers were mentioned in the former part. When

a gate voltage larger than the threshold voltage was applied to the device, the SBHs between the electrodes and MoS$_2$ decreased, and then the thermionic current and tunneling current increased with increasing $V_g$ (Figs. 5(g) and 5(h)). Hence, under a larger gate voltage and the synergy of PGE and SBHs modulation, the device reached an ultrahigh photoresponsivity of 74.8 A·W$^{-1}$ and detectivity of $7.1 \times 10^{11}$ Jones at 1,064 nm. Similarly, $\alpha$ being tuned from $\sim$ 0.98 to 0.12 under varied gate modulation from −50 to 50 V was found in PbSe QDs/Bi$_2$O$_2$Se photodetectors, rendering a sensitive infrared responsivity more than $10^3$ A·W$^{-1}$ at 2 μm [142]. In addition, a larger positive gate voltage also decreased the strength of the charge-transfer dipole at the interface, which impeded carrier separation. However, a larger back gate voltage may also increase the dark current, which decreases the total current between the source and drain. This is not favorable for device performance.

## 4.3 Surface plasmon designs

An alternative to light sensitizers for 2D infrared photodetectors has been based on plasmonic metal nanostructures. As a prospective approach, plasmonic nanostructures exhibit appealing advantages in improving the light–matter interaction, tuning the absorption spectrum and further enhancing the photoresponse of 2D-based infrared photodetectors. Typically, surface plasmon interactions can be classified into localized surface plasmons (LSPs) and surface plasmon polaritons (SPPs) [159, 160]. SPP is a kind of electromagnetic excitation coupled with the collective oscillation of electrons occurring at the metal–dielectric interface, and the realization of oscillation in SPPs requires special experimental arrangements to match the wave vector [160]. Compared with SPPs that transmit along the interface, LSPs without transmission and requirements of matching wave vectors

occur on the surface of metallic nanostructures whose geometric parameters are smaller than the wavelength of incident light. Usually, the collective oscillation will be amplified if the frequency of incident light is the same as the free electron frequency and resonance occurs. Since the collective oscillation is localized at the surface of the nanostructures, light absorption is greatly enhanced. The specific incident light can either generate hot electrons induced by the nonradiatively decayed plasmons to increase photocurrents [161, 162] or be trapped at the interface by collective oscillation of free electrons to enhance the light absorption [10]. For example, the strong coupling of $MoS_2$ and grating of metallic $Mo_2C$ (Fig. 6(a)) at the interface provided a significantly low SBH, benefiting efficient hot carrier transfer from nanostructures to the channel upon illumination [163]. The photoexcited carriers were verified to be generated in the plasmonic p-$MoC_2$ stripes, which supported the transformation from plasmons to hot carriers. The peak photoresponse can be adjusted from the visible to NIR region by tuning the period width and quantity of the $Mo_2C$ grating, achieving a photoresponsivity up to $10^3$ A·$W^{-1}$.

For metal materials to realize surface resonance, gold is the most common choice [164, 165]. The localized surface plasmon resonance (LSPR) of Au has been widely utilized for photoelectric field enhancement and in photochemical reactions occurring at specific wavelengths associated with phase relaxation from plasmon states. Au nanoparticles were integrated onto few-layer $MoS_2$ via magnetron sputtering and realized a strong LSPR [166]. The simulated electric field distribution illustrated the resonance of the Au nanoparticle surface plasmon under matched 980 nm incident light. As Figs. 6(b) and 6(c) illustrate, the intensity of the electric field at the interfaces of air/Au/$MoS_2$ (up to ~ 3.96 × $10^5$ V·$m^{-1}$) was much higher than that in other areas and larger than that of air/$MoS_2$ without the plasmonic nanoparticle-induced LSPR effect (~ 6.72 × $10^4$ V·$m^{-1}$), which contributed to the subsequent separation of electron–hole pairs. The normalized absorption of Au nanoparticles was enhanced compared to that of pure $MoS_2$ in the range of 700–1,600 nm of illumination wavelength, promoting the utilization of incident light. Thus, the photodetector based on this hybrid structure exhibited a photoresponsivity of 64 mA·$W^{-1}$ at 980 nm, which was much higher than that of pristine $MoS_2$.

Compared with the metal grating, the gold plasmonic cavity exhibited a great enhancement in the local field and light absorption of graphene photodetectors and even realized polarization infrared detection experimentally [167]. The cavity resonance is based on the constructive interference of the plasmonic waveguide mode. The graphene was sandwiched above a gold layer by a bottom $Al_2O_3$ dielectric spacer and a group of Au
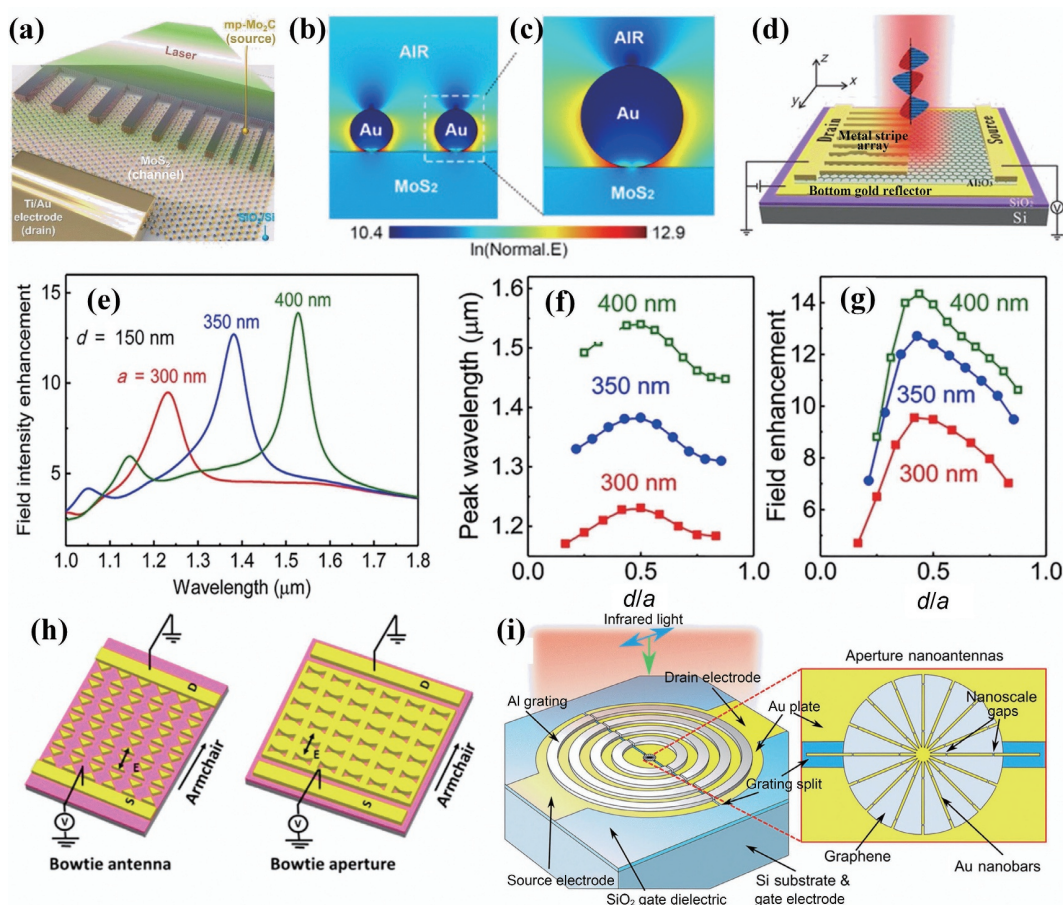


**Figure 6** (a) Schematic illustration of $MoS_2$/mp-$Mo_2C$ photodetector device with illumination. Reproduced with permission from Ref. [163], © WILEY-VCH Verlag GmbH & Co. KGaA, Weinheim 2019. Simulated electric field distribution of the cross-section of (b) the sensing layer consisting of Au NPs and few-layer $MoS_2$ and (c) interfaces at air/Au/$MoS_2$. The rainbow bar indicates the logarithmic scale of the intensity of the normal electric field. Reproduced with permission from Ref. [166], © Elsevier B. V. 2019. (d) Schematic of the plasmonic cavity-integrated graphene phototransistor. Reproduced with permission from Ref. [167], © Zhang, D. H. et al. 2019. (e) Near-field intensity enhancement spectra with the hole diameter $d$ = 150 nm and various array periods $a$ = 300, 350 and 400 nm at normal incident radiation with a circular polarization. (f) The wavelength of the dominant field enhancement peaks and (g) the maximum value of the field intensity enhancement factor as a function of the hole diameter for $a$ = 300, 350 and 400 nm. Reproduced with permission from Ref. [169], © Elsevier B. V. 2020. (h) Au resonant plasmonic structures, bowtie antennas and bowtie apertures. Reprinted with permission from Ref. [29], © American Chemical Society 2018. (i) Cartoon illustrating the proposed LWIR photodetector consisting of a hybrid plasmonic structure and a zoomed view of the aperture nanobar antennas. Reproduced with permission from Ref. [170], © Azar, N. S. et al. 2019.

stripes (also referred to as the plasmonic cavity array) on the top (Fig. 6(d)). The mechanism of a polarization extinction ratio up to 30 was explained as follows. The polarization perpendicular to the stripes (transverse magnetic waves) resonantly excited the intensified local field near the graphene, resulting in a great absorption in graphene; for the polarization along the stripes (transverse electric waves), the suppressed absorption of graphene could be ascribed to the reflection of most light intensity. At the resonant wavelength of 1.55 μm, the incident light was efficiently converted into a localized field that strongly interacted with graphene, leading to a maximum responsivity of 0.18 V·W$^{-1}$ under transverse magnetic waves, which was 30-fold higher than that under polarized light parallel to the metal stripes due to the enhanced localized field.

It is obvious that the resonant wavelength range of LSPs or SPPs is tunable by adjusting the geometric parameters of the nanoparticles. Different nanostructures may realize tunable peaks at different desired wavelengths. For example, 5.9 is an ideal length–diameter aspect ratio for Au nanorods to obtain the plasmon extinction peak at 940 nm [165]. At this ratio, the concentration of the nanorod solution had a sensitive effect on the photoresponse of nanorod/2D PtSe$_2$ photodetectors. Nanorod solutions with concentrations varying from 1 to 50 nM (0.5, 1, 5, 10, 25, and 50 nM) were spin-coated on the PtSe$_2$ films. A high photocurrent was observed in 2D PtSe$_2$ combined with 5.0 nM Au nanorods, which was approximately fivefold higher than that of bare 2D PtSe$_2$. On the other hand, the photocurrent decreased as the Au nanorod concentration exceeded 10 nM. The increase in leakage current could be ascribed to the formation of false transport channels because the spacing between the Au nanorods was less than the mean free path of the hot electrons. It is noteworthy that different concentrations ultimately result in different rod-to-rod distances, which is quite similar to the arrangement of hole arrays on perforated Au films. Numerical simulation results have suggested that 2D arrays of subwavelength holes with different diameters in a gold film serve as meta-surfaces supporting the conversion of external electromagnetic NIR radiation into surface plasmon modes at the Au/Si interface [168]. The surface plasmon modes could also be tuned by the period of arrays [169] at the telecom wavelength region. The field intensity enhancement factor and its spectral position as a function of hole diameter are illustrated in Figs. 6(e)–6(g). For holes with smaller diameters, the spectral position shifted towards longer wavelengths, and the positive correlation between enhancement and periodicity was ascribed to the interference of the SPPs Bragg scattered by the holes in an array. At a ratio of hole diameter to array periodicity of 0.5, the maximum peak wavelength and field intensity enhancement were realized. A field intensity enhancement over 14 times was obtained at 1.54 μm for hole diameter and array periodicity values of 200 and 400 nm, respectively. Enhanced photosensitivity and polarization selectivity of black phosphorus photodetectors were realized via Au resonant plasmonic structures, bowtie antennas and bowtie apertures, respectively (Fig. 6(h)) [29]. Under 1,550 nm illumination, the bowtie antennas led to an LSP-reduced enhancement of 70% in the photoresponse and more than 4-fold responsivity at a low photodetector bias, and the bowtie apertures suppressed the photocurrent in the zigzag direction of BP, realizing an armchair to zigzag photocurrent ratio of 8.7. To collect and concentrate light into a monolayer graphene photodetector, Azar et al. utilized a precisely designed metallic bull's eye grating and optical nanoantennas (Fig. 6(i)) [170]. The SPP-induced interaction between graphene and light improved the photodetection performance in the LWIR region, with the light absorption of graphene enhanced by 558 times and the detectivity of the LWIR

photodetector enhanced by 32 times.

The extraordinary optical transmission (EOT) of metal plasmonic grating slits also plays a role in enhancing photoabsorption [171]. Greatly enhanced transmission can be obtained by adjusting the geometric dimensions of the metal grating slits. In addition, the absorption property and tunable anisotropic plasmonic response up to the MIR region and even further in different dimensions of BP nanoribbon arrays along the armchair and zigzag directions [172, 173] can also be helpful to develop novel infrared photodetectors. The combination with the metal grating increased the absorption of BP from 72% to 83.6% at 7.04 μm [171]. The absorption characteristics of the hybrid structure based on the combination of the LSPR and EOT effect were beyond expectation that the enhanced absorption can be achieved up to 99.92% at the resonance wavelength of 8.9 μm.

In addition to conventional metallic elements [174, 175], some semimetals or heavily doped semiconductors, such as MoO$_x$ [176], TiN [177], Cu$_2$S [178, 179] and Fe$_{1-x}$S$_2$ [180] with high carrier concentrations have also been suggested for surface plasmon resonance in the infrared region, which usually requires variation of the stoichiometry and geometry size of the semiconductors. A WS$_2$/Si photodetector containing oxygen-doped WS$_2$ microrods composed of layer-by-layer stacked nanosheets and a top graphene electrode with silver coating exhibited broadband NIR absorption beyond 1,100 nm [181], which could be ascribed to the oxygen-incorporation-induced LSPR effect. The formation of 25WS$_2$·15WO$_{3-x}$ ($x$ = 2.33) was verified by the atomic ratio of tungsten to sulfide to oxygen estimated to be 4:5:1, and the intensive broadband NIR absorption could be attributed to the LSPR of free charges in oxygen-deficient WO$_{3-x}$. Additionally, assisted with a built-in field at the interface of the heterostructure, a decent responsivity of 1.5 A·W$^{-1}$, a high specific detectivity close to 2 × 10$^{12}$ Jones, fast response speeds with rise/fall time of 2.0/7.2 μs, and good ambient stability (2 months) at zero bias were realized in the photodetector.

Moreover, as a semimetal, graphene can also support surface plasmon resonances. Electrical adjustments can endow graphene plasmons with a high degree of electromagnetic confinement property from MIR to terahertz wavelength, and facilely designed nanostructures can further enhance the field intensity [182]. A graphene/graphene MIR photodetector consisting of plasmonic resonator arrays interconnected by quasi-one-dimensional graphene nanobelts was reported by Guo et al. [183]. The obvious edge roughness in the nanostructures induced disordered localized states, which formed the dramatic temperature-dependent carrier transport characteristic and enabled the electrical detection of plasmon decay near the graphene resonators. Operated at 12.2 μm and room temperature, this device exhibited a subwavelength footprint of 5 μm × 5 μm with an external responsivity of 16 mA·W$^{-1}$ and a low noise-equivalent power of 1.3 nW·Hz$^{-1/2}$. Sun et al. demonstrated another plasmonic-enhanced MIR room-temperature photodetector by fabricating graphene nanoresonators/graphene heterostructures [184]. The plasmon polaritons in graphene nanoresonators are size-dependent with strong field localization.

## 4.4 Ferroelectric-enhanced designs

Combined with 2D materials, ferroelectric materials have been proven to enhance the performance of infrared photodetectors from many aspects [185]. The ferroelectric polarization field provided by the ferroelectric gate can modulate the carrier density in channel materials and dramatically enhance the photoconductive properties of the devices. For ferroelectric materials, one important characteristic is that the intensity and direction of spontaneous polarization in a specific temperature

range can be tuned by the external bias due to the rotation of domains. The influence of the electric field on the polarization is depicted by the electric hysteresis loop. The polarization direction of the domains will remain constant under an external voltage exceeding the coerivity voltage of the ferroelectric materials. After the removal of the applied bias, a residual polarized electric field is formed in ferroelectric materials, which can remarkably deplete the channel [186] to suppress the dark current in the channel over a long duration without additional gate bias, causing less energy consumption [187]. The residual polarization usually behaves in three states [188–190], which are the nonpolarized state, polarization upwards state and polarization downwards state (illustrated in Figs. 7(a)–7(c)). Thus, coupling polarized ferroelectrics with 2D photodetectors can be a reliable approach to achieve high performance.

Ferroelectric 2D $\alpha$-In$_2$Se$_3$ with strong absorption in the IR region can directly build heterojunctions such as WS$_2$/$\alpha$-In$_2$Se$_3$ [191] and BP/$\alpha$-In$_2$Se$_3$ [192] to function as photodetectors. Tunable polarization in $\alpha$-In$_2$Se$_3$ requires no need for an additional ferroelectric gate, which might be a promising approach in addition to the gate dielectric. Nevertheless, at present, most reports are only based on the ferroelectric gate to enhance the photoresponse. LiNbO$_3$ [193], lead zirconate titanate (PZT) [194] and organic ferroelectric poly(vinylidene fluoride-trifluoroethylene) (P(VDF-TrFE) for short). Among them, P(VDF-TrFE) is widely chosen as the gate dielectric due to its transparency. When an applied bias larger than the coerivity voltage is applied, the molecular chains of P(VDF-TrFE) are neatly arranged and polarized in a direction. A well-performing flexible photodetector based on ReS$_2$ and P(VDF-TrFE) was demonstrated by Tai et al. [195]. The upwards polarization state modulated the full depletion of the ReS$_2$ channel, implying an

ultralow dark current in the photodetector. At an incident wavelength of 830 nm, the device with a ferroelectric top gate on a polyimide substrate achieved a responsivity of 11.3 A·W$^{-1}$, and a detectivity of $1.7 \times 10^{10}$ Jones at zero gate voltage. The response time reached 6.1 ms. In addition, the polyimide substrate was fixed on several homemade curved surfaces to produce different strains. The dark current decreased under small strain and increased under larger strain (Fig. 7(d)). Under 0.08% strain, the photoresponse reached the maximum, and the detectivity and responsivity were 1.8 times and 2.6 times those without bending (Fig. 7(e)). The changes induced by the strains were reversible.

Another significant aspect is that the polarization direction on both sides of P(VDF-TrFE) could be modulated independently to build a p-n junction in ambipolar MoS$_2$ and graphene without element doping or stacking different materials [30, 196], which is a facile pathway for better photoresponses. As illustrated in Fig. 7(f), Wu et al. realized ambipolar MoTe$_2$ to form ferroelectric-modulated homojunction photodetectors [197]. A downwards polarization state beneath MoTe$_2$ induced hole accumulation near the semiconductor/ferroelectric interface in MoTe$_2$, leading to p-type doping. An upwards state on the other side of the polymer resulted in n-doping. Thus, a p-n homostructure was formed, which could be further converted into n-p, n-n, and p-p structures under an external gate bias (Fig. 7(g)) and exhibited different photoelectric properties (Fig. 7(h)). The device based on a nonvolatile p-n homosturcture presented 0.5 A·W$^{-1}$ and $3 \times 10^{11}$ Jones at 1,310 nm.

The challenging extension of the absorption spectrum range can also be realized by varying the electric field. Reversing the polarization direction even switched the band alignment of GeSe/MoS$_2$ vdW heterojunctions between type-I and type-II, and the corresponding photodetectors realized high photoresponsivity
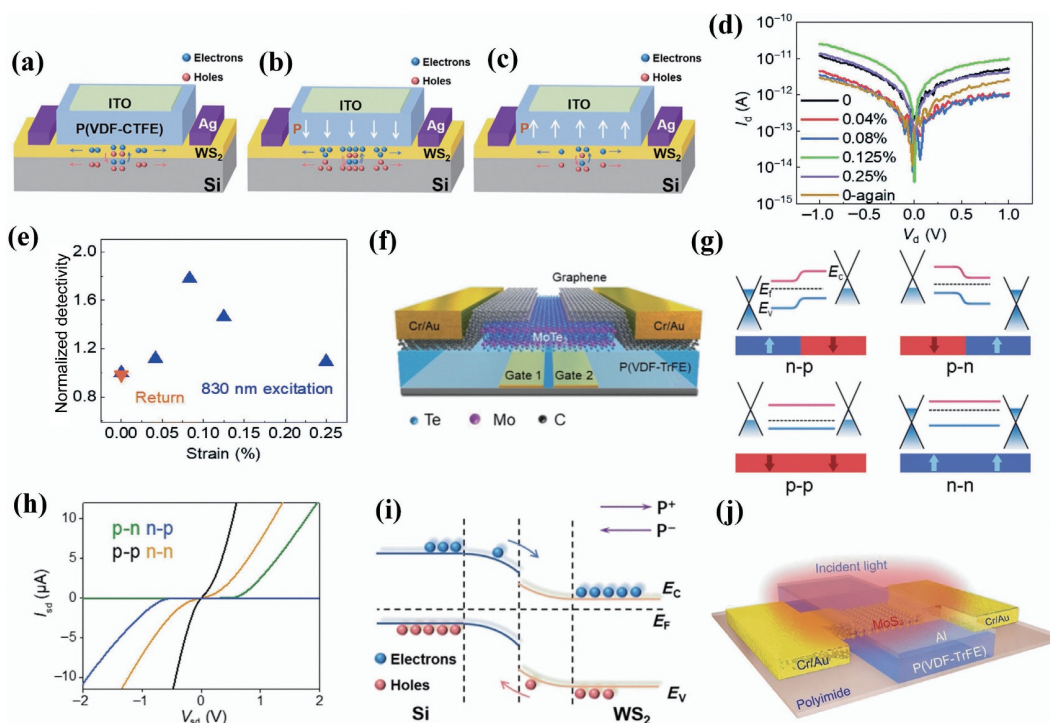


**Figure 7** Schematic diagrams of the carrier movements at the (a) nonpolarization state, (b) downwards state and (c) upwards state. Reproduced with permission from Ref. [188], © WILEY-VCH GmbH 2021. (d) The dark currents of the ReS$_2$ phototransistor under different strains. The '0' state is the state before bending and after polarization. The '0-again' state is the state that returns to the '0' state after bending. (e) Normalized detectivity of the ReS$_2$ phototransistor under strain. Reproduced with permission from Ref. [195], © The Royal Society of Chemistry 2022. (f) Schematic of the device structure and (g) band diagrams for different device configurations. n–p/p–n: the left of P(VDF-TrFE) is polarized up/down, and the left of P(VDF-TrFE) is polarized down/up. p–p/n–n: both sides are polarized down/up. (h) $I_{sd}$–$V_{sd}$ curves in different ferroelectric domain configurations. Reproduced with permission from Ref. [197], © WILEY-VCH Verlag GmbH & Co. KGaA, Weinheim 2020. (i) Band structure of the WS$_2$/Si heterojunction. Reproduced with permission from Ref. [188], © WILEY-VCH GmbH 2021. (j) Schematic of MoS$_2$-based photodetector with P(VDF-TrFE). Reproduced with permission from Ref. [199], © Wang, X. D. et al. 2019.

from visible to near-infrared wavelengths [198]. Zheng et al. achieved the photoresponse of a WS$_2$/Si photodetector up to NIR, which broke through the intrinsic bandgap limitation on the spectral absorption of WS$_2$ [188]. The band structure of WS$_2$/Si is illustrated in Fig. 7(i). At the polarization downwards state, the polarized electric field remained in the same direction as the built-in electric field, which promoted carrier separation in the depletion layer and enhanced the carrier concentration on both sides of the heterojunction. The sensitivity of lateral PVE was also promoted from 198.6 to 503.2 mV·mm$^{-1}$ due to a smaller barrier height. Moreover, along with the residual electric field induced by the threshold bias on the poly(vinylidene fluoridechlorotrifluoro-ethyelene) (P(VDF-CTFE)) gate increasing from 0 to 1 V·nm$^{-1}$, the indirect bandgap gradually decreased from 1.2 to 0.58 eV by DFT calculations. Thus, in the downwards state, the photocurrent at 1,550 nm was greatly enhanced compared to that in the nonpolarized state. A fast response speed of 2.4/8.5 μs was realized at 980 nm due to the lower energy consumption for crossing the depletion layer.

In a MoS$_2$-based photodetector (Fig. 7(j)) demonstrated by Wang et al., an ultrabroad response spectrum from 375 nm to 10 μm was realized via the integration of a hybrid quasi-freestanding structure of P(VDF-TrFE) [199]. Although the bandgap of MoS$_2$ was narrowed to a certain extent, the photoresponse to photon energy that was too far below the bandgap energy to excite carriers could not be ascribed to MoS$_2$. Instead, it was the pyroelectric effect induced by the ferroelectric materials that worked. The upwards polarization mode was chosen to suppress the dark current. Without illumination, holes in MoS$_2$ were bound by the upwards remnant polarization field at the interface, leading to an extremely small dark current. Under illumination ranging from MIR to LWIR, the charge on both sides of P(VDF-TrFE) decreased with the reduced polarized field induced by heat. Consequently, fewer bounded holes in MoS$_2$ elevated the Fermi level and led to more electrons flowing through the channel and a larger photocurrent. The thin polyimide substrate with a thickness of 1.7 μm allowed more heat to be absorbed by P(VDF-TrFE), leading to a higher sensitivity to the pyroelectric effect. A high responsivity of 140 mA·W$^{-1}$, an on/off photocurrent switching ratio up to 10$^3$, and a quick response of 5.5 ms were achieved in the MIR to LWIR region.

In addition, the polarization electric field can passivate the surface defects of few-layer materials [189, 200]. Compared with devices without the P(VDF-TrFE) passivation layer, the dark current of 2D InSb photodetectors was two orders of magnitude lower, and the responsivity was 20 times higher (311.5 A·W$^{-1}$); the photoresponse time was shortened from seconds to the order of milliseconds, and the detectivity at 940 nm reached 9.8 × 10$^9$ Jones, respectively [201]. The surface of the InSb nanosheets was covered by a 3 nm-thick thin layer of natural oxide that absorbed oxygen molecules and captured electrons in InSb to form trap states O$_2^-$, behaving like the p-doped samples. Thus, photogenerated holes would first fill the electron traps. Many surface trap states will slow down the photocurrent stabilization process in carrier separation and prolong the dark current stability in carrier recombination, making both the rising time and the decading time longer. Therefore, the P(VDF-TrFE) layer could isolate oxygen adsorption and encapsulate surface defects. The upwards polarization was favored for the InSb NS devices working in the OFF state (where the dark current was small) without an additional gate voltage.

## 4.5 Other structure designs

In addition to plasmonic structures, optical cavities and waveguides are used to improve the photoresponse of photodetectors because of the enhancement of light absorption of 2D materials [202]. To enhance the photoresponse performance, the vertical heterostructure is also demonstrated as a revolutionary design. The vertical nanoflakes deposited onto the lateral layer can greatly benefit light absorption by enhancing the surface area [203]. Moreover, the response speed as well as the photoresponsivity and detectivity can be improved due to the special carrier transport direction along the vertical intralayer to the top electrode [204]. In a SnS/Si photodetector reported by Yao et al. [205], both lateral and vertical SnS nanosheets aligned on three-dimensional (3D) silicon via pulsed-laser deposition were observed, as illustrated in Fig. 8(a). Yellow dotted lines circle the lateral parts, while white dotted lines circle the vertical parts. The heterostructure device realized a multicolor response from UV to NIR (370–1,640 nm), exhibiting a high responsivity up to 273 A·W$^{-1}$, a detectivity of 7 × 10$^{13}$ Jones and a remarkable EQE of 4.2 × 10$^4$%. The schematics of the carrier dynamics of lateral (Fig. 8(b)), vertical (Fig. 8(c)), and both lateral and vertical alignments (Fig. 8(d)) explained these excellent photodetection performances, which are far better than those of 2D/3D heterostructure photodetectors containing either lateral or vertical 2D materials. For laterally aligned heterostructures, wide and large vdW barriers between monolayers restricted carrier transportation along the purple arrows and caused high recombination. For the vertically aligned heterostructure, a large number of defects resulting from deformation at the interface of the heterojunction acted as combination centers and carrier traps. Thus, in the mixed situation, good contact between SnS and Si, which could be ascribed to lateral alignments without dangling bonds, suppressed carrier combination, and the vertical nanosheets provided a high-conductive channel for effective carrier transfer. In addition, a vertically stacked p-n-p hybrid heterostructure photodetector (Fig. 8(e)) consisting of BP-MoS$_2$-Si also improved the photoresponse [206]. The novel vertical structure was designed to build two opposite electric fields (Fig. 8(f)) for independent detection in the NIR and MIR ranges. The n-type MoS$_2$ plays the role of electron collection and as a hole barrier layer, while p-type Si and BP are used to absorb NIR and MWIR radiation, respectively. The two-color photodetector exhibited outstanding performance with a specific detectivity of 6.4 × 10$^9$ Jones at 3.5 μm and room temperature.

Most photodetectors work on the same mechanism as p-n diodes. However, Lee et al. demonstrated a PIN working mode for photoresponse enhancement based on a homogeneous MoTe$_2$ junction photodetector (Fig. 8(g)) [207]. Compared with the pristine PN mode, the MoTe$_2$ photodetector based on the PIN mode exhibited remarkable optical absorption at 1,300 nm, which could be ascribed to the bandgap reduction induced by the Franz-Keldysh effect. The lateral seamless PIN diode was obtained by two gates that separately influenced the P and N regions, forming the strong built-in field named the I region even after the formation of a chemical p-n junction. The preexisting depletion layer in the p-n junction was enhanced. Thus, as Fig. 8(h) illustrates, $V_{GP}$ and $V_{GN}$ functioned together to obtain the P$^+$, N$^+$, and I regions. The much stronger and wider photocurrent mapping intensity of the PIN mode could be ascribed to the greater depletion width of the PIN mode. The photoresponsivity under PIN mode achieved 1.6 A·W$^{-1}$ at 1,300 nm, which was an order of magnitude higher than that under the PN mode.

Unipolar barrier photodetectors show advantages in dark current suppression to realize a high operating temperature compared with p-n junction infrared photodetectors. Different from the strict lattice matching requirements of traditional superlattice-based unipolar barrier devices [208], photodetectors based on 2D materials possessing self-passivated surfaces may
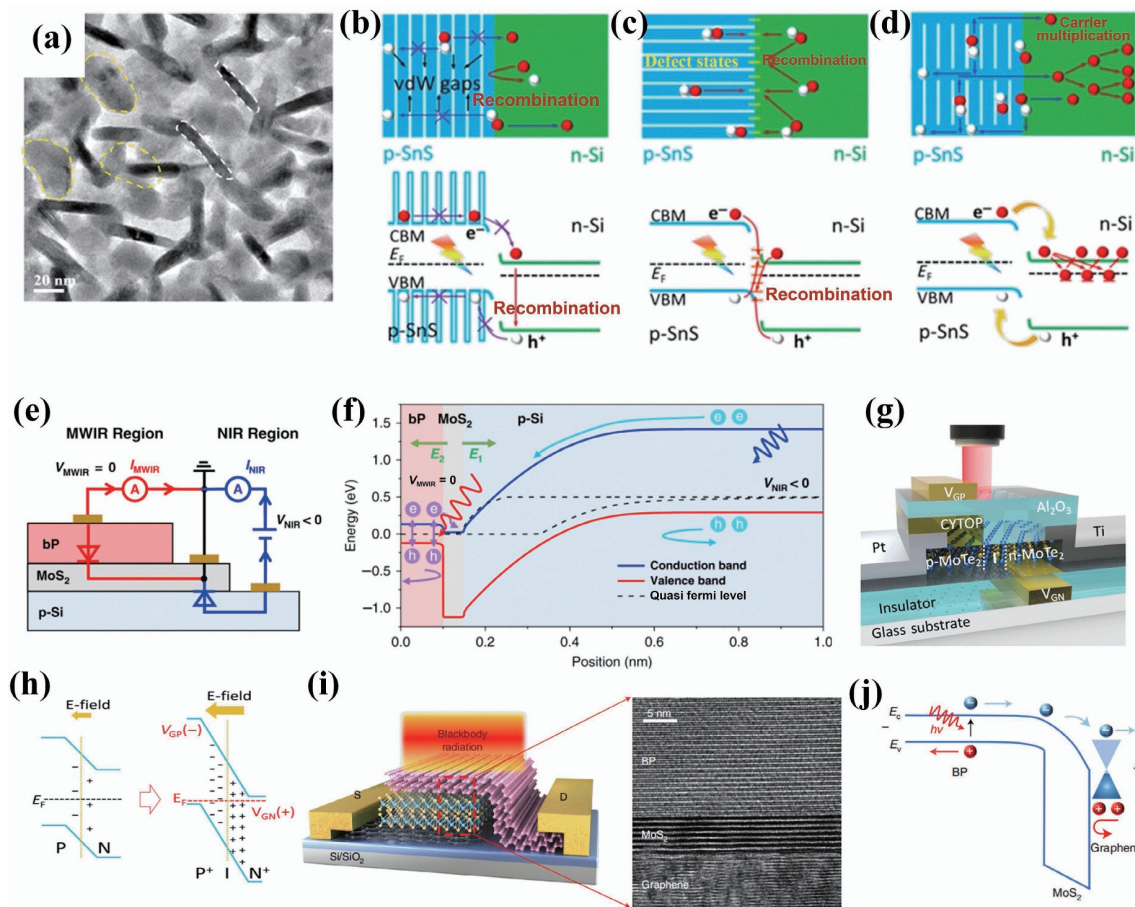
**Figure 8** (a) High-magnification TEM image of SnS nanofilms and (b) laterally aligned, (c) vertically aligned and (d) both laterally and vertically aligned 2D layered materials. Reproduced with permission from Ref. [205], © American Chemical Society 2018. (e) Circuit configuration of the device to demonstrate the performance of the two-color photodetector. (f) Simulated energy band diagram with p-Si applied to a negative voltage. Reproduced with permission from Ref. [206], © Wu, P. S. et al. 2022. (g) Schematic of the homogeneous MoTe$_2$ photodetector. (h) Schematic band diagrams of two operating modes: PN and PIN. Reproduced with permission from Ref. [207], © WILEY-VCH Verlag GmbH & Co. KGaA, Weinheim 2019. (i) Schematic diagram of the BP/MoS$_2$/graphene pBp vdW unipolar barrier MIR photodetector under blackbody radiation. Inset: cross-sectional TEM images of the overlapped region. (j) Corresponding band diagram of a pBp vdW unipolar barrier device under the reverse bias condition. Reproduced with permission from Ref. [209], © Chen, Y. F. et al. 2021.

fundamentally avert the mismatch. In a recent breakthrough, Chen et al. utilized band-engineered vdW heterostructures to construct visible and MIR unipolar barrier photodetectors [209]. For the MIR region, the pBp unipolar barrier photodetectors consisting of a BP p-type absorber, MoS$_2$ barrier and graphene contact layer (a BP/MoS$_2$/graphene heterostructure, illustrated in Fig. 8(i)) exhibited a detectivity of $2.3 \times 10^{10}$ Jones in the MIR region under blackbody radiation at room temperature. As Fig. 8(j) illustrates, the barrier functioned as a block layer of the movement of majority carriers in the absorption layer and controlled the depletion region of the Shockley–Read–Hall (SRH) current to transfer to the barrier layer with a large bandgap, leading to an obvious reduction in the SRH current. Even though the n-type MoS$_2$ barrier layer might introduce a depletion region that caused the SRH current, the high-doping and high-mobility graphene contact exhibited effective charge collection as well as ideal ohmic contact with the Cr/Au electrode, which further reduced the potential barrier during electron transfer. Thus, the pBp photodetector achieved a dichroic ratio of 4.9 under blackbody radiation that only a few 2D materials could reach and a response speed of 28/23 μs at 2 μm.

# 5 Applications of 2D-based infrared photodetectors

Infrared photodetectors can be used as the collecting terminals of on-chip sensing (spectrometers, sensors, etc.) signals, the receiving terminals of radar and other equipment to acquire data, and the focus plane arrays for thermal imaging. In this section, 2D-based infrared photodetectors for free-space image sensing, flexible optoelectronic devices, and on-chip integration will be mainly introduced.

## 5.1 Image sensing

Although the electronic and optical properties of 2D materials can be controlled by doping, strain, and other means, it is difficult to achieve large-scale applications with these methods. Therefore, performance enhancement and modulation actualized by structure designs becomes a pathway with more potential.

Infrared focus plane arrays (IR FPAs) have been broadly applied in military infrared imaging or temperature measurement for industry. The type-II superlattice (T2SL) and HgCdTe infrared photodetectors perform well in the present market. Research on 2D-based infrared photodetectors for IR FPA was also carried out. MXene/perovskite/MXene-based infrared photodetectors were applied to large-scale image sensor arrays consisting of $25 \times 50$ pixels [122]. As Fig. 9(a) illustrates, the sensor arrays were fabricated via alternate spin-coating and direct laser-scribing. The three-layer $25 \times 50$ pixel image sensor array is demonstrated in Figs. 9(b) and 9(c), and the individual functional pixels were separated precisely from Fig. 9(d). The energy level alignment between Ti$_3$C$_2$T$_x$ nanosheets and (CsPbI$_3$)$_{0.05}$((FAPbI$_3$)$_{1-x}$(MAPbBr$_3$)$_{0.5x}$(MAPbI$_3$)$_{0.5x}$)$_{0.95}$ favored efficient charge transfer, while the absorption limitation of the perovskite led to a decrease
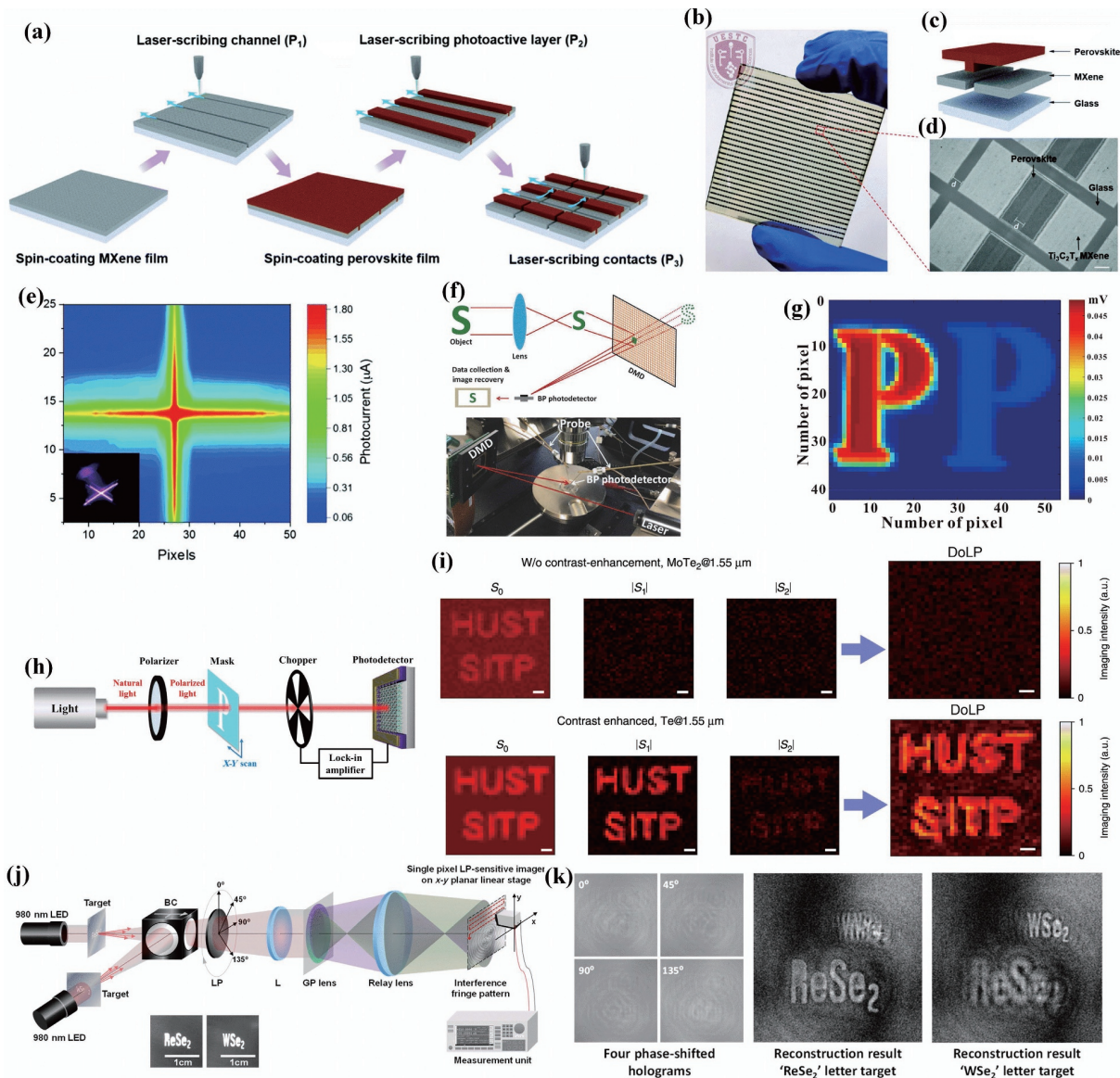
**Figure 9** (a) Schematic of the fabrication process of the MXene/perovskite/MXene image sensor arrays. (b) Image of the sensor arrays. (c) Schematic of a single pixel. (d) Optical image of a single pixel with MXene electrodes and a perovskite photoactive layer (scale bar, 200 μm). The channel width of the MXene electrodes is 120 μm. The effective photoactive and electrode areas of a pixel are ~ 800 μm× 580 μm and ~ 800 μm × 650 μm respectively. (e) The image captured by the image sensor arrays under NIR illumination. The inset image was obtained using a digital camera with an IR filter under the 808 nm laser pattern. Reproduced with permission from Ref. [122], © The Royal Society of Chemistry 2020. (f) Schematic and photograph of the experimental setup for imaging an object. Reproduced with permission from Ref. [80], © WILEY-VCH Verlag GmbH & Co. KGaA, Weinheim 2017. (g) Imaging results of "P" letter under 780 nm with polarization angles of 0° (left) and 90° (right). (h) Schematic illustration of the measurement system for polarization-sensitive infrared imaging. Reproduced with permission from Ref. [72], © American Chemical Society 2019. (i) Imaging DoLP results for the nonpolarized 2H-MoTe$_2$ device and Te device under 1.55 μm illumination for comparison. The DoLP is almost 0, indicating that the MoTe$_2$ device shows no polarization detection ability, which is not applicable for polarized imaging in scattering environments. Reproduced with permission from Ref. [211], © Tong, L. et al. 2020. (j) Schematic of the holographic recording system consisting of a rotating linear polarizer, geometric-phase (GP) lens, and NIR LP-sensitive photodetector. The insets show two targets. The green and violet beams after the GP lens indicate the converging and diverging beams, respectively. BC, beam combiner; LP, rotatable front linear polarizer; L, objective lens. (k) Left: four phase-shifted holograms; right: focused reconstruction of the "ReSe$_2$" letter target and the "WSe$_2$" letter target, illustrating reconstructions of different focused depths. Reproduced with permission from Ref. [212], © American Chemical Society 2021.

in the responsivity and specific detectivity when the wavelength was larger than 532 nm. The minimum values appeared at 808 nm. Regarding the imaging ability, this array could resolve the weak NIR laser signal of 121.0 μW·cm$^{-2}$ and imaged a cross-shaped pattern (Fig. 9(e)).

Single-pixel imaging attracts much attention due to the higher sensitivity, detection efficiency, and better imaging quality for weak signals or in scattering environments. A WS$_2$/Si photodetector with type-II band alignment exhibited a broad response of up to 3 μm [143]. Functioned as a single pixel sensor, the electrical signals of the detector were captured by a lock-in amplifier. As a result, the voltage contrast ratio of the image was as

high as 6 × 10$^3$, which demonstrated the high-resolution imaging ability. Miao et al. combined a single-pixel few-layer BP FET photodetector with a digital micromirror device (DMD) functioning as an infrared camera [80]. With the help of compressive sensing algorithm, limited signal samples were required to reconstruct the original image. As Fig. 9(f) illustrates, the infrared light was first projected onto the DMD instead of the photodetector, and then the algorithm-processed information from the DMD was detected by BP photodetectors, followed by reconstruction calculations. This could avoid the noise created by movements of target objects or photodetectors. Capturing NIR (830 nm) laser spot images with 32 × 32 and 64 × 64 pixels only

took 500 and 2,000 measurements, respectively, which was much less than the number of total pixels. This effective infrared sensor demonstrated advantages over focal plane sensors in conventional infrared cameras, which was promising in high-speed infrared imaging.

Polarization contains certain characteristics determined by the target objects after reflection or transmission. Photodetectors based on 2D materials with anisotropy ($PdSe_2$ [63, 71], $PtTe_2$ [210], Te [128], etc.) have great potential in high-resolution infrared polarized imaging. As the key to a sensor system, photodetectors should have impressive performance. An Au/GeSe/Au photodetector exhibited a high sensitivity of ~ $10^3$ A·W$^{-1}$, broad spectral response from 400 to 1,050 nm, and fast response speed of 22.7/49.5 µs [130]. With unique polarization sensitivity in the spectral range of 690–1,050 nm and broadband polarized light absorption preferentially in the $y$-direction, the 2D α-GeSe photodetector was incorporated with an image sensor system. The contrast ratios of 2.59, 2.63 and 3.45 in the visible (675 and 700 nm) and NIR (808 nm) bands manifested high-resolution polarimetric imaging in dual bands. A graphene/$PdSe_2$/Ge photodetector exhibited highly polarization-sensitive broadband photodetection with an ultrahigh polarization sensitivity of 112.2 [72]. Regarding the infrared polarized imaging ability, Fig. 9(g) illustrates the outstanding polarization imaging ability by a set of equipment, as shown in Fig. 9(h). The image of the English letter "P" was of higher resolution at a polarization angle of 0° (left of Fig. 9(g)) compared with that at a polarization angle of 90° (right of Fig. 9(g)), and the voltage contrast ratios were $3.25 \times 10^3$ and $2.9 \times 10^2$ respectively. Tong and coworkers investigated an anisotropic Te photodetector [211]. A photoresponsivity anisotropic ratio of ~ 8 under 2.3 µm incident light was measured. A broadband sensitive photoresponse from visible to MIR was realized at room temperature, with a photoresponsivity of ~ $1.36 \times 10^3$ A·W$^{-1}$ and detectivity of ~ $1.15 \times 10^{10}$ Jones at 1.06 µm. Even under illumination with a wavelength of 3.0 µm, the photoresponsivity remained higher than ~ $3.53 \times 10^2$ A·W$^{-1}$ and the measured detectivity was higher than ~ $3.01 \times 10^9$ Jones. These remarkable performances were favorable for the application of polarized imaging. Furthermore, this photodetector was utilized to realize polarized infrared imaging for a target without any polarization filter. The scattering media between the incident infrared light and the target aimed at creating approximately linear polarized signals. Compared with traditional division-of-focus-plane devices, fewer pixels of anisotropic Te photodetectors were required to calculate the value of a given-size degree of linear polarization (DoLP) according to

$$\text{DoLP} = \frac{\sqrt{S_1^2 + S_2^2}}{S_0} \tag{10}$$

$$S_0 = I_{0°}(x,y) + I_{90°}(x,y) \tag{11}$$

$$S_1 = I_{0°}(x,y) - I_{90°}(x,y) \tag{12}$$

$$S_2 = I_{45°}(x,y) - I_{135°}(x,y) \tag{13}$$

where $I_\theta(x,y)$ refers to the polarized intensity detected at the $\theta$ angle. The advantages of Te photodetectors were offered by comparison with non-polarized $MoTe_2$ photodetectors. As Fig. 9(i) shows, Te photodetectors exhibit a much clearer contrast and fewer pixels to realize the same resolution, suggesting a promising approach to realize higher-resolution imaging.

A polarization-sensitive photodetector based on the $WSe_2$/$ReSe_2$ heterostructure realized incoherent holography 3D imaging due to its outstanding NIR (980 nm)-selective linear polarization (LP) detection [212]. A linear dynamic range wider than 100 dB and a rapid photoswitching behavior with a cut-off frequency up to 100 kHz were achieved. The components of this holography recording system are shown in Fig. 9(j). To demonstrate the 3D imaging ability, two different metal transmissive negative targets with the letter "$WSe_2$" and the letter "$ReSe_2$" are used to mimic the volumetric layer. The left image of Fig. 9(k) shows the output images of four phase-shifted holograms captured by the $WSe_2$/$ReSe_2$ photodetector in the holography recording system. After numerical reconstructions involved in the four different holograms, holographic 3D imaging of different letters clearly appeared (the middle and the right of Fig. 9(k)). A two-color infrared photodetector based on a BP/$MoS_2$/Si heterostructure (illustrated in Fig. 8(e)) designed by Wu et al. was applied to temporal-spatial coexisting two-color infrared imaging [206]. The vertical structure formed two opposite built-in electric fields to independently detect carriers generated from NIR and SWIR. Besides, the two-colour feature supported detecting the target temperature at the same time as imaging.

## 5.2 Flexible devices

In 2014, Liu et al. demonstrated the first fully flexible and transparent graphene-based infrared photodetector [213]. Polyethylene terephthalate (PET) was chosen as the substrate, and the controllable-area chemical doping of CVD-grown graphene enabled high photoresponsivity and fast response speed. A prerequisite for photodetectors applied in flexible optoelectronic products in real scenarios is the anti-bending ability. 2D-based infrared photodetectors with flexible substrates can meet the basic requirements of flexible devices such as the electronic skin or medical monitoring [214]. While bending can change the compactness of 2D materials, their good extreme-mechanical-deformation tolerance [215] helps the photodetectors to maintain high sensitivity and high performance under strengths. For example, 2D ternary $SnS_{1.26}Se_{0.76}$ alloy nanosheets exfoliated from bulk crystals were transferred onto a PET substrate [107]. The $R$ under the 808 nm illustration before and after 100 bending cycles with a bending radius of 5.5 mm (Fig. 10(a)) was 120 and 98 mA·W$^{-1}$ respectively. Moreover, as Fig. 10(b) illustrates, the response time remained the same after the bending cycles. The excellent mechanical durability, reproducibility, and high photosensitivity illustrated the promising future for wearable optoelectronic device applications. Another flexible photodetector based on a wafer-scale SnSe film exhibited ultrabroadband detection from UV to MIR, and under incident light of 10.6 µm, the device exhibited a relatively high responsivity of 0.16 A·W$^{-1}$ and a specific detectivity of $3.9 \times 10^7$ Jones [43]. Regarding the anti-bending capacity, after 200 bending cycles, only a small decrease in the photocurrent was measured.

Replacing the hard substrates with flexible polymer substrates such as polyimide (PI) [216], and filter membrane [217], some infrared photodetectors still exhibit stable detection performance. For example, the 2D HfSSe photodetector based on Si/$SiO_2$ achieved a detective performance up to a photoresponsivity of ~ 4.2 A·W$^{-1}$ and specific detectivity of ~ $3.4 \times 10^{10}$ Jones at 980 nm [106]. When the HfSSe nanoflakes were transferred onto a PET substrate, the responsivity of this flexible photodetector was approximately 1.3 A·W$^{-1}$ at a flat state and 0.4 A·W$^{-1}$ at a bending state. The decrease in responsivity was concluded to be due to the crack in the metal electrodes. Meanwhile, the other route to realize flexibility is to reduce the thickness of the materials of the original hard substrates. Choi et al. demonstrated a $MoS_2$/Si flexible photodetector (Fig. 10(c)) with a responsivity of 10.07 mA·W$^{-1}$ and a specific detectivity of $4.53 \times 10^{10}$ Jones under NIR light (850 nm) [218]. The 2D $MoS_2$ films were directly deposited onto the
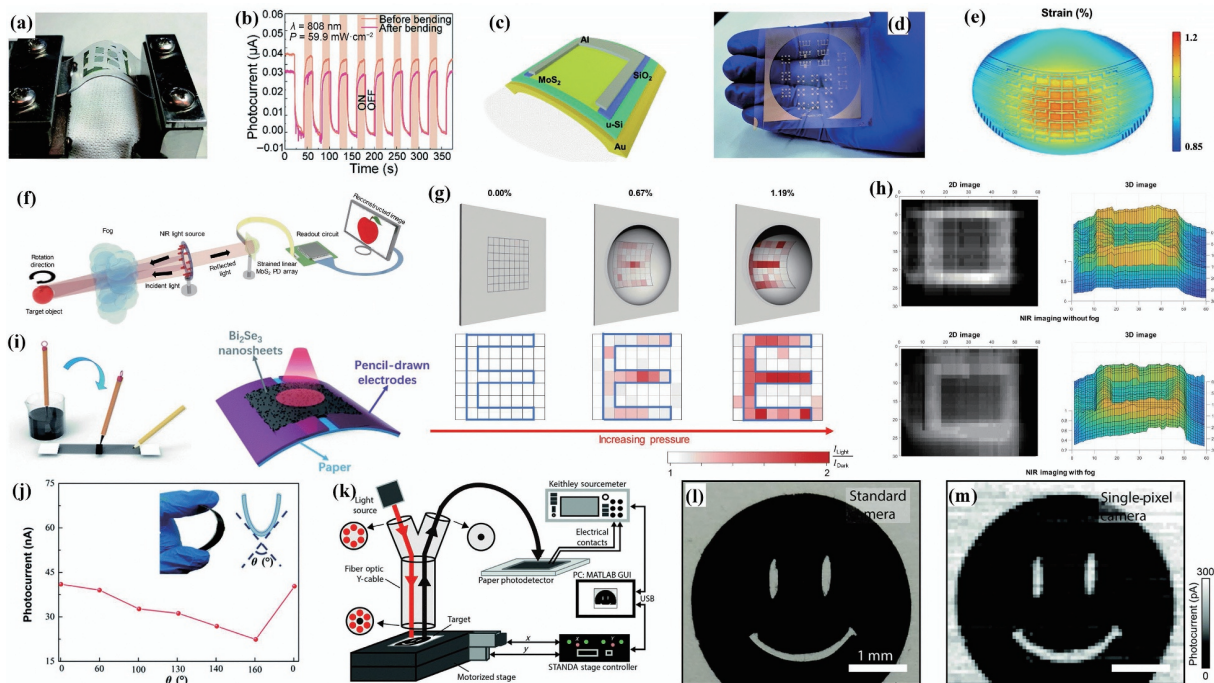
**Figure 10** (a) The instrument used for bending. (b) Time trace of the photoresponse under illumination with 808 nm laser before and after bending the device 100 times. Reproduced with permission from Ref. [107], © The Royal Society of Chemistry 2019. (c) Illustration of a flexible MoS$_2$/Si photodetector. Reproduced with permission from Ref. [218], © The Royal Society of Chemistry 2021. (d) Digital photographs of Au electrodes patterned on transparent and flexible PET substrates. Reproduced with permission from Ref. [137], © The Royal Society of Chemistry 2019. (e) Simulation of the strain distribution in a bulged PI film before MoS$_2$ degraded. The geometric deformation is enlarged 10 times by setting a scale factor of 10. The maximum strain located at the center of the PI film is 1.19%. (f) Schematic of the imaging system. (g) Photocurrent mapping images of the letter "E" recorded under incident light of 785 nm with increasing strain pressures. (h) The scanned image of the alphabet at a wavelength of 850 nm without fog and with fog. Reproduced with permission from Ref. [219], © American Chemical Society 2021. (i) Schematic diagram of the device of the fabrication procedure for direct writing using a pencil and Chinese brush on paper and the flexible device structure. Reproduced with permission from Ref. [220], © Cordeiro, N. J. A. et al. 2021. (j) Photocurrent fitting curve of the flexible photodetector under different bending angles. (k) Schematic diagram of the experimental setup. (l) Image of the object under study acquired using a standard camera. (m) Image of the same object acquired with the single-pixel camera system based on a MoS$_2$-on-paper photodetector. Reproduced with permission from Ref. [221], © The Royal Society of Chemistry 2020.

flexible Si substrate via atmospheric-pressure plasma-enhanced chemical vapour deposition. The mechanical properties of this photodetector were demonstrated by wrapping it on a finger or even a glass rod with a radius of 3 mm without mechanical cracks. The tiny change in photocurrent before and after 1,000 bending cycles suggested the good stability of this flexible photodetector.

Heterostructures-based infrared photodetectors can also be fabricated on flexible substrates [121]. Solution-synthesized 0D/2D PbS/MoS$_2$ heterostructures were drop-cast onto a PET substrate (Fig. 10(d)) [137]. This photodetector exhibited two color-band photoresponses (400–1,600 nm, visible range and NIR range), and the $R$ and $D^\star$ at 1,200 nm reached 543 mA·W$^{-1}$ and ~ 2.68 × 10$^{12}$ Jones respectively. The output current of this flexible infrared photodetector started to degrade at bending angles up to 20°, but the currents were stable under a fixed bending angle, which showed reproducibility and the repeatability of the performance of flexible devices.

For flexible photodetectors, the strain can not only decrease but also enhance the detective performance of photodetectors. One example is quoted in Figs. 7(d) and 7(e), the ReS$_2$/P(VDF-TrFE) photodetectors based on the PI substrate. Thai et al. applied strain modulations to extend the detection range of the MoS$_2$-based photodetectors array on a PI substrate up to NIR [219]. Simulations of a pneumatic bulging process from finite element analysis (the strain distribution is presented in Fig. 10(e)) showed that the flexible substrate was stretched in the biaxial direction to a highest tensile strain level of 1.19%. Then the strain-fixed MoS$_2$ photodetector array was applied in a vis–NIR line-scanning system, as shown in Fig. 10(f). As Fig. 10(g) illustrates, the image quality of the letter "E" under incident light at a wavelength of 785 nm improved with higher strain. As illustrated in Fig. 10(h), the imaging system also captured clear NIR images even under

extremely dense foggy conditions.

In addition, some interesting infrared photodetectors were fabricated on paper substrates. Liu et al. drew electrodes with graphite pencil (8B), and fabricated Bi$_2$Se$_3$-based infrared photodetectors, as illustrated in Fig. 10(i) [220]. The 2D Bi$_2$Se$_3$ was obtained via liquid exfoliation, and was transferred onto the common paper with Chinese brushes. The novel flexible photodetector exhibited a responsivity of 26.69 μA·W$^{-1}$ under infrared illumination at 1,064 nm. In addition, the photocurrents under different bending angles depicted in Fig. 10(j) suggested a good recovery from the bending strength of the device. The MoS$_2$-on-paper photodetectors fabricated by Mazaheri et al. showed spectral sensitivity from the UV to NIR range, and these photodetectors imaged objects well when they were set up on a single-pixel camera [221]. The setup was built up as shown in Fig. 10(k), and compared with the image acquired via a normal camera (Fig. 10(l)). The image quality of this photodetector is shown in Fig. 10(m).

## 5.3 On-chip integration

Some on-chip infrared photodetectors are realized by integrating the photodetectors with waveguides, which enhance the originally weak light absorption of 2D materials. 2D based photodetectors provide a more flexible and easier path to integrate with silicon photonics and CMOS processes by back-end-of-the-line steps [222]. In a silicon waveguide/Bi$_2$O$_2$Se photodetector, the interaction between Bi$_2$O$_2$Se and the light transmitted along the waveguide was driven by evanescent field coupling [26]. The Bi$_2$O$_2$Se/Si hybrid waveguide in the O-band (1,260–1,360 nm) exhibited a responsivity of 3.5 A·W$^{-1}$ at 1,260 nm and an external bias of 2 V, a dark current of 72.9 nA, and rise/decay time of

22/78 ns. Moreover, the light absorption of the device was further increased by integration with microring resonator cavities. A threefold improvement in the photocurrent at the resonance wavelength compared with that at the off-resonance wavelength was observed, implying suitability for devices with a small volume of photosensitive materials. Liu et al realized MIR on-chip photodetection through a BP avalanche photodetector based on a silicon hybrid plasmonic waveguide (HPWG) with double nanoslots, as illustrated in Figs. 11(a) and 11(b) [223]. Owing to the great enhancement of the local field induced by the nanoslots, the light absorption of BP was greatly enhanced, and the carrier transit time was reduced simultaneously. One of the further applications of waveguide-integrated infrared photodetectors is gas sensors. The PtSe$_2$/silicon waveguide photodetector with a 3D topographic channel exhibited high sensitivity to ammonia gas at room temperature [56]. The response speed of this ammonia sensor without an accelerating process (UV illumination or heating) was faster (5 min under an NH$_3$ concentration of 8 ppm) than that of the other toxic gas sensors based on the charge transfer working mechanism, which might result from the large active areas induced by 3D topography. Since the signal must be at least three times of the root-mean-square noise of the measured device, the limit of detection (LOD) was extracted by simple signal processing based on the signal-to-noise ratio (SNR). Figure 11(c) pointed to a theoretical LOD of 370 ppb.

A method utilizing the slow light effect in photonic crystal waveguides (PhCWGs) was experimentally demonstrated in a BP/PhCWG photodetector to maintain high responsivity in miniaturized BP waveguide photodetectors [81]. A shared-BP photonic system (Figs. 11(d) and 11(e)) was applied for the fair and precise characterization of the slow light enhancement. This effect spatially compressed the optical field so that the light absorption was enhanced due to the stronger interaction with the BP atomic layer. Close to the band edge approximately 3.8 μm, compared with the counterpart on a subwavelength grating waveguide, the responsivity is enhanced by more than ten times in the BP photodetector on a PhCWG with a geometric length of 10 μm. At a 0.5 V bias, the BP PhCWG photodetector realized a responsivity of 11.31 A·W$^{-1}$ and a 0.012 nW·Hz$^{-1/2}$ NEP. In addition to the silicon waveguides, chalcogenide glass waveguides have great potential for on-chip integration due to their broadband transparency covering almost the whole MIR range,

continuously tunable refractive indices, and other optical properties [224].

Photodetectors can function as the collecting terminals of on-chip sensing. One of the important parameters to analyze the light–matter interaction is the spectrum. To quantitatively analyze the spectrum to decode the involved information such as gas concentration, spectrometers are necessary. A on-chip MIR spectrometer was fabricated by utilizing a single tunable BP photodetector with an active area footprint of only 9 μm × 16 μm [225]. Due to the Stark effect of the BP photodetector, the response range of this spectrometer was tunable at 2–9 μm. The spectrum was reconstructed via the algorithm-built responsivity matrix. The BP spectrometer can clearly capture the characteristic absorption peak of CO$_2$ at approximately 4.3 μm. With a reduced scanning range (4–7 μm) and 81 photocurrent sampling points, a full-width at half-maximum of 90 nm was achieved.

Nevertheless, photodetectors based on 2D heterostructures still face some challenges, such as the transfer process which is not fully compatible with the standard CMOS compatible back-end process. Moreover, it is also important to incorporate the direct growth of wafer-scale 2D materials on substrates with the CMOS process [226]. For example, large-area direct growth on sapphire [227] or silicon [228] has been reported.

### 5.4 Other application scenarios

The possible application scenarios for 2D-based infrared photodetectors are still expanding. Different from the conventional setup that connects the in-fiber signals with external planar photodetectors based on bulk semiconductors, fiber-integrated photodetectors can implement detections or sensing in narrow spaces, having a promising future in medical endoscopic imaging. The fiber integration took advantage of concentrating the total input power into the photodetector without other optical devices, and the development of 2D materials may simplify the fabrication process. Xiong et al. integrated a 2D graphene/MoS$_2$/WS$_2$ photodetector (Figs. 12(a) and 12(b)) on the endface of a fiber [17]. The 2D materials were transferred layer-by-layer as shown in Fig. 12(c). The type-II band alignment between the MoS$_2$/WS$_2$ heterostructure broadened the response range up to SWIR, with a photoresponsivity of 17.1 A·W$^{-1}$ at 1,550 nm. Yang et al. also assembled a graphene/PdSe$_2$ photodetector on the endface of a fiber, which realized a temporal response of 660 μs at
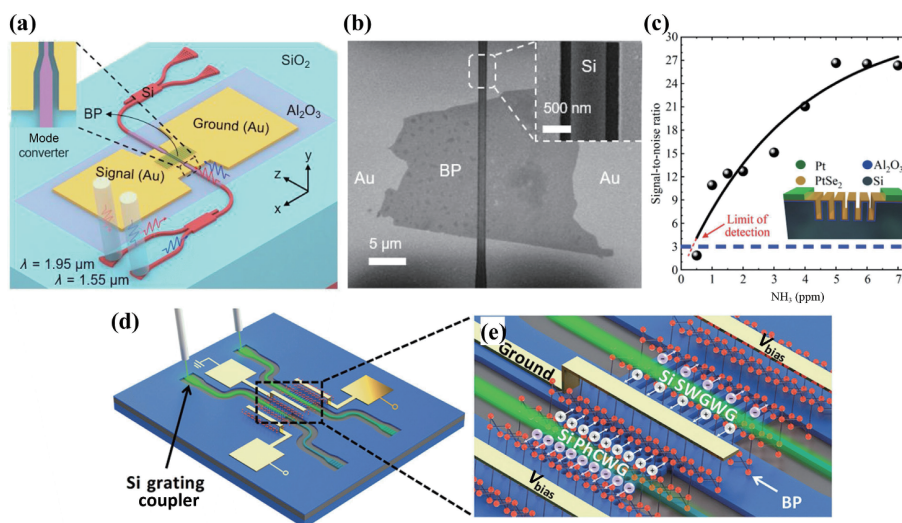


**Figure 11** (a) Schematic and (b) scanning electron microscopy (SEM) images of the silicon-BP HPWG photodetector. Reproduced with permission from Ref. [223], © American Chemical Society 2022. (c) SNR of sensor at various NH$_3$ concentrations (dots). The fitted curve (black line) reveals an LOD of 370 ppb for NH$_3$. Inset: schematic of the cross-section of the PtSe$_2$ gas sensor. Reproduced with permission from Ref. [56], © Prechtl, M. et al. 2021. (d) Schematic illustration of the shared-BP photonic system. (e) Magnified view of the black square box in (d) showing the two BP photodetectors on the PhCWG and the subwavelength grating waveguide. Reproduced with permission from Ref. [81], © WILEY-VCH Verlag GmbH & Co. KGaA, Weinheim 2020.
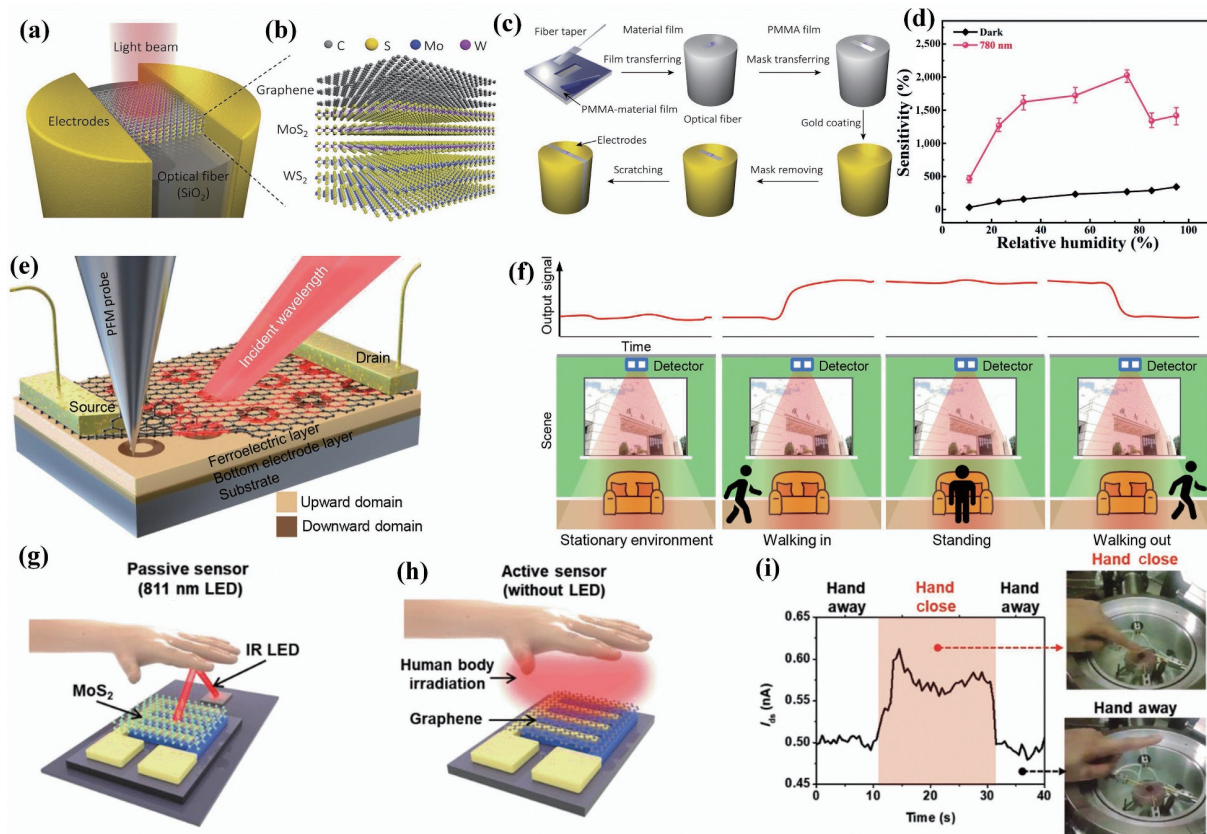
**Figure 12** (a) Schematic of the in-fiber photodetector. (b) Structure of the graphene/MoS$_2$/WS$_2$ heterojunction. (c) Sequential fabrication process of the in-fiber photodetector. Reproduced with permission from Ref. [17], © WILEY-VCH Verlag GmbH & Co. KGaA, Weinheim 2018. (d) The dependence relationship between sensitivity and relative humidity in the dark and under 780 nm illumination. Reproduced with permission from Ref. [68], © The Royal Society of Chemistry 2020. (e) Schematic of the graphene plasmonic photodetector. (f) Detection of both stationary and motion states of humans in a single device. The detection of stationary (such as environment, standing state) and motional (such as walking in/out state) scenes operates using single- and dual-band, respectively. Reproduced with permission from Ref. [230], © Elsevier Ltd. 2021. (g) MoS$_2$/NiO/Ni passive sensor. (h) The graphene/NiO/Ni active sensor. (i) The time-dependent photoresponse of the graphene active sensor (left panel) depends on the hand effect. "Hand close" (right upper panel) and "hand away" (right lower panel) represent the distance between the hand and active sensor device. Reproduced with permission from Ref. [231], © Wiley-VCH GmbH 2021.

1,520 nm [229]. However, the immature micromachining technology limits the mass production for 2D-based all-in-fiber photodetectors.

For environmental monitoring, Wu et al. transferred 2D PdSe$_2$ onto silicon nanowire arrays (SiNWAs) to construct a heterostructure photodetector with a strong light confinement effect, which resulted in its outstanding detection performance and decent imaging ability under NIR and MIR illumination [68]. Moreover, this photodetector exhibited high sensitivity to the relative humidity (RH) of the surroundings. The sensitivity ($S$) of this PdSe$_2$/SiNWA humidity sensor was defined according to

$$S = \frac{I_{RH} - I_{Dry}}{I_{Dry}} \times 100\% \tag{14}$$

where $I_{RH}$ and $I_{Dry}$ are the currents of the sensor in a humid atmosphere and under dry air conditions respectively. With illumination, the sensitivities under different RHs were greatly enhanced (Fig. 12(d)). In addition, under NIR illumination, the response and recovery time of 18.7/54.8 s in dark at 75% RH was greatly improved to 6.6/5.0 s. The high surface-to-volume ratio of this vdWH structure provided many absorption sites for OH$^-$ groups, which increased the conductivity of the device. Under illumination, the photogenerated holes would oxide the OH$^-$ groups and the conductivity was enhanced by free electrons. With increasing of RH, more free electrons and larger photocurrent were created. The extreme RH provided H$^+$ groups which would consume the photogenerated electrons to reduce the photocurrent. A graphene plasmonic photodetector (Fig. 12(e)) was demonstrated to realize ferroelectric-tuned dual-band infrared

detection, and was applied to thermal imaging and warning systems [230]. The excitement and confinement of the intrinsic graphene plasmons resulted from the periodic ferroelectric polarization array with nanoscale ring shapes. As Fig. 12(f) shows, Guo et al. tested the effects of detecting motion states of human movements by using this photodetector with tunable resonance photoresponses of 3.7–16.3 and 15.1–52.1 μm. The difference in output signals corresponded with the change in motion states. Kim et al. proposed two types of integrated infrared proximity sensor applications, namely, a passive sensor with the MoS$_2$/NiO/Ni structure for the NIR range and a graphene/NiO/Ni active sensor for the MIR range [231]. The passive sensor exhibited a broad photoresponse to reflect a NIR light-emitting diode (LED) (Fig. 12(g)), while the active sensor absorbed human body irradiation in a range from 2 to 16 μm (Fig. 12(h)). High detectivities of 10$^{11}$ Jones even up to a long wavelength of 10 μm for the active sensor and ~ 10$^{12}$ Jones at 1 μm for the passive sensor were achieved. Taking the active sensor as an example, as Fig. 12(i) shows, a low dark current of 0.5 nA was observed in the room-temperature hand away case. Conversely, in the hand close case, the active sensor absorbed the human body irradiation energy, which generated photoexcited carriers, resulting in an increase in the photoresponse current to 0.62 nA.

# 6   Conclusion and outlooks

In this article, current progress on 2D materials beyond TMDs and graphene as well as structure constructions are summarized, and their performances are also summarized in Table 2 . These

**Table 2** Summary of the performance of 2D-based infrared photodetectors

| Material | Response range (μm) | R (A·W⁻¹) | D* (Jones) | $\tau_r/\tau_d$ (μs) | EQE (%) | Ref. |
|---|---|---|---|---|---|---|
| PtSe$_2$ | 0.632–10 | ~ 4.5 (10 μm) | $7 \times 10^8$ (10 μm) | $1.1 \times 10^3/1.2 \times 10^3$ | — | [52] |
| PdSe$_2$ | Vis–4.05 | 708 (1,640 nm) | $1.31 \times 10^9$ (1,640 nm) | $220 \times 10^3$ | — | [69] |
| PdSe$_2$/MoS$_2$ | 0.45–10.6 | 42.1 (10.6 μm) | $6.09 \times 10^{10}$ (4.012 μm) | $7.45 \times 10^4/9.31 \times 10^4$ | 25.4 | [61] |
| PdSe$_2$/SiNWA | 0.2–4.6 | 0.726 (980 nm) | $3.19 \times 10^{14}$ (980 nm) | 25.1/34 | — | [68] |
| BP | Vis–3.39 | 82 (3.39 μm) | $1.25 \times 10^{11}$ | — | — | [74] |
| Graphene/BP | 0.637–4.25 | $51.5 \times 10^{-3}$ (1,310 nm) | $6.69 \times 10^8$ (4.25 μm) | 12.6/13.2 | 10.1 (1,310 nm) | [87] |
| b-AsP | 0.45–2.2 | 0.45 (1,550 nm) | $6.45 \times 10^9$ (1,550 nm) | $4 \times 10^4/1.4 \times 10^5$ | — | [92] |
| hBN/BP/hBN | Vis–MIR | 0.518 (3.4 μm) | $3.3 \times 10^{13}$ (3.4 μm) | — | — | [94] |
| hBN/b-AsP/hBN | Vis–MIR | 0.19 (3.4 μm) | $3.57 \times 10^{10}$ (3.4 μm) | — | — | [95] |
| Bi$_2$O$_2$S | Vis–NIR | 4 (785 nm) | $1.3 \times 10^{10}$ (785 nm) | $1 \times 10^5$ | 630 (785 nm) | [102] |
| Bi$_2$O$_2$Te | 0.21–2.4 | $2 \times 10^4$ | $2 \times 10^{14}$ | ~ $1 \times 10^5$/~ $1.22 \times 10^5$ | 6,000 (210 nm) | [104] |
| HfSSe | UV–NIR | 1.3 (980 nm) | $10^{14}$ (980 nm) | $3 \times 10^4$ | — | [106] |
| Bi$_2$Te$_2$Se | 0.365–0.98 | 2.74 (980 nm) | — | 2 | — | [110] |
| InSiTe$_3$ | 0.265–1.31 | $7.1 \times 10^{-2}$ (365 nm) | $7.59 \times 10^9$ (365 nm) | 0.576 | — | [111] |
| CrPS$_4$/MoS$_2$ | 0.532–1.450 | $7.69 \times 10^{-3}$ (1,095 nm) | $1.35 \times 10^9$ (1,095 nm) | $5 \times 10^5$ | — | [113] |
| Ti$_3$C$_2$T$_x$/p-Si | SWIR | $5.5 \times 10^{-4}$ | — | — | — | [123] |
| Te | 0.5–2 | 6650 (1,550 nm) 5.19 (blackbody radiation) | $1.23 \times 10^{12}$ (1,550 nm) $9.6 \times 10^8$ (blackbody radiation) | 31.7/25.5 | — | [128] |
| Te (with optical cavity) | –3.4 | 13 (1.4 μm) | $2 \times 10^9$ (1.7 μm) | — | — | [127] |
| BP/PdSe$_2$ | 0.532–1.31 | $1.63 \times 10^5$ (1,310 nm) | $1.13 \times 10^{13}$ (532 nm) | $1.6 \times 10^3$/$4.7 \times 10^3$ | $9.4 \times 10^6$ | [62] |
| WS$_2$/HfS$_2$ | –20 | $8.2 \times 10^2$ (4.7 μm) | ~ $10^{12}$ (7 μm) | ~ $1 \times 10^{-6}$ | — | [147] |
| 0D-MOF/2D-Bi$_2$Se$_3$ | 0.5–2 | 4,725 (1,500 nm) | $3.5 \times 10^{13}$ (1,500 nm) | $1.3 \times 10^5$/$6 \times 10^3$ | 4,185 (1,500 nm) | [157] |
| MoS$_2$/CuInSe$_2$ QD | 0.355–1.064 | 74.8 (1,064 nm) | $7.1 \times 10^{11}$ (1,064 nm) | $1.5 \times 10^6$/$1.2 \times 10^6$ | — | [158] |
| Metallic Mo$_2$C/MoS$_2$ | 0.405–1.31 | $5 \times 10^3$ | $3 \times 10^2$ | — | — | [163] |
| Au NPs/MoS$_2$ | 0.7–1.6 | $6.4 \times 10^{-2}$ (980 nm) | — | $2.4 \times 10^3$/$2.6 \times 10^3$ | — | [166]. |
| WSe$_2$/α-In$_2$Se$_3$ | 0.4–1.1 | 2.21 (980 nm) | $9.52 \times 10^{10}$ (980 nm) | $3.3 \times 10^3$/$5.7 \times 10^3$ | — | [191] |
| Graphene/MoTe$_2$/P(VDF-TrFE) | Vis–1.4 | 0.5 (1,310 nm) | $3 \times 10^{11}$ (1,310 nm) | 30 | 40 | [197] |

layered materials present attractive properties that favor high-performance infrared photodetection, and exhibit surprising applications in imaging, environmental monitoring, on-chip integration, and flexible devices. Nevertheless, their limitations need further research to make breakthroughs. The emerging NTMDs display a stronger interlayer coupling than TMDs, long-duration air stability and layer-dependent narrow bandgap, which can even realize a transition from semimetal to semiconductor, resulting in their bright future for broadband infrared photodetection. Among them, PdSe$_2$ with high carrier mobility exhibited an outstanding responsivity and EQE of 708 A·W⁻¹ and 82,700%, respectively, under NIR illumination [69], and the in-plane anisotropic structure can support polarization detection. In the field of polarization imaging, especially for the detection of LWIR radiation, BP and arsenic b-AsP have a more mature investigation system for device integration, with performance comparable to that of commercialized HgCdTe photodetectors. However, despite of the existing effective protective methods, instability of the surface in ambient conditions caused by chemical degradation persists as the biggest impediment to its further applications. Infrared photodetectors based on ternary materials such as Bi$_2$O$_2$X take advantage of their fast response speed, while the hindrances for the 2D ternary compounds lie in the difficult and costly precise growth of the corresponding crystal and film, which is similar to commercial ternary bulk photodiodes.

For those structure designs, type-II band alignments speed up the charge separation process and induce electrons and holes to move in the opposite direction, enabling spatial separation and the best utilization of photogenerated carriers. The other striking characteristic of the staggered band structure is the interlayer transition subbandgap realizing a photoresponse at longer wavelengths, which suggests that 2D materials with considerable electric properties but an absorption cut-off wavelength in the visible region can also be employed in infrared detection. For infrared photodetectors based on PGE, the carrier lifetime is extended due to sensitizer trapping, resulting in enhancement of photoconductive gain and photoresponsivity. However, a longer lifetime also means longer relaxation time, which causes a low response speed for PGE devices. To find the middle ground, photoresponsivity should be augmented by larger optical absorption without conspicuous lifetime extension, for example, the introduction of ferroelectrics or surface plasmons. Under a durable ferroelectric field, an additional large gate bias, which is applied in type-II band alignments and may cause a large dark current and energy consumption, becomes unnecessary. The realization of LSPR through diverse metal gratings, semiconductor nanostructures or graphene enhances light–matter interactions, demonstrating high overall performance. In addition, the advantages and maturity of metal plasmonic structures have been demonstrated in other silicon-integrated devices.

The advantages that have been discussed indeed imply a great potential for 2D materials to play a critical role in the next

generation of infrared photodetectors. The limitations that we mentioned impede the way for more 2D-based infrared photodetectors from laboratories to factories. At the present stage, from our perspective, to promote the revolution, there are still some problems to be solved, or it will be quite difficult to predict the prosperous future of 2D materials in the mature photodetector market.

(1) Demands for large-size and low-cost 2D materials

The growth of large-scale 2D materials to fabricate arrays is one of the ultimate goals to realize wide detector applications at an industrial level [21]. Success in wafer-scale growth or direct growth on silicon for 2D materials can promote development in real applications. Many reported 2D-based photodetectors with high responsivity have been fabricated via mechanical exfoliation, which is not conducive to repetitive mass production. High-performance devices should not only be stable but also relatively costless and able to be synthesized controllably. In the manufacturing process, further exploration of CVD, CVT or molecular beam epitaxy may bring a successful rise to match the current demands, while how to decrease the cost is still unclear.

(2) More practical performance

For infrared photodetectors based on most categories of 2D materials, the response speed is relatively low compared to that of commercialized photodetectors [232]. For ultrafast layered ternary compounds, crystal growth is a more intractable issue. Research on the combination of 2D materials and HgCdTe has been proposed to make a trade-off [233]. In addition, compared to the radiation from the laser, weaker blackbody radiation is closer to the signals emitted by real objects, yet many studies on 2D infrared photodetectors did not present blackbody sensitivity or demonstrate the performances in possible applications, making them difficult to commercialize or optimize.

(3) Interface contact optimization

The contact electrodes also play important roles in the photodetector performance [62, 66, 234]. However, few published works discuss the interface contacts of electrodes/2D materials and vdW heterostructures. The SBH and energy band bending have a crucial influence on the transfer process of carriers. In those rational structure designs, the interface contact should also be taken into consideration to improve the device performance. To find the proper way to address this issue, theoretical calculations may be helpful with less trial-and-error cost.

(4) Transfer process optimization

In the wet transfer process of large-area CVD-growth 2D materials from the metal substrate to the target substrate, it is difficult to put down the samples at the precise position. In addition, water or polymer residues are inevitable, which can damage the ideal clean interface. Thus, novel dry transfer of CVD samples has been developed as a simplified and competitive process [235]. Additionally, more efforts are still called for handling doping nonuniformities and batch-to-batch variability [9] induced by the transfer process. Moreover, a transfer process that is compatible with the CMOS process can scale up the applications in on-chip devices (sensing or communication) for 2D-based infrared photodetectors is another direction of optimization.

To conclude, the future of 2D infrared photodetectors is promising in the booming developments, while turning that into reality requires more effort.

## Acknowledgements

## References

[1] Herschel, W. XIV. Experiments on the refrangibility of the invisible rays of the sun. *Philos. Trans.* **1800**, *90*, 284–292.

[2] Zhuge, F. W.; Zheng, Z.; Luo, P.; Lv, L.; Huang, Y.; Li, H. Q.; Zhai, T. Y. Nanostructured materials and architectures for advanced infrared photodetection. *Adv. Mater. Technol.* **2017**, *2*, 1700005.

[3] Liu, J. K.; Xiao, L.; Liu, Y.; Cao, L. F.; Shen, Z. K. Development of long-wavelength infrared detector and its space-based application requirements. *Chin. Phys. B* **2019**, *28*, 028504.

[4] Lawson, W. D.; Nielsen, S.; Putley, E. H.; Young, A. S. Preparation and properties of HgTe and mixed crystals of HgTe-CdTe. *J. Phys. Chem. Solids* **1959**, *9*, 325–329.

[5] Ye, Z. H.; Li, H. H.; Wang, J. D.; Chen, X.; Sun, C. H.; Liao, Q. J.; Huang, A. B.; Li, H.; Zhou, S. M.; Lin, J. M. et al. Recent hotspots and innovative trends of infrared photon detectors. *J. Infrared Millim. Waves* **2022**, *41*, 15–39.

[6] Tan, B.; Cheng, S. F.; Liu, B.; Zhou, W. H.; Liu, Y. F.; Zhang, C. J.; Cao, S. S.; Ding, Y. Y.; Yang, Z. C.; Huang, L. Effective suppression of surface leakage currents in T2SL photodetectors with deep and vertical mesa sidewalls via TMA and $H_2$ plasma combined pretreatment. *Infrared Phys. Technol.* **2021**, *116*, 103724.

[7] Wang, J.; Chen, X. S.; Hu, W. D.; Wang, L.; Lu, W.; Xu, F. Q.; Zhao, J.; Shi, Y. L.; Ji, R. B. Amorphous HgCdTe infrared photoconductive detector with high detectivity above 200 K. *Appl. Phys. Lett.* **2011**, *99*, 113508.

[8] Tong, J. C.; Tobing, L. Y. M.; Luo, Y.; Zhang, D. W.; Zhang, D. H. Single plasmonic structure enhanced dual-band room temperature infrared photodetection. *Sci. Rep.* **2018**, *8*, 1548.

[9] Konstantatos, G. Current status and technological prospect of photodetectors based on two-dimensional materials. *Nat. Commun.* **2018**, *9*, 5266.

[10] Wang, H. Y.; Li, Z. X.; Li, D. Y.; Chen, P.; Pi, L. J.; Zhou, X.; Zhai, T. Y. Van der Waals integration based on two-dimensional materials for high-performance infrared photodetectors. *Adv. Funct. Mater.* **2021**, *31*, 2103106.

[11] Tan, C. L.; Mohseni, H. Emerging technologies for high performance infrared detectors. *Nanophotonics* **2018**, *7*, 169–197.

[12] Izhnin, I. I.; Mynbaev, K. D.; Voitsekhovsky, A. V.; Korotaev, A. G.; Syvorotka, I. I.; Fitsych, O. I.; Varavin, V. S.; Dvoretsky, S. A.; Mikhailov, N. N.; Remesnik, V. G. et al. Arsenic-ion implantation-induced defects in HgCdTe films studied with Hall-effect measurements and mobility spectrum analysis. *Infrared Phys. Technnol.* **2019**, *98*, 230–235.

[13] Rogalski, A.; Martyniuk, P.; Kopytko, M.; Madejczyk, P.; Krishna, S. InAsSb-based infrared photodetectors: Thirty years later on. *Sensors* **2020**, *20*, 7047.

[14] Rogalski, A.; Martyniuk, P.; Kopytko, M.; Hu, W. D. Trends in performance limits of the HOT infrared photodetectors. *Appl. Sci.* **2021**, *11*, 501.

[15] Chang, C.; Chen, W.; Chen, Y.; Chen, Y. H.; Chen, Y.; Ding, F.; Fan, C. H.; Fan, H. J.; Fan, Z. X.; Gong, C. et al. Recent progress on two-dimensional materials. *Acta Phys. -Chim. Sin.* **2021**, *37*, 2108017.

[16] Hu, X.; Wu, J. H.; Wu, M. Z.; Hu, J. Q. Recent developments of infrared photodetectors with low-dimensional inorganic nanostructures. *Nano Res.* **2022**, *15*, 805–817.

[17] Xiong, Y. F.; Chen, J. H.; Lu, Y. Q.; Xu, F. Broadband optical-fiber-compatible photodetector based on a graphene-MoS$_2$-WS$_2$ heterostructure with a synergetic photogenerating mechanism. *Adv. Electron. Mater.* **2019**, *5*, 1800562.

[18] Bonaccorso, F.; Sun, Z.; Hasan, T.; Ferrari, A. C. Graphene photonics and optoelectronics. *Nat. Photonics* **2010**, *4*, 611–622.

[19] Chen, J. H.; Jang, C.; Xiao, S. D.; Ishigami, M.; Fuhrer, M. S. Intrinsic and extrinsic performance limits of graphene devices on SiO$_2$. *Nat. Nanotechnol.* **2008**, *3*, 206–209.

[20] Yu, X. C.; Li, Y. Y.; Hu, X. N.; Zhang, D. L.; Tao, Y.; Liu, Z. X.; He, Y. M.; Haque, A.; Liu, Z.; Wu, T. et al. Narrow bandgap oxide nanoparticles coupled with graphene for high performance mid-infrared photodetection. *Nat. Commun.* **2018**, *9*, 4299.

[21] Rogalski, A.; Kopytko, M.; Martyniuk, P. Two-dimensional infrared and terahertz detectors: Outlook and status. *Appl. Phys. Rev.* **2019**, *6*, 021316.

[22] Radisavljevic, B.; Radenovic, A.; Brivio, J.; Giacometti, V.; Kis, A. Single-layer MoS₂ transistors. *Nat. Nanotechnol.* **2011**, *6*, 147–150.

[23] Han, R. Y.; Feng, S.; Sun, D. M.; Cheng, H. M. Properties and photodetector applications of two-dimensional black arsenic phosphorus and black phosphorus. *Sci. China Inf. Sci.* **2021**, *64*, 140402.

[24] Wang, Y. H.; Pang, J. B.; Cheng, Q. L.; Han, L.; Li, Y. F.; Meng, X.; Ibarlucea, B.; Zhao, H. B.; Yang, F.; Liu, H. Y. et al. Applications of 2D-layered palladium diselenide and its van der Waals heterostructures in electronics and optoelectronics. *Nano-Micro Lett.* **2021**, *13*, 143.

[25] Tamalampudi, S. R.; Dushaq, G.; Villegas, J. E.; Rajput, N. S.; Paredes, B.; Elamurugu, E.; Rasras, M. S. Short-wavelength infrared (SWIR) photodetector based on multi-layer 2D GaGeTe. *Opt. Express* **2021**, *29*, 39395–39405.

[26] Wu, J. H.; Wei, M. L.; Mu, J. L.; Ma, H.; Zhong, C. Y.; Ye, Y. T.; Sun, C. L.; Tang, B.; Wang, L. C.; Li, J. Y. et al. High-performance waveguide-integrated Bi₂O₂Se photodetector for Si photonic integrated circuits. *ACS Nano* **2021**, *15*, 15982–15991.

[27] Wang, J.; Han, J.; Chen, X.; Wang, X. Design strategies for two-dimensional material photodetectors to enhance device performance. *InfoMat* **2019**, *1*, 33–53.

[28] Zhou, H. B.; Lai, H. J.; Sun, X.; Zhang, N.; Wang, Y. E.; Liu, P. Y.; Zhou, Y.; Xie, W. G. Van der Waals MoS₂/two-dimensional perovskite heterostructure for sensitive and ultrafast sub-band-gap photodetection. *ACS Appl. Mater. Interfaces* **2022**, *14*, 3356–3362.

[29] Venuthurumilli, P. K.; Ye, P. D.; Xu, X. F. Plasmonic resonance enhanced polarization-sensitive photodetection by black phosphorus in near infrared. *ACS Nano* **2018**, *12*, 4861–4867.

[30] Lv, L.; Zhuge, F. W.; Xie, F. J.; Xiong, X. J.; Zhang, Q. F.; Zhang, N.; Huang, Y.; Zhai, T. Y. Reconfigurable two-dimensional optoelectronic devices enabled by local ferroelectric polarization. *Nat. Commun.* **2019**, *10*, 3331.

[31] Sun, Z. H.; Chang, H. X. Graphene and graphene-like two-dimensional materials in photodetection: Mechanisms and methodology. *ACS Nano* **2014**, *8*, 4133–4156.

[32] Wang, F. K.; Zhang, Y.; Gao, Y.; Luo, P.; Su, J. W.; Han, W.; Liu, K. L.; Li, H. Q.; Zhai, T. Y. 2D metal chalcogenides for IR photodetection. *Small* **2019**, *15*, 1901347.

[33] Li, P.; Yuan, K.; Lin, D. Y.; Wang, T. T.; Du, W. Y.; Wei, Z. M.; Watanabe, K.; Taniguchi, T.; Ye, Y.; Dai, L. p-MoS₂/n-InSe van der Waals heterojunctions and their applications in all-2D optoelectronic devices. *RSC Adv.* **2019**, *9*, 35039–35044.

[34] Lin, P.; Yang, J. K. Tunable WSe₂/WS₂ van der Waals heterojunction for self-powered photodetector and photovoltaics. *J. Alloys Compd.* **2020**, *842*, 155890.

[35] Rao, G. F.; Wang, X. P.; Wang, Y.; Wangyang, P. H.; Yan, C. Y.; Chu, J. W.; Xue, L. X.; Gong, C. H.; Huang, J. W.; Xiong, J. et al. Two-dimensional heterostructure promoted infrared photodetection devices. *InfoMat* **2019**, *1*, 272–288.

[36] Miao, J. S.; Wang, C. Avalanche photodetectors based on two-dimensional layered materials. *Nano Res.* **2021**, *14*, 1878–1888.

[37] Gao, A. Y.; Lai, J. W.; Wang, Y. J.; Zhu, Z.; Zeng, J. W.; Yu, G. L.; Wang, N. Z.; Chen, W. C.; Cao, T. J.; Hu, W. D. et al. Observation of ballistic avalanche phenomena in nanoscale vertical InSe/BP heterostructures. *Nat. Nanotechnol.* **2019**, *14*, 217–222.

[38] Noumbé, U. N.; Gréboval, C.; Livache, C.; Chu, A.; Majjad, H.; López, L. E. P.; Mouafo, L. D. N.; Doudin, B.; Berciaud, S.; Chaste, J. et al. Reconfigurable 2D/0D p-n Graphene/HgTe nanocrystal heterostructure for infrared detection. *ACS Nano* **2020**, *14*, 4567–4576.

[39] Zolotavin, P.; Evans, C.; Natelson, D. Photothermoelectric effects and large photovoltages in plasmonic Au nanowires with nanogaps. *J. Phys. Chem. Lett.* **2017**, *8*, 1739–1744.

[40] Liu, H.; Liu, Y. J.; Dong, S. C.; Xu, H. Y.; Wu, Y. P.; Hao, L. Z.; Cao, B. L.; Li, M. J.; Wang, Z. G.; Han, Z. D. et al. Photothermoelectric SnTe photodetector with broad spectral response and high on/off ratio. *ACS Appl. Mater. Interfaces* **2020**, *12*, 49830–49839.

[41] Guo, W. L.; Dong, Z.; Xu, Y. J.; Liu, C. L.; Wei, D. C.; Zhang, L. B.; Shi, X. Y.; Guo, C.; Xu, H.; Chen, G. et al. Sensitive terahertz detection and imaging driven by the photothermoelectric effect in ultrashort-channel black phosphorus devices. *Adv. Sci.* **2020**, *7*, 1902699.

[42] Dai, M. J.; Wang, C. W.; Ye, M.; Zhu, S.; Han, S.; Sun, F. Y.; Chen, W. D.; Jin, Y. H.; Chua, Y.; Wang, Q. J. High-performance, polarization-sensitive, long-wave infrared photodetection via photothermoelectric effect with asymmetric van der waals contacts. *ACS Nano* **2022**, *16*, 295–305.

[43] Xu, H. Y.; Hao, L. Z.; Liu, H.; Dong, S. C.; Wu, Y. P.; Liu, Y. J.; Cao, B. L.; Wang, Z. G.; Ling, C. C.; Li, S. X. et al. Flexible SnSe photodetectors with ultrabroad spectral response up to 10.6 μm enabled by photobolometric effect. *ACS Appl. Mater. Interfaces* **2020**, *12*, 35250–35258.

[44] Tong, L.; Peng, M.; Wu, P. S.; Huang, X. Y.; Li, Z.; Peng, Z. R.; Lin, R. F.; Sun, Q. D.; Shen, Y. X.; Zhu, X. F. et al. Hole-dominated Fowler-Nordheim tunneling in 2D heterojunctions for infrared imaging. *Sci. Bull.* **2021**, *66*, 139–146.

[45] Liu, C. Y.; Guo, J. S.; Yu, L. W.; Li, J.; Zhang, M.; Li, H.; Shi, Y. C.; Dai, D. X. Silicon/2D-material photodetectors: From near-infrared to mid-infrared. *Light: Sci. Appl.* **2021**, *10*, 123.

[46] Wu, J. Y.; Chun, Y. T.; Li, S. P.; Zhang, T.; Wang, J. Z.; Shrestha, P. K.; Chu, D. P. Broadband MoS₂ field-effect phototransistors: Ultrasensitive visible-light photoresponse and negative infrared photoresponse. *Adv. Mater.* **2018**, *30*, 1705880.

[47] Jiang, W.; Zheng, T.; Wu, B. M.; Jiao, H. X.; Wang, X. D.; Chen, Y.; Zhang, X. Y.; Peng, M.; Wang, H. L.; Lin, T. et al. A versatile photodetector assisted by photovoltaic and bolometric effects. *Light: Sci. Appl.* **2020**, *9*, 160.

[48] Pi, L. J.; Li, L.; Liu, K. L.; Zhang, Q. F.; Li, H. Q.; Zhai, T. Y. Recent progress on 2D noble-transition-metal dichalcogenides. *Adv. Funct. Mater.* **2019**, *29*, 1904932.

[49] Wang, Y. W.; Zhou, L.; Zhong, M. Z.; Liu, Y. P.; Xiao, S.; He, J. Two-dimensional noble transition-metal dichalcogenides for nanophotonics and optoelectronics: Status and prospects. *Nano Res.* **2022**, *15*, 3675–3694.

[50] Wang, Z.; Wang, P.; Wang, F.; Ye, J. F.; He, T.; Wu, F.; Peng, M.; Wu, P. S.; Chen, Y. F.; Zhong, F. et al. A noble metal dichalcogenide for high-performance field-effect transistors and broadband photodetectors. *Adv. Funct. Mater.* **2020**, *30*, 1907945.

[51] Zhao, Y. D.; Qiao, J. S.; Yu, P.; Hu, Z. X.; Lin, Z. Y.; Lau, S. P.; Liu, Z.; Ji, W.; Chai, Y. Extraordinarily strong interlayer interaction in 2D layered PtS₂. *Adv. Mater.* **2016**, *28*, 2399–2407.

[52] Yu, X. C.; Yu, P.; Wu, D.; Singh, B.; Zeng, Q. S.; Lin, H.; Zhou, W.; Lin, J. H.; Suenaga, K.; Liu, Z. et al. Atomically thin noble metal dichalcogenide: A broadband mid-infrared semiconductor. *Nat. Commun.* **2018**, *9*, 1545.

[53] Zhang, G.; Amani, M.; Chaturvedi, A.; Tan, C. L.; Bullock, J.; Song, X. H.; Kim, H.; Lien, D. H.; Scott, M. C.; Zhang, H. et al. Optical and electrical properties of two-dimensional palladium diselenide. *Appl. Phys. Lett.* **2019**, *114*, 253102.

[54] Zeng, L. H.; Wu, D.; Lin, S. H.; Xie, C.; Yuan, H. Y.; Lu, W.; Lau, S. P.; Chai, Y.; Luo, L. B.; Li, Z. J. et al. Controlled synthesis of 2D palladium diselenide for sensitive photodetector applications. *Adv. Funct. Mater.* **2019**, *29*, 1806878.

[55] Sefidmooye Azar, N.; Bullock, J.; Shrestha, V. R.; Balendhran, S.; Yan, W.; Kim, H.; Javey, A.; Crozier, K. B. Long-wave infrared photodetectors based on 2D platinum diselenide atop optical cavity substrates. *ACS Nano* **2021**, *15*, 6573–6581.

[56] Prechtl, M.; Parhizkar, S.; Hartwig, O.; Lee, K.; Biba, J.; Stimpel-Lindner, T.; Gity, F.; Schels, A.; Bolten, J.; Suckow, S. et al. Hybrid devices by selective and conformal deposition of PtSe₂ at low temperatures. *Adv. Funct. Mater.* **2021**, *31*, 2103936.

[57] Dong, Z.; Yu, W. Z.; Zhang, L. B.; Mu, H. R.; Xie, L.; Li, J.; Zhang, Y.; Huang, L. Y.; He, X. Y.; Wang, L. et al. Highly

efficient, ultrabroad PdSe$_2$ phototransistors from visible to terahertz driven by mutiphysical mechanism. *ACS Nano* 2021, *15*, 20403–20413.

[58] Xu, W. T.; Jiang, J. Y.; Ma, H. F.; Zhang, Z. W.; Li, J.; Zhao, B.; Wu, R. X.; Yang, X. D.; Zhang, H. M.; Li, B. L. et al. Vapor phase growth of two-dimensional PdSe$_2$ nanosheets for high-photoresponsivity near-infrared photodetectors. *Nano Res.* 2020, *13*, 2091–2097.

[59] Luo, L. B.; Wang, D.; Xie, C.; Hu, J. G.; Zhao, X. Y.; Liang, F. X. PdSe$_2$ multilayer on germanium nanocones array with light trapping effect for sensitive infrared photodetector and image sensing application. *Adv. Funct. Mater.* 2019, *29*, 1900849.

[60] Liang, F. X.; Zhao, X. Y.; Jiang, J. J.; Hu, J. G.; Xie, W. Q.; Lv, J.; Zhang, Z. X.; Wu, D.; Luo, L. B. Light confinement effect induced highly sensitive, self-driven near-infrared photodetector and image sensor based on multilayer PdSe$_2$/pyramid Si heterojunction. *Small* 2019, *15*, 1903831.

[61] Long, M. S.; Wang, Y.; Wang, P.; Zhou, X. H.; Xia, H.; Luo, C.; Huang, S. Y.; Zhang, G. W.; Yan, H. G.; Fan, Z. Y. et al. Palladium diselenide long-wavelength infrared photodetector with high sensitivity and stability. *ACS Nano* 2019, *13*, 2511–2519.

[62] Afzal, A. M.; Dastgeer, G.; Iqbal, M. Z.; Gautam, P.; Faisal, M. M. High-performance p-BP/n-PdSe$_2$ near-infrared photodiodes with a fast and gate-tunable photoresponse. *ACS Appl. Mater. Interfaces* 2020, *12*, 19625–19634.

[63] Wu, D.; Mo, Z. H.; Han, Y. B.; Lin, P.; Shi, Z. F.; Chen, X.; Tian, Y. T.; Li, X. J.; Yuan, H. Y.; Tsang, Y. H. Fabrication of 2D PdSe$_2$/3D CdTe mixed-dimensional van der Waals heterojunction for broadband infrared detection. *ACS Appl. Mater. Interfaces* 2021, *13*, 41791–41801.

[64] Wu, D.; Wang, Y. G.; Zeng, L. H.; Jia, C.; Wu, E. P.; Xu, T. T.; Shi, Z. F.; Tian, Y. T.; Li, X. J.; Tsang, Y. H. Design of 2D layered PtSe$_2$ heterojunction for the high-performance, room-temperature, broadband, infrared photodetector. *ACS Photonics* 2018, *5*, 3820–3827.

[65] Yuan, J.; Sun, T.; Hu, Z. X.; Yu, W. Z.; Ma, W. L.; Zhang, K.; Sun, B. Q.; Lau, S. P.; Bao, Q. L.; Lin, S. H. et al. Wafer-scale fabrication of two-dimensional PtS$_2$/PtSe$_2$ heterojunctions for efficient and broad band photodetection. *ACS Appl. Mater. Interfaces* 2018, *10*, 40614–40622.

[66] Afzal, A. M.; Iqbal, M. Z.; Dastgeer, G.; ul. Ahmad, A.; Park, B. Highly sensitive, ultrafast, and broadband photo-detecting field-effect transistor with transition-metal dichalcogenide van der Waals heterostructures of MoTe$_2$ and PdSe$_2$. *Adv. Sci.* 2021, *8*, 2003713.

[67] Ahmad, W.; Liu, J. D.; Jiang, J. Z.; Hao, Q. Y.; Wu, D.; Ke, Y. X.; Gan, H. B.; Laxmi, V.; Ouyang, Z. B.; Ouyang, F. P. et al. Strong interlayer transition in few-layer InSe/PdSe$_2$ van der Waals heterostructure for near-infrared photodetection. *Adv. Funct. Mater.* 2021, *31*, 2104143.

[68] Wu, D.; Jia, C.; Shi, F. H.; Zeng, L. H.; Lin, P.; Dong, L.; Shi, Z. F.; Tian, Y. T.; Li, X. J.; Jie, J. S. Mixed-dimensional PdSe$_2$/SiNWA heterostructure based photovoltaic detectors for self-driven, broadband photodetection, infrared imaging and humidity sensing. *J. Mater. Chem. A* 2020, *8*, 3632–3642.

[69] Liang, Q. J.; Wang, Q. X.; Zhang, Q.; Wei, J. X.; Lim, S. X.; Zhu, R.; Hu, J. X.; Wei, W.; Lee, C.; Sow, C. et al. High-performance, room temperature, ultra-broadband photodetectors based on air-stable PdSe$_2$. *Adv. Mater.* 2019, *31*, 1807609.

[70] Zhong, J. H.; Yu, J.; Cao, L. K.; Zeng, C.; Ding, J. N.; Cong, C. X.; Liu, Z. W.; Liu, Y. P. High-performance polarization-sensitive photodetector based on a few-layered PdSe$_2$ nanosheet. *Nano Res.* 2020, *13*, 1780–1786.

[71] Zeng, L. H.; Chen, Q. M.; Zhang, Z. X.; Wu, D.; Yuan, H. Y.; Li, Y. Y.; Qarony, W.; Lau, S. P.; Luo, L. B.; Tsang, Y. H. Multilayered PdSe$_2$/perovskite schottky junction for fast, self-powered, polarization-sensitive, broadband photodetectors, and image sensor application. *Adv. Sci.* 2019, *6*, 1901134.

[72] Wu, D.; Guo, J. W.; Du, J.; Xia, C. X.; Zeng, L. H.; Tian, Y. Z.; Shi, Z. F.; Tian, Y. T.; Li, X. J.; Tsang, Y. H. et al. Highly polarization-sensitive, broadband, self-powered photodetector

based on graphene/PdSe$_2$/germanium heterojunction. *ACS Nano* 2019, *13*, 9907–9917.

[73] Tran, V.; Soklaski, R.; Liang, Y. F.; Yang, L. Layer-controlled band gap and anisotropic excitons in few-layer black phosphorus. *Phys. Rev. B* 2014, *89*, 235319.

[74] Guo, Q. S.; Pospischil, A.; Bhuiyan, M.; Jiang, H.; Tian, H.; Farmer, D.; Deng, B. C.; Li, C.; Han, S. J.; Wang, H. et al. Black phosphorus mid-infrared photodetectors with high gain. *Nano Lett.* 2016, *16*, 4648–4655.

[75] Hu, G. H.; Albrow-Owen, T.; Jin, X. X.; Ali, A.; Hu, Y. W.; Howe, R. C. T.; Shehzad, K.; Yang, Z. Y.; Zhu, X. K.; Woodward, R. I. et al. Black phosphorus ink formulation for inkjet printing of optoelectronics and photonics. *Nat. Commun.* 2017, *8*, 278.

[76] Phaneuf-L'Heureux, A. L.; Favron, A.; Germain, J. F.; Lavoie, P.; Desjardins, P.; Leonelli, R.; Martel, R.; Francoeur, S. Polarization-resolved raman study of bulk-like and davydov-induced vibrational modes of exfoliated black phosphorus. *Nano Lett.* 2016, *16*, 7761–7767.

[77] Li, Y. Y.; Hu, Z. X.; Lin, S. H.; Lai, S. K.; Ji, W.; Lau, S. P. Giant anisotropic raman response of encapsulated ultrathin black phosphorus by uniaxial strain. *Adv. Funct. Mater.* 2017, *27*, 1600986.

[78] Bullock, J.; Amani, M.; Cho, J.; Chen, Y. Z.; Ahn, G. H.; Adinolfi, V.; Shrestha, V. R.; Gao, Y.; Crozier, K. B.; Chueh, Y. L. et al. Polarization-resolved black phosphorus/molybdenum disulfide mid-wave infrared photodiodes with high detectivity at room temperature. *Nat. Photonics* 2018, *12*, 601–607.

[79] Liu, T. T.; Jiang, X. Y.; Zhou, C. B.; Xiao, S. Y. Black phosphorus-based anisotropic absorption structure in the mid-infrared. *Opt. Express* 2019, *27*, 27618–27627.

[80] Miao, J. S.; Song, B.; Xu, Z. H.; Cai, L.; Zhang, S. M.; Dong, L. X.; Wang, C. Single pixel black phosphorus photodetector for near-infrared imaging. *Small* 2018, *14*, 1702082.

[81] Ma, Y. M.; Dong, B. W.; Wei, J. X.; Chang, Y. H.; Huang, L.; Ang, K. W.; Lee, C. High-responsivity mid-infrared black phosphorus slow light waveguide photodetector. *Adv. Opt. Mater.* 2020, *8*, 2000337.

[82] Huang, L.; Dong, B.; Yu, Z. G.; Zhou, J.; Ma, Y.; Zhang, Y. W.; Lee, C.; Ang, K. W. Mid-infrared modulators integrating silicon and black phosphorus photonics. *Mater. Today Adv.* 2021, *12*, 100170.

[83] Xu, Y. J.; Liu, C. L.; Guo, C.; Yu, Q.; Guo, W. L.; Lu, W.; Chen, X. S.; Wang, L.; Zhang, K. High performance near infrared photodetector based on in-plane black phosphorus p-n homojunction. *Nano Energy* 2020, *70*, 104518.

[84] Yu, X. C.; Zhang, S. L.; Zeng, H. B.; Wang, Q. J. Lateral black phosphorene P-N junctions formed via chemical doping for high performance near-infrared photodetector. *Nano Energy* 2016, *25*, 34–41.

[85] Ye, L.; Li, H.; Chen, Z. F.; Xu, J. B. Near-infrared photodetector based on MoS$_2$/black phosphorus heterojunction. *ACS Photonics* 2016, *3*, 692–699.

[86] Ye, L.; Wang, P.; Luo, W. J.; Gong, F.; Liao, L.; Liu, T. D.; Tong, L.; Zang, J. F.; Xu, J. B.; Hu, W. D. Highly polarization sensitive infrared photodetector based on black phosphorus-on-WSe$_2$ photogate vertical heterostructure. *Nano Energy* 2017, *37*, 53–60.

[87] Zhang, X. M.; Yan, C. L.; Hu, X.; Dong, Q. S.; Liu, Z. Y.; Lv, W. M.; Zeng, C. H.; Su, R. G.; Wang, Y. Q.; Sun, T. Y. et al. High performance mid-wave infrared photodetector based on graphene/black phosphorus heterojunction. *Mater. Res. Express* 2021, *8*, 035602.

[88] Liang, J. C.; Hu, Y.; Zhang, K. Q.; Wang, Y. D.; Song, X. M.; Tao, A. Y.; Liu, Y. Z.; Jin, Z. 2D layered black arsenic-phosphorus materials: Synthesis, properties, and device applications. *Nano Res.* 2022, *15*, 3737–3752.

[89] Long, M. S.; Gao, A. Y.; Wang, P.; Xia, H.; Ott, C.; Pan, C.; Fu, Y. J.; Liu, E. F.; Chen, X. S.; Lu, W. et al. Room temperature high-detectivity mid-infrared photodetectors based on black arsenic phosphorus. *Sci. Adv.* 2017, *3*, e1700589.

[90] Liu, Y. J.; Wang, H. D.; Wang, S.; Wang, Y. J.; Wang, Y. Z.; Guo,

Z. N.; Xiao, S. M.; Yao, Y.; Song, Q. H.; Zhang, H. et al. Highly efficient silicon photonic microheater based on black arsenic-phosphorus. *Adv. Opt. Mater.* **2020**, *8*, 1901526.

[91] Yu, L.; Zhu, Z.; Gao, A. Y.; Wang, J. Z.; Miao, F.; Shi, Y.; Wang, X. M. Electrically tunable optical properties of few-layer black arsenic phosphorus. *Nanotechnology* **2018**, *29*, 484001.

[92] Zhong, M. Z.; Meng, H. T.; Ren, Z. H.; Huang, L.; Yang, J. H.; Li, B.; Xia, Q. L.; Wang, X. T.; Wei, Z. M.; He, J. Gate-controlled ambipolar transport in b-AsP crystals and their VIS-NIF photodetection. *Nanoscale* **2021**, *13*, 10579–10586.

[93] Gong, F.; Wu, F.; Long, M. S.; Chen, F. S.; Su, M.; Yang, Z. Y.; Shi, J. Black phosphorus infrared photodetectors with fast response and high photoresponsivity. *Phys. Status Solidi (RRL) - Rapid Res. Lett.* **2018**, *12*, 1800310.

[94] Chen, X. L.; Lu, X. B.; Deng, B. C.; Sinai, O.; Shao, Y. C.; Li, C.; Yuan, S. F.; Tran, V.; Watanabe, K.; Taniguchi, T. et al. Widely tunable black phosphorus mid-infrared photodetector. *Nat. Commun.* **2017**, *8*, 1672.

[95] Yuan, S. F.; Shen, C. F.; Deng, B. C.; Chen, X. L.; Guo, Q. S.; Ma, Y. Q.; Abbas, A.; Liu, B. L.; Haiges, R.; Ott, C. et al. Air-stable room-temperature mid-infrared photodetectors based on hBN/black arsenic phosphorus/hBN heterostructures. *Nano Lett.* **2018**, *18*, 3172–3179.

[96] Wu, J. X.; Yuan, H. T.; Meng, M. M.; Chen, C.; Sun, Y.; Chen, Z. Y.; Dang, W. H.; Tan, C. W.; Liu, Y. J.; Yin, J. B. et al. High electron mobility and quantum oscillations in non-encapsulated ultrathin semiconducting $Bi_2O_2Se$. *Nat. Nanotechnol.* **2017**, *12*, 530–534.

[97] Wei, Q. L.; Li, R. P.; Lin, C. Q.; Han, A. L.; Nie, A. M.; Li, Y. R.; Li, L. J.; Cheng, Y. C.; Huang, W. Quasi-two-dimensional Se-terminated bismuth oxychalcogenide ($Bi_2O_2Se$). *ACS Nano* **2019**, *13*, 13439–13444.

[98] Sun, Y.; Zhang, J.; Ye, S.; Song, J.; Qu, J. L. Progress report on property, preparation, and application of $Bi_2O_2Se$. *Adv. Funct. Mater.* **2020**, *30*, 2004480.

[99] Yin, J. B.; Tan, Z. J.; Hong, H.; Wu, J. X.; Yuan, H. T.; Liu, Y. J.; Chen, C.; Tan, C. W.; Yao, F. R.; Li, T. R. et al. Ultrafast and highly sensitive infrared photodetectors based on two-dimensional oxyselenide crystals. *Nat. Commun.* **2018**, *9*, 3311.

[100] Li, J.; Wang, Z.; Wen, Y.; Chu, J.; Yin, L.; Cheng, R.; Lei, L.; He, P.; Jiang, C.; Feng, L.; He, J. High-Performance Near-Infrared Photodetector Based on Ultrathin $Bi_2O_2Se$ Nanosheets. *Advanced Functional Materials* **2018**, *28*.

[101] Ma, X. Y.; Chang, D. H.; Zhao, C. X.; Li, R.; Huang, X. Y.; Zeng, Z. P.; Huang, X. W.; Jia, Y. Geometric structures and electronic properties of the $Bi_2X_2Y$ (X, Y = O, S, Se, and Te) ternary compound family: A systematic DFT study. *J. Mater. Chem. C* **2018**, *6*, 13241–13249.

[102] Chitara, B.; Limbu, T. B.; Orlando, J. D.; Tang, Y. G.; Yan, F. Ultrathin $Bi_2O_2S$ nanosheet near-infrared photodetectors. *Nanoscale* **2020**, *12*, 16285–16291.

[103] Yang, X. X.; Qu, L. H.; Gao, F.; Hu, Y. X.; Yu, H.; Wang, Y. X.; Cui, M. Q.; Zhang, Y. X.; Fu, Z. D.; Huang, Y. W. et al. High-performance broadband photoelectrochemical photodetectors based on ultrathin $Bi_2O_2S$ nanosheets. *ACS Appl. Mater. Interfaces* **2022**, *14*, 7175–7183.

[104] Tian, P.; Wu, H. B.; Tang, L. B.; Xiang, J. Z.; Ji, R. B.; Lau, S. P.; Teng, K. S.; Guo, W.; Yao, Y. G.; Li, L. J. Ultrasensitive broadband photodetectors based on two-dimensional $Bi_2O_2Te$ films. *J. Mater. Chem. C* **2021**, *9*, 13713–13721.

[105] Wang, F. K.; Yang, S. J.; Wu, J.; Hu, X. Z.; Li, Y.; Li, H. Q.; Liu, X. T.; Luo, J. H.; Zhai, T. Y. Emerging two-dimensional bismuth oxychalcogenides for electronics and optoelectronics. *InfoMat* **2021**, *3*, 1251–1271.

[106] Ulaganathan, R. K.; Sankar, R.; Lin, C. Y.; Murugesan, R. C.; Tang, K. C.; Chou, F. C. High-performance flexible broadband photodetectors based on 2D hafnium selenosulfide nanosheets. *Adv. Electron. Mater.* **2020**, *6*, 1900794.

[107] Du, L. N.; Wang, C.; Fang, J. Z.; Wei, B.; Xiong, W. Q.; Wang, X.

[108] Xu, T. F.; Luo, M.; Shen, N. M.; Yu, Y. Y.; Wang, Z.; Cui, Z. Z.; Qin, J. Y.; Liang, F.; Chen, Y. F.; Zhou, Y. et al. Ternary 2D layered material $FePSe_3$ and near-infrared photodetector. *Adv. Electron. Mater.* **2021**, *7*, 2100207.

[109] Kang, P. P.; Nan, H. Y.; Zhang, X. M.; Mo, H. X.; Ni, Z. H.; Gu, X. F.; Ostrikov, K.; Xiao, S. Q. Controllable synthesis of crystalline $ReS_{2(1-x)}Se_{2x}$ monolayers on amorphous $SiO_2$/Si substrates with fast photoresponse. *Adv. Opt. Mater.* **2020**, *8*, 1901415.

[110] Luo, P.; Pei, K.; Wang, F. K.; Feng, X.; Li, H. Q.; Liu, X. T.; Luo, J. H.; Zhai, T. Y. Ultrathin 2D ternary $Bi_2Te_2Se$ flakes for fast-response photodetectors with gate-tunable responsivity. *Sci. China Mater.* **2021**, *64*, 3017–3026.

[111] Chen, J. W.; Li, L.; Gong, P. L.; Zhang, H. L.; Yin, S. Q.; Li, M.; Wu, L. F.; Gao, W. S.; Long, M. S.; Shan, L. et al. A submicrosecond-response ultraviolet-visible-near-infrared broadband photodetector based on 2D tellurosilicate $InSiTe_3$. *ACS Nano* **2022**, *16*, 7745–7754.

[112] Qiao, J.; Feng, F.; Song, S.; Wang, T.; Shen, M. Y.; Zhang, G. P.; Yuan, X. C.; Somekh, M. G. Perovskite quantum dot-$Ta_2NiSe_5$ mixed-dimensional van der waals heterostructures for high-performance near-infrared photodetection. *Adv. Funct. Mater.* **2022**, *32*, 2110706.

[113] Xu, G. L.; Liu, D. M.; Li, S. Y.; Wu, Y.; Zhang, Z. L.; Wang, S. B.; Huang, Z. K.; Zhang, Y. Z. Binary-ternary transition metal chalcogenides interlayer coupling in van der Waals type-II heterostructure for visible-infrared photodetector with efficient suppression dark currents. *Nano Res.* **2022**, *15*, 2689–2696.

[114] Yang, T.; Li, X.; Wang, L. M.; Liu, Y. M.; Chen, K. J.; Yang, X.; Liao, L.; Dong, L.; Shan, C. X. Broadband photodetection of 2D $Bi_2O_2Se$-$MoSe_2$ heterostructure. *J. Mater. Sci.* **2019**, *54*, 14742–14751.

[115] Yang, S. J.; Luo, P.; Wang, F. K.; Liu, T.; Zhao, Y. H.; Ma, Y.; Li, H. Q.; Zhai, T. Y. Van der Waals epitaxy of $Bi_2Te_2Se$/$Bi_2O_2Se$ vertical heterojunction for high performance photodetector. *Small* **2022**, *18*, 2105211.

[116] Arora, H.; Dong, R. H.; Venanzi, T.; Zscharschuch, J.; Schneider, H.; Helm, M.; Feng, X. L.; Cánovas, E.; Erbe, A. Demonstration of a broadband photodetector based on a two-dimensional metal-organic framework. *Adv. Mater.* **2020**, *32*, 1907063.

[117] Chung, Y. K.; Lee, J.; Lee, W. G.; Sung, D.; Chae, S.; Oh, S.; Choi, K. H.; Kim, B. J.; Choi, J. Y.; Huh, J. Theoretical study of anisotropic carrier mobility for two-dimensional $Nb_2Se_9$ material. *ACS Omega* **2021**, *6*, 26782–26790.

[118] Kecik, D.; Özçelik, V. O.; Durgun, E.; Ciraci, S. Structure dependent optoelectronic properties of monolayer antimonene, bismuthene and their binary compound. *Phys. Chem. Chem. Phys.* **2019**, *21*, 7907–7917.

[119] Xu, H.; Ren, A. B.; Wu, J.; Wang, Z. M. Recent advances in 2D MXenes for photodetection. *Adv. Funct. Mater.* **2020**, *30*, 2000907.

[120] Wang, B.; Zhong, S. P.; Xu, P.; Zhang, H. Booming development and present advances of two dimensional MXenes for photodetectors. *Chem. Eng. J.* **2021**, *403*, 126336.

[121] Hu, C. Q.; Li, L.; Shen, G. Z. Flexible transparent near-infrared photodetector based on 2D $Ti_3C_2$ MXene-Te van der Waals heterostructures. *Chin. J. Chem.* **2021**, *39*, 2141–2146.

[122] Ren, A. B.; Zou, J. H.; Lai, H. G.; Huang, Y. X.; Yuan, L. M.; Xu, H.; Shen, K.; Wang, H.; Wei, S. Y.; Wang, Y. F. et al. Direct laser-patterned MXene-perovskite image sensor arrays for visible-near infrared photodetection. *Mater. Horiz.* **2020**, *7*, 1901–1911.

[123] Yang, C. M.; Qin, S. Y.; Zuo, Y.; Shi, Y.; Bie, T.; Shao, M.; Yu, Y. Waveguide schottky photodetector with tunable barrier based on $Ti_3C_2T_x$/p-Si van der Waals heterojunction. *Nanophotonics* **2021**, *10*, 4133–4139.

[124] Zhang, X. W.; Shao, J. H.; Yan, C. X.; Wang, X. M.; Wang, Y. F.; Lu, Z. H.; Qin, R. J.; Huang, X. W.; Tian, J. L.; Zeng, L. H. High performance broadband self-driven photodetector based on MXene ($Ti_3C_2T_x$)/GaAs Schottky junction. *Mater. Des.* **2021**, *207*, 109850.

[125] Shi, Z.; Cao, R.; Khan, K.; Tareen, A. K.; Liu, X. S.; Liang, W. Y.;

Zhang, Y.; Ma, C. Y.; Guo, Z. N.; Luo, X. L. et al. Two-dimensional tellurium: Progress, challenges, and prospects. *Nano-Micro Lett.* **2020**, *12*, 99.

[126] Gao, S. Y.; Sun, C. Q.; Zhang, X. Ultra-strong anisotropic photo-responsivity of bilayer tellurene: A quantum transport and time-domain first principle study. *Nanophotonics* **2020**, *9*, 1931–1940.

[127] Amani, M.; Tan, C. L.; Zhang, G.; Zhao, C. S.; Bullock, J.; Song, X. H.; Kim, H.; Shrestha, V. R.; Gao, Y.; Crozier, K. B. et al. Solution-synthesized high-mobility tellurium nanoflakes for short-wave infrared photodetectors. *ACS Nano* **2018**, *12*, 7253–7263.

[128] Peng, M.; Xie, R. Z.; Wang, Z.; Wang, P.; Wang, F.; Ge, H. N.; Wang, Y.; Zhong, F.; Wu, P. S.; Ye, J. F. et al. Blackbody-sensitive room-temperature infrared photodetectors based on low-dimensional tellurium grown by chemical vapor deposition. *Sci. Adv.* **2021**, *7*, eabf7358.

[129] Wang, X. T.; Li, Y. T.; Huang, L.; Jiang, X. W.; Jiang, L.; Dong, H. L.; Wei, Z. M.; Li, J. B.; Hu, W. P. Short-wave near-infrared linear dichroism of two-dimensional germanium selenide. *J. Am. Chem. Soc.* **2017**, *139*, 14976–14982.

[130] Wang, X. T.; Zhong, F.; Kang, J.; Liu, C.; Lei, M.; Pan, L. F.; Wang, H. L.; Wang, F.; Zhou, Z. Q.; Cui, Y. et al. Polarizer-free polarimetric image sensor through anisotropic two-dimensional GeSe. *Sci. China Mater.* **2021**, *64*, 1230–1237.

[131] Chen, Y.; Wang, X. D.; Wu, G. J.; Wang, Z.; Fang, H. H.; Lin, T.; Sun, S.; Shen, H.; Hu, W. D.; Wang, J. L. et al. High-performance photovoltaic detector based on MoTe$_2$/MoS$_2$ Van der Waals heterostructure. *Small* **2018**, *14*, 1703293.

[132] Wu, H. L.; Kang, Z.; Zhang, Z. H.; Zhang, Z.; Si, H. N.; Liao, Q. L.; Zhang, S. C.; Wu, J.; Zhang, X. K.; Zhang, Y. Interfacial charge behavior modulation in perovskite quantum dot-monolayer MoS$_2$ 0D-2D mixed-dimensional van der Waals heterostructures. *Adv. Funct. Mater.* **2018**, *28*, 1802015.

[133] Tan, C. Y.; Yin, S. Q.; Chen, J. W.; Lu, Y.; Wei, W. S.; Du, H. F.; Liu, K. L.; Wang, F. K.; Zhai, T. Y.; Li, L. Broken-gap PtS$_2$/WSe$_2$ van der Waals heterojunction with ultrahigh reverse rectification and fast photoresponse. *ACS Nano* **2021**, *15*, 8328–8337.

[134] Du, Y. X.; Liu, H.; Hu, J. X.; Deng, L. E.; Bai, Y.; Bai, M. Y.; Xie, F. First-principles study of the electronic and optical properties of Bi$_2$Se$_3$/MoSe$_2$ heterojunction. *Phys. Status Solidi (B)* **2021**, *258*, 2100403.

[135] Yan, X.; Liu, C. S.; Li, C.; Bao, W. Z.; Ding, S. J.; Zhang, D. W.; Zhou, P. Tunable SnSe$_2$/WSe$_2$ heterostructure tunneling field effect transistor. *Small* **2017**, *13*, 1701478.

[136] Wu, Z. T.; Zhu, N. C.; Jiang, J.; Zafar, A.; Hong, J. T.; Zhang, Y. Tuning interlayer coupling by laser irradiation and broadband photodetection in vertical MoTe$_2$/WS$_2$ vdW heterostructure. *APL Mater.* **2019**, *7*, 041108.

[137] Mukherjee, S.; Jana, S.; Sinha, T. K.; Das, S.; Ray, S. K. Infrared tunable, two colour-band photodetectors on flexible platforms using 0D/2D PbS-MoS$_2$ hybrids. *Nanoscale Adv.* **2019**, *1*, 3279–3287.

[138] Kim, H. S.; Patel, M.; Kim, J.; Jeong, M. S. Growth of wafer-scale standing layers of WS$_2$ for self-biased high-speed UV-visible-NIR optoelectronic devices. *ACS Appl. Mater. Interfaces* **2018**, *10*, 3964–3974.

[139] Zhang, Y. N.; Yun, J. N.; Zhang, S. Y.; Zeng, L. R.; Bi, Z. S.; Huang, N. N.; Kang, P.; Yan, J. F.; Zhao, W.; Zhang, Z. Y. et al. Self-powered near-infrared photodetector based on graphyne/hexagonal boron phosphide heterostructure with high responsivity and robustness: A theoretical study. *Appl. Surf. Sci.* **2021**, *569*, 151035.

[140] Wang, Y. G.; Huang, X. W.; Wu, D.; Zhuo, R. R.; Wu, E. P.; Jia, C.; Shi, Z. F.; Xu, T. T.; Tian, Y. T.; Li, X. J. A room-temperature near-infrared photodetector based on a MoS$_2$/CdTe p-n heterojunction with a broadband response up to 1,700 nm. *J. Mater. Chem. C* **2018**, *6*, 4861–4865.

[141] Sun, Y.; Hu, R. X.; An, C. H.; Ma, X. L.; Zhang, J.; Liu, J. Visible to near-infrared photodetector based on SnSe$_2$/WSe$_2$ heterojunction with potential application in artificial visual neuron. *Nanotechnology* **2021**, *32*, 475206.

[142] Luo, P.; Zhuge, F. W.; Wang, F. K.; Lian, L. Y.; Liu, K. L.; Zhang, J. B.; Zhai, T. Y. PbSe quantum dots sensitized high-mobility Bi$_2$O$_2$Se nanosheets for high-performance and broadband photodetection beyond 2 μm. *ACS Nano* **2019**, *13*, 9028–9037.

[143] Wang, Z. Y.; Zhang, X. W.; Wu, D.; Guo, J. W.; Zhao, Z. H.; Shi, Z. F.; Tian, Y. T.; Huang, X. W.; Li, X. J. Construction of mixed-dimensional WS$_2$/Si heterojunctions for high-performance infrared photodetection and imaging applications. *J. Mater. Chem. C* **2020**, *8*, 6877–6882.

[144] Ross, J. S.; Rivera, P.; Schaibley, J.; Lee-Wong, E.; Yu, H. Y.; Taniguchi, T.; Watanabe, K.; Yan, J. Q.; Mandrus, D.; Cobden, D. et al. Interlayer exciton optoelectronics in a 2D heterostructure p-n junction. *Nano Lett.* **2017**, *17*, 638–643.

[145] Mueller, T.; Malic, E. Exciton physics and device application of two-dimensional transition metal dichalcogenide semiconductors. *npj 2D Mater. Appl.* **2018**, *2*, 29.

[146] Qi, T. L.; Gong, Y. P.; Li, A. L.; Ma, X. M.; Wang, P. P.; Huang, R.; Liu, C.; Sakidja, R.; Wu, J. Z.; Chen, R. et al. Interlayer transition in a vdW heterostructure toward ultrahigh detectivity shortwave infrared photodetectors. *Adv. Funct. Mater.* **2020**, *30*, 1905687.

[147] Lukman, S.; Ding, L.; Xu, L.; Tao, Y.; Riis-Jensen, A. C.; Zhang, G.; Wu, Q. Y. S.; Yang, M.; Luo, S.; Hsu, C. et al. High oscillator strength interlayer excitons in two-dimensional heterostructures for mid-infrared photodetection. *Nat. Nanotechnol.* **2020**, *15*, 675–682.

[148] Inbaraj, C. R. P.; Mathew, R. J.; Ulaganathan, R. K.; Sankar, R.; Kataria, M.; Lin, H. Y.; Cheng, H. Y.; Lin, K. H.; Lin, H. I.; Liao, Y. M. et al. Modulating charge separation with hexagonal boron nitride mediation in vertical van der Waals heterostructures. *ACS Appl. Mater. Interfaces* **2020**, *12*, 26213–26221.

[149] Shen, N. F.; Yang, X. D.; Wang, X. X.; Wang, G. H.; Wan, J. G. Two-dimensional van der Waals heterostructure of indium selenide/hexagonal boron nitride with strong interlayer coupling. *Chem. Phys. Lett.* **2020**, *749*, 137430.

[150] Fang, H. H.; Wu, P. S.; Wang, P.; Zheng, Z.; Tang, Y. C.; Ho, J. C.; Chen, G.; Wang, Y. M.; Shan, C. X.; Cheng, X. B. et al. Global photocurrent generation in phototransistors based on single-walled carbon nanotubes toward highly sensitive infrared detection. *Adv. Opt. Mater.* **2019**, *7*, 1900597.

[151] Ogawa, S.; Fukushima, S.; Okuda, S.; Shimatani, M. Graphene nanoribbon photogating for graphene-based infrared photodetectors. In *Proceedings of SPIE 11741, Infrared Technology and Applications XLVII*, 2021, pp 117411H.

[152] Wen, H.; Xiong, L.; Tan, C. B.; Zhu, K. M.; Tang, Y.; Wang, J. B.; Zhong, X. L. Localized electric-field-enhanced low-light detection by a 2D SnS visible-light photodetector. *Chin. Phys. B* **2021**, *30*, 057803.

[153] Wang, X. Z.; Pan, D.; Sun, M.; Lyu, F. J.; Zhao, J. H.; Chen, Q. High-performance room-temperature UV-IR photodetector based on the InAs nanosheet and its wavelength-and intensity-dependent negative photoconductivity. *ACS Appl. Mater. Interfaces* **2021**, *13*, 26187–26195.

[154] Huang, H.; Wang, J. L.; Hu, W. D.; Liao, L.; Wang, P.; Wang, X. D.; Gong, F.; Chen, Y.; Wu, G. J.; Luo, W. J. et al. Highly sensitive visible to infrared MoTe$_2$ photodetectors enhanced by the photogating effect. *Nanotechnology* **2016**, *27*, 445201.

[155] Hao, L. Z.; Du, Y. J.; Wang, Z. G.; Wu, Y. P.; Xu, H. Y.; Dong, S. C.; Liu, H.; Liu, Y. J.; Xue, Q. Z.; Han, Z. D. et al. Wafer-size growth of 2D layered SnSe films for UV-visible-NIR photodetector arrays with high responsivity. *Nanoscale* **2020**, *12*, 7358–7365.

[156] Shen, C. F.; Liu, Y. H.; Wu, J. B.; Xu, C.; Cui, D. Z.; Li, Z.; Liu, Q. Z.; Li, Y. R.; Wang, Y. X.; Cao, X. et al. Tellurene photodetector with high gain and wide bandwidth. *ACS Nano* **2020**, *14*, 303–310.

[157] Wang, F. K.; Wu, J.; Zhang, Y.; Yang, S. J.; Zhang, N.; Li, H. Q.; Zhai, T. Y. High-sensitivity shortwave infrared photodetectors of metal-organic frameworks integrated on 2D layered materials. *Sci. China Mater.* **2022**, *65*, 451–459.

[158] Shen, T.; Li, F.; Zhang, Z. Y.; Xu, L.; Qi, J. J. High-performance broadband photodetector based on monolayer MoS$_2$ hybridized with environment-friendly CuInSe$_2$ quantum dots. *ACS Appl. Mater. Interfaces* **2020**, *12*, 54927–54935.

[159] Ilyas, N.; Li, D. Y.; Song, Y. H.; Zhong, H.; Jiang, Y. D.; Li, W. Low-dimensional materials and state-of-the-art architectures for infrared photodetection. *Sensors* **2018**, *18*, 4163.

[160] Zha, J. J.; Luo, M. C.; Ye, M.; Ahmed, T.; Yu, X. C.; Lien, D. H.; He, Q. Y.; Lei, D. Y.; Ho, J. C.; Bullock, J. et al. Infrared photodetectors based on 2D materials and nanophotonics. *Adv. Funct. Mater.* **2022**, *32*, 2111970.

[161] Liu, T. D.; Tong, L.; Huang, X. Y.; Ye, L. Room-temperature infrared photodetectors with hybrid structure based on two-dimensional materials. *Chin. Phys. B* **2019**, *28*, 017302.

[162] Wang, W. Y.; Klots, A.; Prasai, D.; Yang, Y. M.; Bolotin, K. I.; Valentine, J. Hot electron-based near-infrared photodetection using bilayer MoS$_2$. *Nano Lett.* **2015**, *15*, 7440–7444.

[163] Jeon, J.; Choi, H.; Choi, S.; Park, J. H.; Lee, B. H.; Hwang, E.; Lee, S. Transition-metal-carbide (Mo$_2$C) multiperiod gratings for realization of high-sensitivity and broad-spectrum photodetection. *Adv. Funct. Mater.* **2019**, *29*, 1905384.

[164] Dai, M. J.; Chen, H. Y.; Feng, R.; Feng, W.; Hu, Y. X.; Yang, H. H.; Liu, G. B.; Chen, X. S.; Zhang, J.; Xu, C. Y. et al. A dual-band multilayer InSe self-powered photodetector with high performance induced by surface plasmon resonance and asymmetric schottky junction. *ACS Nano* **2018**, *12*, 8739–8747.

[165] Nakazawa, T.; Kim, D.; Kato, S.; Park, J.; Nam, J.; Kim, H. Photocurrent enhancement of PtSe$_2$ photodetectors by using au nanorods. *Photonics* **2021**, *8*, 505.

[166] Guo, J. X.; Li, S. D.; He, Z. B.; Li, Y. Y.; Lei, Z. C.; Liu, Y.; Huang, W.; Gong, T. X.; Ai, Q. Q.; Mao, L. N. et al. Near-infrared photodetector based on few-layer MoS$_2$ with sensitivity enhanced by localized surface plasmon resonance. *Appl. Surf. Sci.* **2019**, *483*, 1037–1043.

[167] Zhang, D. H.; Zhou, J.; Liu, C. L.; Guo, S. K.; Deng, J. N.; Cai, Q. Y.; Li, Z. F.; Zhang, Y. F.; Zhang, W. Q.; Chen, X. S. Enhanced polarization sensitivity by plasmonic-cavity in graphene phototransistors. *J. Appl. Phys.* **2019**, *126*, 074301.

[168] Yakimov, A. I.; Bloshkin, A. A.; Dvurechenskii, A. V. Plasmonic field enhancement by metallic subwave lattices on silicon in the near-infrared range. *Jetp Letters* **2019**, *110*, 411–416.

[169] Yakimov, A. I.; Bloshkin, A. A.; Dvurechenskii, A. V. Tailoring the optical field enhancement in Si-based structures covered by nanohole arrays in gold films for near-infrared photodetection. *Photon. Nanostruct. -Fundam. Appl.* **2020**, *40*, 100790.

[170] Azar, N. S.; Shrestha, V. R.; Crozier, K. B. Bull's eye grating integrated with optical nanoantennas for plasmonic enhancement of graphene long-wave infrared photodetectors. *Appl. Phys. Lett.* **2019**, *114*, 091108.

[171] Huang, Y.; Liu, Y.; Fang, C. Z.; Shao, Y.; Han, G. Q.; Zhang, J. C.; Hao, Y. Active tuning of the hybridization effects of mid-infrared surface plasmon resonance in a black phosphorus sheet array and a metal grating slit. *Opt. Mater. Express* **2020**, *10*, 14–28.

[172] Lee, I. H.; Martin-Moreno, L.; Mohr, D. A.; Khaliji, K.; Low, T.; Oh, S. H. Anisotropic acoustic plasmons in black phosphorus. *ACS Photonics* **2018**, *5*, 2208–2216.

[173] Huang, L.; Jia, Z. P.; Tang, B. Tunable anisotropic plasmon-induced transparency in black phosphorus-based metamaterials. *J. Opt.* **2022**, *24*, 014001.

[174] Huang, Y.; Liu, X. Y.; Liu, Y.; Shao, Y.; Zhang, S. Q.; Fang, C. Z.; Han, G. Q.; Zhang, J. C.; Hao, Y. Nanostructured multiple-layer black phosphorus photodetector based on localized surface plasmon resonance. *Opt. Mater. Express* **2019**, *9*, 739–750.

[175] Nguyen-Huu, N.; Pištora, J.; Cada, M.; Nguyen-Thoi, T.; Ma, Y. Q.; Yasumoto, K.; Rahman, B. M. A.; Wu, Q.; Ma, Y.; Ngo, Q. H. et al. Ultra-wide spectral bandwidth and enhanced absorption in a metallic compound grating covered by graphene monolayer. *IEEE J. Sel. Top. Quantum Electron.* **2021**, *27*, 8500108.

[176] Min, B. K.; Nguyen, V. T.; Kim, S. J.; Yi, Y.; Choi, C. G. Surface plasmon resonance-enhanced near-infrared absorption in single-layer MoS$_2$ with vertically aligned nanoflakes. *ACS Appl. Mater. Interfaces* **2020**, *12*, 14476–14483.

[177] Podder, S.; Pal, A. R. Hot carrier devices using visible and NIR responsive titanium nitride nanostructures with stoichiometry variation. *Opt. Mater.* **2019**, *97*, 109379.

[178] Hassan, S.; Bera, S.; Gupta, D.; Ray, S. K.; Sapra, S. MoSe$_2$-Cu$_2$S vertical p-n nanoheterostructures for high-performance photodetectors. *ACS Appl. Mater. Interfaces* **2019**, *11*, 4074–4083.

[179] Sarkar, S. S.; Bera, S.; Hassan, S.; Sapra, S.; Khatri, R. K.; Ray, S. K. MoSe$_2$-Cu$_{2-x}$S/GaAs heterostructure-based self-biased two color-band photodetectors with high detectivity. *J. Phys. Chem. C* **2021**, *125*, 10768–10776.

[180] Wu, J. Z. Exploration of uncooled quantum infrared detectors based on quantum dots/graphene heterostructures. In *Proceedings of SPIE 11407, Infrared Technology and Applications XLVI*, 2020, pp 1140706.

[181] Xu, J.; Cheng, X. L.; Liu, T.; Yu, Y. Q.; Song, L. L.; You, Y.; Wang, T.; Zhang, J. J. Oxygen-incorporated and layer-by-layer stacked WS$_2$ nanosheets for broadband, self-driven and fast-response photodetection. *Nanoscale* **2019**, *11*, 6810–6816.

[182] Guo, J. X.; Liu, Y.; Lin, Y.; Tian, Y.; Zhang, J. X.; Gong, T. X.; Cheng, T. D.; Huang, W.; Zhang, X. S. Simulation of tuning graphene plasmonic behaviors by ferroelectric domains for self-driven infrared photodetector applications. *Nanoscale* **2019**, *11*, 20868–20875.

[183] Guo, Q. S.; Yu, R. W.; Li, C.; Yuan, S. F.; Deng, B. C.; de Abajo, F. J. G.; Xia, F. N. Efficient electrical detection of mid-infrared graphene plasmons at room temperature. *Nat. Mater.* **2018**, *17*, 986–992.

[184] Sun, T.; Ma, W. L.; Liu, D. H.; Bao, X. Z.; Shabbir, B.; Yuan, J.; Li, S. J.; Wei, D. C.; Bai, Q. L. Graphene plasmonic nanoresonators/graphene heterostructures for efficient room-temperature infrared photodetection. *J. Semicond.* **2020**, *41*, 072907.

[185] Sun, Y. X.; Niu, G.; Ren, W.; Meng, X. J.; Zhao, J. Y.; Luo, W. B.; Ye, Z. G.; Xie, Y. H. Hybrid system combining two-dimensional materials and ferroelectrics and its application in photodetection. *ACS Nano* **2021**, *15*, 10982–11013.

[186] Huang, H.; Wang, X. D.; Wang, P.; Wu, G. J.; Chen, Y.; Meng, C. M.; Liao, L.; Wang, J. L.; Hu, W. D.; Shen, H. et al. Ferroelectric polymer tuned two dimensional layered MoTe$_2$ photodetector. *RSC Adv.* **2016**, *6*, 87416–87421.

[187] Wu, G. J.; Wang, X. D.; Wang, P.; Huang, H.; Chen, Y.; Sun, S.; Shen, H.; Lin, T.; Wang, J. L.; Zhang, S. T. et al. Visible to short wavelength infrared In$_2$Se$_3$-nanoflake photodetector gated by a ferroelectric polymer. *Nanotechnology* **2016**, *27*, 364002.

[188] Zheng, D. Y.; Dong, X. Y.; Lu, J.; Niu, Y. R.; Wang, H. High-sensitivity infrared photoelectric detection based on WS$_2$/Si structure tuned by ferroelectrics. *Small* **2022**, *18*, 2105188.

[189] Wang, X. D.; Wang, P.; Wang, J. L.; Hu, W. D.; Zhou, X. H.; Guo, N.; Huang, H.; Sun, S.; Shen, H.; Lin, T. et al. Ultrasensitive and broadband MoS$_2$ photodetector driven by ferroelectrics. *Adv. Mater.* **2015**, *27*, 6575–6581.

[190] Liu, L.; Wu, L. M.; Wang, A. W.; Liu, H. T.; Ma, R. S.; Wu, K.; Chen, J. C.; Zhou, Z.; Tian, Y.; Yang, H. T. et al. Ferroelectric-gated InSe photodetectors with high on/off ratios and photoresponsivity. *Nano Lett.* **2020**, *20*, 6666–6673.

[191] Jin, H. J.; Park, C.; Lee, K. J.; Shin, G. H.; Choi, S. Y. Ultrasensitive WSe$_2$/α-In$_2$Se$_3$ NIR photodetector based on ferroelectric gating effect. *Adv. Mater. Technol.* **2021**, *6*, 2100494.

[192] Zhu, C. C.; Wang, Y. R.; Wang, F.; Yang, J.; Zhan, X. Y.; Fang, L.; Wang, Z. X.; He, J. Nonvolatile reconfigurable broadband photodiodes based on BP/α-In$_2$Se$_3$ ferroelectric p-n junctions. *Appl. Phys. Lett.* **2022**, *120*, 083101.

[193] Guan, H. Y.; Hong, J. Y.; Wang, X. L.; Ming, J. Y.; Zhang, Z. L.; Liang, A. J.; Han, X. Y.; Dong, J. L.; Qiu, W. T.; Chen, Z. et al. Broadband, high-sensitivity graphene photodetector based on ferroelectric polarization of lithium niobate. *Adv. Opt. Mater.* **2021**, *9*, 2100245.

[194] Sun, Y. L.; Xie, D.; Zhang, X. W.; Xu, J. L.; Li, X. M.; Li, X.; Dai, R. X.; Li, X.; Li, P. L.; Gao, X. S. et al. Temperature-dependent transport and hysteretic behaviors induced by interfacial states in MoS$_2$ field-effect transistors with lead-zirconate-titanate ferroelectric gating. *Nanotechnology* **2017**, *28*, 045204.

[195] Tai, X. C.; Chen, Y.; Wu, S. Q.; Jiao, H. X.; Cui, Z. Z.; Zhao, D. Y.; Huang, X. N.; Zhao, Q. R.; Wang, X. D.; Lin, T. et al. High-

performance ReS$_2$ photodetectors enhanced by a ferroelectric field and strain field. *RSC Adv.* **2022**, *12*, 4939–4945.

[196] Baeumer, C.; Saldana-Greco, D.; Martirez, J. M. P.; Rappe, A. M.; Shim, M.; Martin, L. W. Ferroelectrically driven spatial carrier density modulation in graphene. *Nat. Commun.* **2015**, *6*, 6136.

[197] Wu, G. J.; Wang, X. D.; Chen, Y.; Wu, S. Q.; Wu, B. M.; Jiang, Y. Y.; Shen, H.; Lin, T.; Liu, Q.; Wang, X. R. et al. MoTe$_2$ p-n homojunctions defined by ferroelectric polarization. *Adv. Mater.* **2020**, *32*, 1907937.

[198] Chen, Y.; Wang, X. D.; Huang, L.; Wang, X. T.; Jiang, W.; Wang, Z.; Wang, P.; Wu, B. M.; Lin, T.; Shen, H. et al. Ferroelectric-tuned van der Waals heterojunction with band alignment evolution. *Nat. Commun.* **2021**, *12*, 4030.

[199] Wang, X. D.; Shen, H.; Chen, Y.; Wu, G. J.; Wang, P.; Xia, H.; Lin, T.; Zhou, P.; Hu, W. D.; Meng, X. J. et al. Multimechanism synergistic photodetectors with ultrabroad spectrum response from 375 nm to 10 μm. *Adv. Sci.* **2019**, *6*, 1901050.

[200] Wang, P.; Wang, Y.; Ye, L.; Wu, M. Z.; Xie, R. Z.; Wang, X. D.; Chen, X. S.; Fan, Z. Y.; Wang, J. L.; Hu, W. D. Ferroelectric localized field-enhanced ZnO nanosheet ultraviolet photodetector with high sensitivity and low dark current. *Small* **2018**, *14*, 1800492.

[201] Zhang, S. K.; Jiao, H. X.; Wang, X. D.; Chen, Y.; Wang, H. L.; Zhu, L. Q.; Jiang, W.; Liu, J. J.; Sun, L. X.; Lin, T. et al. Highly sensitive InSb nanosheets infrared photodetector passivated by ferroelectric polymer. *Adv. Funct. Mater.* **2020**, *30*, 2006156.

[202] Tao, L.; Chen, Z. F.; Li, Z. Y.; Wang, J. Q.; Xu, X.; Xu, J. B. Enhancing light–matter interaction in 2D materials by optical micro/nano architectures for high-performance optoelectronic devices. *InfoMat* **2021**, *3*, 36–60.

[203] Zheng, Z. Q.; Chen, P. F.; Lu, J. T.; Yao, J. D.; Zhao, Y.; Zhang, M. L.; Hao, M. M.; Li, J. B. Self-assembly In$_2$Se$_3$/SnSe$_2$ heterostructure array with suppressed dark current and enhanced photosensitivity for weak signal. *Sci. China Mater.* **2020**, *63*, 1560–1569.

[204] Qiao, S.; Cong, R. D.; Liu, J. H.; Liang, B. L.; Fu, G. S.; Yu, W.; Ren, K. L.; Wang, S. F.; Pan, C. F. A vertically layered MoS$_2$/Si heterojunction for an ultrahigh and ultrafast photoresponse photodetector. *J. Mater. Chem. C* **2018**, *6*, 3233–3239.

[205] Yao, J. D.; Zheng, Z. Q.; Yang, G. W. Ultrasensitive 2D/3D heterojunction multicolor photodetectors: A synergy of laterally and vertically aligned 2D layered materials. *ACS Appl. Mater. Interfaces* **2018**, *10*, 38166–38172.

[206] Wu, P. S.; Ye, L.; Tong, L.; Wang, P.; Wang, Y.; Wang, H. L.; Ge, H. N.; Wang, Z.; Gu, Y.; Zhang, K. et al. Van der Waals two-color infrared photodetector. *Light: Sci. Appl.* **2022**, *11*, 6.

[207] Lee, H. S.; Lim, J. Y.; Yu, S.; Jeong, Y.; Park, S.; Oh, K.; Hong, S.; Yang, S.; Lee, C. H.; Im, S. Seamless MoTe$_2$ homojunction PIN diode toward 1, 300 nm short-wave infrared detection. *Adv. Opt. Mater.* **2019**, *7*, 1900768.

[208] Jackson, E. M.; Nolde, J. A.; Kim, M.; Kim, C. S.; Cleveland, E. R.; Affouda, C. A.; Canedy, C. L.; Vurgaftman, I.; Meyer, J. R.; Aifer, E. H. et al. Two-dimensional plasmonic grating for increased quantum efficiency in midwave infrared *nBn* detectors with thin absorbers. *Opt. Express* **2018**, *26*, 13850–13864.

[209] Chen, Y. F.; Wang, Y.; Wang, Z.; Gu, Y.; Ye, Y.; Chai, X. L.; Ye, J. F.; Chen, Y.; Xie, R. Z.; Zhou, Y. et al. Unipolar barrier photodetectors based on van der Waals heterostructures. *Nat. Electron.* **2021**, *4*, 357–363.

[210] Zeng, L. H.; Wu, D.; Jie, J. S.; Ren, X. Y.; Hu, X.; Lau, S. P.; Chai, Y.; Tsang, Y. H. Van der Waals epitaxial growth of mosaic-like 2D platinum ditelluride layers for room-temperature mid-infrared photodetection up to 10.6 μm. *Adv. Mater.* **2020**, *32*, 2004412.

[211] Tong, L.; Huang, X. Y.; Wang, P.; Ye, L.; Peng, M.; An, L. C.; Sun, Q. D.; Zhang, Y.; Yang, G. M.; Li, Z. et al. Stable mid-infrared polarization imaging based on quasi-2D tellurium at room temperature. *Nat. Commun.* **2020**, *11*, 2308.

[212] Ahn, J.; Ko, K.; Kyhm, J. H.; Ra, H. S.; Bae, H.; Hong, S.; Kim, D. Y.; Jang, J.; Kim, T. W.; Choi, S. et al. Near-infrared self-powered linearly polarized photodetection and digital incoherent holography

using WSe$_2$/ReSe$_2$ van der Waals heterostructure. *ACS Nano* **2021**, *15*, 17917–17925.

[213] Liu, N.; Tian, H.; Schwartz, G.; Tok, J. B. H.; Ren, T. L.; Bao, Z. N. Large-area, transparent, and flexible infrared photodetector fabricated using P-N junctions formed by N-doping chemical vapor deposition grown graphene. *Nano Lett.* **2014**, *14*, 3702–3708.

[214] Zhang, T.; Ling, C. C.; Wang, X. M.; Feng, B. X.; Cao, M.; Xue, X.; Xue, Q. Z.; Zhang, J. Q.; Zhu, L.; Wang, C. K. et al. Six-arm stellat dendritic-PbS flexible infrared photodetector for intelligent healthcare monitoring. *Adv. Mater. Technol.* **2022**, *7*, 2200250.

[215] Fang, J. Z.; Zhou, Z. Q.; Xiao, M. Q.; Lou, Z.; Wei, Z. M.; Shen, G. Z. Recent advances in low-dimensional semiconductor nanomaterials and their applications in high-performance photodetectors. *InfoMat* **2020**, *2*, 291–317.

[216] Yao, J. D.; Yang, G. W. Flexible and high-performance all-2D photodetector for wearable devices. *Small* **2018**, *14*, 1704524.

[217] Li, J. Y.; Han, J. F.; Li, H. X.; Fan, X. Y.; Huang, K. Large-area, flexible broadband photodetector based on WS$_2$ nanosheets films. *Mater. Sci. Semicond. Proc.* **2020**, *107*, 104804.

[218] Choi, J. M.; Jang, H. Y.; Kim, A. R.; Kwon, J. D.; Cho, B.; Park, M. H.; Kim, Y. Ultra-flexible and rollable 2D-MoS$_2$/Si heterojunction-based near-infrared photodetector via direct synthesis. *Nanoscale* **2021**, *13*, 672–680.

[219] Thai, K. Y.; Park, I.; Kim, B. J.; Hoang, A. T.; Na, Y.; Park, C. U.; Chae, Y.; Ahn, J. H. MoS$_2$/graphene photodetector array with strain-modulated photoresponse up to the near-infrared regime. *ACS Nano* **2021**, *15*, 12836–12846.

[220] Cordeiro, N. J. A.; Gaspar, C.; de Oliveira, M. J.; Nunes, D.; Barquinha, P.; Pereira, L.; Fortunato, E.; Martins, R.; Laureto, E.; Lourenço, S. A. Fast and low-cost synthesis of MoS$_2$ nanostructures on paper substrates for near-infrared photodetectors. *Appl. Sci.* **2021**, *11*, 1234.

[221] Mazaheri, A.; Lee, M.; van der Zant, H. S. J.; Frisenda, R.; Castellanos-Gomez, A. MoS$_2$-on-paper optoelectronics: Drawing photodetectors with van der Waals semiconductors beyond graphite. *Nanoscale* **2020**, *12*, 19068–19074.

[222] Bie, Y. Q.; Grosso, G.; Heuck, M.; Furchi, M. M.; Cao, Y.; Zheng, J. B.; Bunandar, D.; Navarro-Moratalla, E.; Zhou, L.; Efetov, D. K. et al. A MoTe$_2$-based light-emitting diode and photodetector for silicon photonic integrated circuits. *Nat. Nanotechnol.* **2017**, *12*, 1124–1129.

[223] Liu, C. Y.; Guo, J. S.; Yu, L. W.; Xiang, Y. L.; Xiang, H. T.; Li, J.; Dai, D. X. High-speed and high-responsivity silicon/black-phosphorus hybrid plasmonic waveguide avalanche photodetector. *ACS Photonics* **2022**, *9*, 1764–1774.

[224] Lin, H. T.; Song, Y.; Huang, Y. Z.; Kita, D.; Deckoff-Jones, S.; Wang, K. Q.; Li, L.; Li, J. Y.; Zheng, H. Y.; Luo, Z. Q. et al. Chalcogenide glass-on-graphene photonics. *Nat. Photonics* **2017**, *11*, 798–805.

[225] Yuan, S. F.; Naveh, D.; Watanabe, K.; Taniguchi, T.; Xia, F. N. A wavelength-scale black phosphorus spectrometer. *Nat. Photonics* **2021**, *15*, 601–607.

[226] Zhang, Z. H.; Yang, X. N.; Liu, K. H.; Wang, R. M. Epitaxy of 2D materials toward single crystals. *Adv. Sci.* **2022**, *9*, 2105201.

[227] Li, T. T.; Guo, W.; Ma, L.; Li, W. S.; Yu, Z. H.; Han, Z.; Gao, S.; Liu, L.; Fan, D. X.; Wang, Z. X. et al. Epitaxial growth of wafer-scale molybdenum disulfide semiconductor single crystals on sapphire. *Nat. Nanotechnol.* **2021**, *16*, 1201–1207.

[228] Lei, Y.; Yang, X. Z.; Feng, W. L. Synthesis of vertically-aligned large-area MoS$_2$ nanofilm and its application in MoS$_2$/Si heterostructure photodetector. *Nanotechnology* **2022**, *33*, 105709.

[229] Yang, H. W.; Xiao, Y. H.; Zhang, K. M.; Chen, Z. F.; Pan, J. T.; Zhuo, L. Q.; Zhong, Y. C.; Zheng, H. D.; Zhu, W. G.; Yu, J. H. et al. Self-powered and high-performance all-fiber integrated photodetector based on graphene/palladium diselenide heterostructures. *Opt. Express* **2021**, *29*, 15631–15640.

[230] Guo, J. X.; Lin, L.; Li, S. D.; Chen, J. B.; Wang, S. C.; Wu, W. J.; Cai, J.; Zhou, T. C.; Liu, Y.; Huang, W. Ferroelectric superdomain controlled graphene plasmon for tunable mid-infrared photodetector with dual-band spectral selectivity. *Carbon* **2022**,

*189*, 596–603.

[231] Kim, Y. R.; Phan, T. L.; Cho, K. W.; Kang, W. T.; Kim, K.; Lee, Y. H.; Yu, W. J. Infrared proximity sensors based on photo-induced tunneling in van der Waals integration. *Adv. Funct. Mater.* **2021**, *31*, 2100966.

[232] Rogalski, A.; Kopytko, M.; Martyniuk, P.; Hu, W. Comparison of performance limits of HOT HgCdTe photodiodes with 2D material infrared photodetectors. *Opto-Electron. Rev.* **2020**, *28*, 82–92.

[233] You, C. Y.; Deng, W. J.; Liu, M.; Zhou, P.; An, B. X.; Wang, B.; Yu, S. L.; Zhang, Y. Z. Design and performance study of hybrid graphene/HgCdTe mid-infrared photodetector. *IEEE Sens. J.* **2021**, *21*, 26708–26715.

[234] Hassan, A.; Guo, Y. G.; Wang, Q. Performance of the pentagonal PdSe$_2$ sheet as a channel material in contact with metal surfaces and graphene. *ACS Appl. Electron. Mater.* **2020**, *2*, 2535–2542.

[235] Cartamil-Bueno, S. J.; Cavalieri, M.; Wang, R. Z.; Houri, S.; Hofmann, S.; van der Zant, H. S. J. Mechanical characterization and cleaning of CVD single-layer h-BN resonators. *npj 2D Mater. Appl.* **2017**, *1*, 16.